

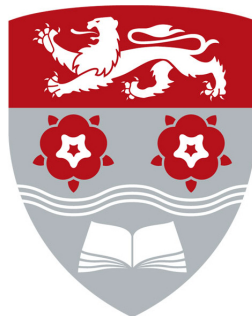
QUANTUM MONTE CARLO STUDY OF LOW
DIMENSIONAL MATERIALS

Elaheh Mostaani

Department of Physics, Lancaster University

A dissertation submitted for the degree of Doctor of
Philosophy at the University of Lancaster

February 2016



TO MY PARENTS,

for their endless love, support and encouragement.

Foreword

This thesis describes work carried out between October 2012 and February 2016 in the Condensed Matter group at the Department of Physics, Lancaster University under the supervision of Dr. N.D. Drummond. The following sections of this thesis are included in work that has been published, is submitted or to be submitted:

Chapter 1 Section 1.6.6 of this chapter is included in P. López Ríos, E. Mostaani, N. D. Drummond and R. J. Needs, *Finite-size effects in backflow corrections to quantum Monte Carlo energies*, to be submitted.

Chapter 2 E. Mostaani, N. D. Drummond and V. I. Fal'ko, *Quantum Monte Carlo calculation of the binding energy of bilayer graphene*, Phys. Rev. Lett. **115**, 115501 (2015).

Chapter 3 E. Mostaani, N. D. Drummond and V. I. Fal'ko, *Quantum Monte Carlo calculation of the binding energy of graphene on boron nitride bilayer*, to be submitted.

Chapter 4 E. Mostaani, M. Szyniszewski, C. Price, R. Maezono, N. D. Drummond and V. I. Fal'ko, *Biexcitons in Two-Dimensional Semiconductors*, to be submitted.

Chapter 5 E. Mostaani, B. Monserrat, N. D. Drummond and C. J. Lambert, *Quasiparticle and excitonic gaps of one-dimensional carbon chains*, Submitted to PCCP, preprint arXiv:1601.04324.

This thesis is my own work and contains nothing which is the outcome of work done in collaboration with others, except as specified in the text and Acknowledgements. This thesis has not been submitted in substantially the same form for the award of a higher degree elsewhere. This thesis does not exceed the word limit of 80,000 words.

Elaheh Mostaani

Lancaster, February 2016

Abstract

This thesis addresses several challenging problems in low-dimensional systems, which have rarely or never been studied using quantum Monte Carlo methods. It begins with an investigation into weak van der Waals-like interactions in bilayer graphene and extends to graphene placed on top of boron nitride at four different stacking configurations. The in-plane optical phonon frequencies for the latter heterostructure as well as the out-of-plane phonon frequencies for both structures are calculated. We find that the binding energies (BEs) of these structures are almost within the same range and are less than 20 meV/atom. Although the phonon vibrations are comparable within both the diffusion quantum Monte Carlo (DMC) method and density functional theory (DFT), DFT gives quantitatively wrong BEs for vdW structures. Next, the BEs of 2D biexcitons are studied at different mass ratios and a variety of screening lengths. Our exact DMC results show that the BEs of biexcitons in different kinds of transition-metal dichalcogenides are in the range 15 – 30 meV bound at room temperature.

Besides 2D systems, the electronic properties of 1D hydrogen-terminated oligoynes and polyynes are studied by calculating their DMC quasiparticle and excitonic gaps. By minimising the DMC energy of free-standing polyynes with respect to the lattice constant and the bond-length alternation, DMC predicts geometry in agreement with that obtained by accurate quantum chemistry methods. The DMC longitudinal optical phonon is within the range of experimental values. Our results confirm that DMC is capable of accurately describing Peierls-distorted materials.

Acknowledgments

I am privileged to have worked under the supervision of Neil Drummond during my time at Lancaster and would like to express my deep and sincere gratitude to him for all of the guidance and support that he has given me. I am also indebted to Volodya Fal'ko for helpful discussions and his support in this work. I would also like to thank Colin Lambert for helpful discussions in part of my thesis and also giving me a chance to be involved in his group seminars and their events in a pleasant environment.

This thesis has been financially supported by the Physics Department of Lancaster University. Computational facilities have been provided by the Lancaster High End Computing Cluster (HEC) facility and N8 HPC provided and funded by the N8 consortium and Engineering and Physical Sciences Research Council (EPSRC). I would like to thank Mike Pacey, Steve Marple, Robin Lewsey, Sandra Irving and Susan Harrison for their helpful advice.

I am grateful to Marjan Famili, Marcin Szyniszewski, Jake Arkinstall, Simon Malzard and other PhD students of condensed matter group in Physics Department of Lancaster University and all my friends for making my time in Lancaster so enjoyable; Needless to mention that I thank my family specially my parents for supporting me spiritually throughout my life.

Contents

1	Introduction	1
1.1	Electronic structure calculation	1
1.2	Hartree–Fock method	3
1.3	Quantum chemistry methods	6
1.4	Density functional theory	7
1.5	Basis sets	10
1.6	Quantum Monte Carlo methods	13
1.6.1	Monte Carlo integration	14
1.6.2	Slater–Jastrow wave function	15
1.6.3	Variational quantum Monte Carlo method	18
1.6.4	Theory of diffusion quantum Monte Carlo	21
1.6.5	Sources of errors in VMC and DMC calculations	24
1.6.6	Backflow transformations	27
2	DMC binding energy of bilayer graphene	33
2.1	Introduction	33
2.2	Computational details	35
2.2.1	Finite-population errors in our DMC data	36
2.2.2	Finite-size errors in our DMC data	37
2.3	Results and discussion	39
2.3.1	Atomisation energy of monolayer graphene	39
2.3.2	Binding energy of bilayer graphene	42
2.3.3	Choice of fitting function for the binding-energy curve	46
2.4	Conclusion	49
3	DMC binding energies of G/hBN moiré heterostructures	50
3.1	Introduction	50
3.2	Computational details	51
3.3	Results and discussion	54
3.3.1	Time-step errors in our DMC calculations	54
3.3.2	DMC binding energy of G/hBN	56
3.3.3	Breathing mode optical phonon frequency of G/hBN	58
3.3.4	DMC in-plane shear mode of G/hBN	60
3.4	Conclusion	61
4	Biexcitons in monolayer transition-metal dichalcogenides	62
4.1	Introduction	62
4.2	Electrostatic interactions	63
4.3	Units and scaling for different interactions	65

4.4	Excitons and biexcitons with distinguishable particles	68
4.5	Biexcitons with indistinguishable particles	71
4.6	Time-step and population-control biases	74
4.7	Limit of heavy holes	74
4.7.1	Binding energy of biexcitons	77
4.8	Conclusion	84
5	Quasiparticle and excitonic gaps of one-dimensional carbon chains	85
5.1	Introduction	85
5.2	Computational methodology	87
5.2.1	DFT calculations	87
5.2.2	QMC calculations	88
5.2.3	DMC quasiparticle and excitonic gaps	90
5.2.4	Finite-size effects	91
5.2.5	Test of our method: benzene molecule	93
5.3	Results and discussion	94
5.3.1	Atomic structures and atomisation energies of linear hydrogen-terminated oligynes	94
5.3.2	Atomic structure and atomisation energy of polyynes	95
5.3.3	Quasiparticle and excitonic gaps of hydrogen-terminated oligynes	102
5.3.4	Quasiparticle and excitonic gaps of polyynes	105
5.4	Conclusions	110
6	Overall conclusions	111
Appendix A Interlayer vdW forces of bilayer graphene		113
A.1	Introduction	113
A.2	vdW forces between two slabs	121
A.3	vdW forces in bilayer graphene	125

List of Figures

1.1	Local energy of a 2D biexciton against the separation of electrons. . .	17
1.2	Reblocking eight elements into three blocking transformations. . .	25
2.1	DMC GS energy of a 3×3 cell of monolayer graphene and a C atom as a function of the reciprocal of the configuration population . . .	37
2.2	Atomisation energy of monolayer graphene against $N_P^{-5/4}$	40
2.3	DMC BE of BLG against $N_P^{-5/4}$	42
2.4	BE curve of AB-stacked BLG as a function of interlayer distance. . .	44
2.5	DMC BE of AB-stacked BLG against interlayer separation using different fitting curves.	47
2.6	Histogram of $E''_{\text{bind}}(d_0)$ obtained in bootstrap Monte Carlo sampling. . .	48
3.1	Four different stacking configurations of bilayer G/hBN.	52
3.2	DMC GS energy of MLG, hBN, and stacking pattern II of G/hBN against time step for a supercell consisting of 3×3 primitive cells. . .	55
3.3	DMC BE curve of G/hBN against the interlayer separation for con- figuration stacks I–IV.	56
3.4	DFT-LDA phonon dispersions of G/hBN for stacking configurations I and II.	59
3.5	DMC BE of bilayer G/hBN against the sliding distance.	60
4.1	DMC BE of a biexciton with the logarithmic interaction against r^* . . .	68
4.2	The PDF of a biexciton with distinguishable particles against the interparticle separation.	71
4.3	DMC GS energy of the biexciton with distinguishable particles against the DMC time step.	74
4.4	DMC GS energy of a heavy-hole biexciton with the logarithmic interaction against the hole separation.	76
4.5	VMC and DMC GS energies of heavy-hole biexcitons with the Keldysh interaction against the hole separations at different r^*	78
4.6	DMC BE of a biexciton with the logarithmic interaction against mass ratio	79
4.7	DMC BE of biexcitons with distinguishable particles and the Keldysh interaction against mass ratio and r^*	80
4.8	Comparison of DMC BE of biexcitons with distinguishable particles and indistinguishable holes against mass ratio.	81
4.9	Comparing the DMC and PIMC BE of biexcitons with distinguish- able particles in the Keldysh interaction.	82
4.10	DMC BE of biexcitons with distinguishable particles against $\frac{m_e/m_h}{1+m_e/m_h}$ and $\tilde{r}^*/(1 + \tilde{r}^*)$	83

5.1	Finite-size error in the total energy of a 1D exciton against the periodic cell length.	93
5.2	Optimised BLA of a hydrogen-terminated oligoyne in the ground and cationic states against $1/n$	95
5.3	DMC atomisation energies of hydrogen-terminated oligoynes as a function of $1/n$	96
5.4	GS DMC energy of polyyne as a function of BLA.	97
5.5	Phonon dispersion curve of polyyne calculated using DFT-LDA, DFT-PBE, and DFT-HSE06.	99
5.6	GS DMC energy of polyyne against $1/n^2$	100
5.7	DMC excitonic and quasiparticle gaps of oligoynes obtained using MD and single-determinant Slater–Jastrow trial wave functions against $1/n$	103
5.8	Quasiparticle gaps of hydrogen-terminated oligoynes against $1/n$	104
5.9	DMC singlet and triplet excitonic gaps of oligoynes against $1/n$	105
5.10	DMC singlet–triplet splitting of oligoynes obtained with DFT-PBE and DFT-HSE06 geometries.	105
5.11	DMC excitonic gaps of polyyne against the reciprocal of the number n	107
5.12	DFT-HSE06 band structure of polyyne.	108
A.1	Two slabs are placed in three different media.	122
A.2	vdW energy of bilayer graphene obtained by different methods.	128

List of Tables

1.1	VMC and DMC energies of a 14-electron 2D HEG with a density parameter $r_s = 4$	31
1.2	VMC-BF and DMC-BF corrections of a 14-electron 2D HEG with a density parameter $r_s = 4$	32
2.1	DFT and DMC atomisation energy of monolayer graphene.	40
2.2	DFT and DFT-D BEs of AB-stacked BLG at equilibrium separation.	41
2.3	BE of BLG obtained in recent theoretical studies.	44
2.4	The equilibrium separation, BE, and out-of-plane phonon frequency of AB-stacked BLG obtained by DFT, DFT-D, DMC, and experiment.	45
2.5	Comparing different parameters obtained by fitting different curves to the DMC BE of BLG.	48
3.1	Comparison of BE of G/hBN using DFT and DMC methods.	57
3.2	Relative BE of G/hBN for different stacking patterns of G/hBN.	57
3.3	Comparison of equilibrium interlayer separation of G/hBN using DFT and DMC methods.	58
3.4	Parameters obtained for four stacks of G/hBN using the DMC BE curve.	60
4.1	Order of η in the E_{VMC} , variance and E_{DMC} of biexcitons with identical electrons in the logarithmic interaction limit.	73
4.2	Order of η in the E_{VMC} , variance and DMC energy E_{DMC} of biexcitons with identical electrons interacting via the Keldysh interaction.	73
4.3	Comparing VMC and DMC parameters obtained by BE of heavy-hole biexciton with distinguishable electrons at different r^* in the Keldysh interaction.	77
4.4	BEs of biexcitons with distinguishable particles for different monolayer transition-metal dichalcogenides.	83
5.1	Number of MD terms and orbital occupancies in each determinant in our calculations.	89
5.2	BLA and lattice constant of polyynes.	101
5.3	Atomisation energy of polyynes obtained by different methods.	102
5.4	Singlet excitonic gaps and quasiparticle gaps of polyynes obtained by different methods.	109

CHAPTER 1

Introduction

1.1 Electronic structure calculation

The story of electronic structure begins in the 1880s when the electron was discovered as a fundamental constituent of matter [1]. Electrons orbiting nuclei cannot be treated as classical particles because they are accelerating; a classical analysis suggests that they would continuously radiate energy, and therefore the radius of the orbit would shrink with time. On the contrary, the quantum mechanical model of the atom is based on probability rather than certainty and uses complex shapes of orbitals. According to this model, when the positions of all nuclei are held fixed in a system, the electrons reach a steady state and form an “electron cloud” with a stable charge-density distribution determined quantum mechanically. This basic idea, together with the quantum description of electron excitations, determines a variety of electrical, optical, vibrational, mechanical, and magnetic properties of materials.

To study the electronic structure of materials from first principles, it is essential that the many-electron Schrödinger equation be solved accurately, which is one of the great challenges of condensed-matter physics due to the large number of particles involved. First-principles (*ab initio*) methods, as a vital computational

tool in modern condensed-matter physics and molecular quantum chemistry, have opened a new era in which one can design and investigate new materials with desired properties. However, first-principles simulations depending on the method can be expensive for few hundred atoms, even with the fastest supercomputers.

In general, there are four main first-principles approaches to determine the ground state of many-electron systems in both condensed matter and molecules: A starting point for many-body calculations, as described in Sec. 1.2, is Hartree–Fock (HF) theory, which can be expanded to establish the *Ab initio* quantum chemistry or post–HF methods that are introduced in Sec. 1.3. We have not used HF and post-HF methods in our calculations; however we briefly discuss their fundamental theory to show how they can be used in many-body calculations. In Sec. 1.4, we represent density functional theory (DFT), by which we have provided initial information for our main calculations using quantum Monte Carlo (QMC) methods, which are introduced in Sec. 1.6.

Our DFT and QMC calculations are performed within the Born–Oppenheimer (B–O) approximation, by which we separate the calculation of electronic structure from that of the ionic motion. This is valid because the electron mass is considerably smaller than nuclear masses and electrons very quickly follow nuclear motion. Therefore, any change in the electronic state occurs quickly compared to the nuclear motion. All our results and equations are reported in Hartree atomic units (a.u.) ($|e| = \hbar = m_e = 4\pi\epsilon_0 = 1$) unless stated otherwise. In atomic units, the unit of length is the Bohr radius (0.529×10^{-10} m) and the unit of energy is the Hartree ($= 2$ Rydberg $= 27.2$ eV $= 4.36 \times 10^{-18}$ J).

We consider the nonrelativistic Hamiltonian of the form

$$\hat{H} = - \sum_{i=1}^N \frac{1}{2} \nabla_i^2 - \sum_{i=1}^N \sum_{I=1}^{N_n} \frac{Z_I}{r_{iI}} + \frac{1}{2} \sum_{i \neq j}^N \frac{1}{r_{ij}} + \frac{1}{2} \sum_{I \neq J}^{N_n} \frac{Z_I Z_J}{r_{IJ}}, \quad (1.1)$$

where N and N_n are the numbers of electrons and nuclei, respectively. Z is atomic

number and r is separation, where the indices i and j refer to electrons while I and J refer to nuclei. The first term in Eq. 1.1 is the operator for the kinetic energy; the second term represents the Coulomb attraction between electrons and nuclei, which can be replaced by a pseudopotential; the third term is the Coulomb interaction between electrons and the fourth term is the internucleus energy, which adds a constant value to the electron energy eigenvalue.

The fundamental idea of pseudopotentials is that the tightly bound core electrons are replaced by an effective potential acting on the valence electrons. Since the core electrons are considered inert, a pseudopotential can be generated in an atomic calculation and then applied to compute the properties of valence electrons in molecules and solids. Good pseudopotentials should be reasonably smooth and should be proportional to $1/r$ far from the nucleus. They should give the same orbitals and energies as all-electron calculations at large r . Using pseudopotentials reduces the computational cost and removes singularities in the electron-ion potential. We have used ultrasoft [2, 3] and Dirac-Fock pseudopotentials [4] in our DFT and QMC calculations, respectively. The Dirac-Fock pseudopotential is local outside of the core space and is norm conserving, while ultrasoft pseudopotentials are not norm conserving; inside the core radius, the norm of each pseudo-wavefunction differs from that of the all-electron wave function.

1.2 Hartree-Fock method

The HF approximation [5] is an important starting point for many-body methods such as QMC. In the HF method, the time-independent Schrödinger equation is solved for an independent N -electron system within the B-O approximation. The

trial wave function, Ψ_S , is a Slater determinant, defined as:

$$\begin{aligned}\Psi_S(\mathbf{X}_1, \dots, \mathbf{X}_N) &= \frac{1}{\sqrt{N!}} \begin{vmatrix} \chi_1(\mathbf{X}_1) & \dots & \chi_1(\mathbf{X}_N) \\ \vdots & \dots & \vdots \\ \chi_N(\mathbf{X}_1) & \dots & \chi_N(\mathbf{X}_N) \end{vmatrix} \\ &= \frac{1}{\sqrt{N!}} \sum_{\hat{P}} (-1)^p \hat{P}[\chi_1(\mathbf{X}_1), \dots, \chi_N(\mathbf{X}_N)],\end{aligned}\quad (1.2)$$

where \hat{P} is a permutation operator and $(-1)^p$ is the corresponding parity, which is 1 for an even number of swaps and -1 for an odd number of swaps. $\{\chi\}$ are single-electron spin-orbital wave functions depending on $\mathbf{X} = \{\mathbf{r}, \sigma\}$, where \mathbf{r} and σ are spatial and spin coordinates, respectively. The spin orbitals $\{\chi\}$ form an orthonormal set:

$$\langle \chi_i | \chi_j \rangle = \int \chi_i^\dagger(\mathbf{X}) \chi_j(\mathbf{X}) d\mathbf{X} = \delta_{ij}.\quad (1.3)$$

The variational principle for the normalised wave function Ψ_S gives an upper bound on the exact ground state energy, E_0 :

$$\begin{aligned}\langle \Psi_S | \hat{H} | \Psi_S \rangle &= \int \Psi_S^*(\mathbf{X}_1, \dots, \mathbf{X}_N) \hat{H} \Psi_S(\mathbf{X}_1, \dots, \mathbf{X}_N) d\mathbf{X}_1 \dots d\mathbf{X}_N \\ &\geq E_0.\end{aligned}\quad (1.4)$$

The expectation value of the Hamiltonian using Eqs. 1.1, 1.2 and 1.4 is:

$$\begin{aligned}\langle \Psi_S | \hat{H} | \Psi_S \rangle &= \frac{N}{N!} \sum_{\hat{P}', \hat{P}} (-1)^{p'+p} \int \hat{P}'[\chi_1^*(\mathbf{X}_1), \dots, \chi_N^*(\mathbf{X}_N)] \hat{h} \hat{P}[\chi_1(\mathbf{X}_1), \dots, \chi_N(\mathbf{X}_N)] d\mathbf{X} \\ &\quad + \frac{N(N-1)}{2N!} \sum_{\hat{P}', \hat{P}} (-1)^{p'+p} \int \hat{P}'[\chi_1^*(\mathbf{X}_1), \dots, \chi_N^*(\mathbf{X}_N)] \\ &\quad \times r_{12}^{-1} \hat{P}[\chi_1(\mathbf{X}_1), \dots, \chi_N(\mathbf{X}_N)] d\mathbf{X} \\ &= \sum_{i=1}^N \langle \chi_i | \hat{h} | \chi_i \rangle + \frac{1}{2} \sum_{i,j} [\langle \chi_i \chi_j | r_{12}^{-1} | \chi_i \chi_j \rangle - \langle \chi_i \chi_j | r_{12}^{-1} | \chi_j \chi_i \rangle],\end{aligned}\quad (1.5)$$

where $\hat{h} = -(1/2)\nabla_i^2 - \sum_I Z_I/r_{iI}$ corresponds to the first two terms of the Hamiltonian defined in Eq. 1.1. The HF interaction energy is the sum of the second and third terms of the last line of Eq. 1.5, known as the ‘‘Hartree’’ and ‘‘exchange’’ terms, respectively. The Hartree term is due to the charge density, while the exchange term stems from the antisymmetry of the wave function with respect to two-particle permutation (exchange). The exchange term keeps electrons of like spin apart and, as a result, each electron has around it a Fermi or exchange hole containing unit positive charge. To find the eigenvalues of the Hamiltonian using the variational principle, the Lagrangian $\mathcal{L} = \langle \Psi_S | \hat{H} | \Psi_S \rangle - \sum_{i,j} \mathcal{E}_{ij} (\langle \chi_i | \chi_j \rangle - \delta_{ij})$ should be minimised with respect to variations in $\{\chi\}$ subject to the constraints $\langle \chi_i | \chi_j \rangle = \delta_{ij}$. Here, $\mathcal{E}_{ij} = \mathcal{E}_{ji}^*$ are hermitian Lagrange multipliers that are unitarily diagonalisable. We therefore vary the spin orbitals an arbitrary infinitesimal amount $\{\chi\} \rightarrow \{\chi\} + \delta\{\chi\}$.

$$\begin{aligned}
\delta\mathcal{L} &= \delta \langle \Psi_S | \hat{H} | \Psi_S \rangle - \sum_{ij} \mathcal{E}_{ij} \delta \langle \chi_i | \chi_j \rangle \\
&= \sum_{i=1}^N \langle \delta\chi_i | \hat{h} | \chi_i \rangle + \sum_{i,j} [\langle \delta\chi_i \chi_j | r_{12}^{-1} | \chi_i \chi_j \rangle - \langle \delta\chi_i \chi_j | r_{12}^{-1} | \chi_j \chi_i \rangle] \\
&\quad - \sum_{ij} \mathcal{E}_{ij} \langle \delta\chi_i | \chi_j \rangle + \text{c.c.}
\end{aligned} \tag{1.6}$$

Requiring $\delta\mathcal{L} = 0$ leads to the HF equation:

$$\begin{aligned}
\sum_j \mathcal{E}_{ij} \chi_j(\mathbf{X}_1) \equiv \hat{f}\chi_i(\mathbf{X}_1) &= \hat{h}\chi_i(\mathbf{X}_1) + \sum_{j=1}^N \left(\int r_{12}^{-1} |\chi_j(\mathbf{X}_2)|^2 \chi_i(\mathbf{X}_1) d\mathbf{X}_2 \right. \\
&\quad \left. - \int r_{12}^{-1} \chi_j^*(\mathbf{X}_2) \chi_i(\mathbf{X}_2) \chi_j(\mathbf{X}_1) d\mathbf{X}_2 \right).
\end{aligned} \tag{1.7}$$

$\hat{f} = \hat{h} + \hat{v}_{\text{HF}}$ is the Fock operator, where v_{HF} is the sum of the direct and the exchange terms. The former is the average local potential energy at \mathbf{X}_1 due to an electron in χ_j and the latter is because of the antisymmetry of the wave function under exchange of electrons 1 and 2 [6].

Although the HF method often gives qualitatively correct results for the ground-state energies, it has some important drawbacks; for example, the HF approximation in metals gives a zero density of states at the Fermi level due to the logarithmically divergent derivative of energy bands with respect to k at the Fermi surface [7]. Also, HF theory overestimates the energy gaps of semiconductors between the occupied and unoccupied states, because HF theory cannot fully describe electronic screening or correlation.

1.3 Quantum chemistry methods

Quantum chemistry or post-HF methods include electronic correlations by using a linear combination of Slater determinants. There are different kind of quantum chemistry methods [6, 8] such as a full configuration-interaction (full CI), which constructs all possible Slater determinants of a N -electron system from a set of $2K$ basis functions $\{\chi_i\}$ to introduce the many-electron wave function $|\phi_0\rangle$,

$$\begin{aligned}
 |\phi_0\rangle = & c_0|\Psi_0\rangle + \sum_{ar} c_a^r|\Psi_a^r\rangle + \sum_{a<b;r<s} c_{ab}^{rs}|\Psi_{ab}^{rs}\rangle \\
 & + \sum_{a<b<c;r<s<t} c_{abc}^{rst}|\Psi_{abc}^{rst}\rangle + \dots, \tag{1.8}
 \end{aligned}$$

where the set of possible determinants include $|\Psi_0\rangle$ as the determinant formed from N lowest energy spin orbitals, $|\Psi_a^r\rangle$ as the singly excited determinants by having χ_a replaced by χ_r , $|\Psi_{ab}^{rs}\rangle$ as the doubly excited state, etc, up to the N -tuply excited determinants. The restrictions on the summation (e.g. $a < b$, $r < s$, etc.) ensure that a given excited determinant is included in the sum only once. The scale of quantum chemistry methods depends on the basis size. For example, the number of determinants in full CI methods rises exponentially with N and the current practical limit for highly accurate calculations is reached for small molecules. An alternative way to avoid this problem is to truncate the trial wave function in

Eq. 1.8 at the doubly excited state resulting in the CI singles and doubles excited (CISD) method, which scales as $\mathcal{O}(N^6)$. Similar to CISD, coupled-cluster singles and doubles (CCSD) [9] method is size consistent and Møller–Plesset second-order perturbation theory (MP2) [10] scales as $\mathcal{O}(N^5)$.

1.4 Density functional theory

In general, the charge density operator of N interacting electrons in volume Ω with normalised wave function $\psi(\mathbf{r}_1, \dots, \mathbf{r}_N)$ is

$$\hat{\rho} = \sum_{i=1}^N \delta(\mathbf{r} - \hat{\mathbf{r}}_i). \quad (1.9)$$

The expectation value of the charge density gives the electronic charge density

$$n(\mathbf{r}) = \langle \psi(\mathbf{r}_1, \dots, \mathbf{r}_N) | \hat{\rho} | \psi(\mathbf{r}_1, \dots, \mathbf{r}_N) \rangle, \quad (1.10)$$

which is the probability density of finding an electron at \mathbf{r} , normalised to N . For any system of interacting electrons in an external potential $V_{\text{ext}}(\mathbf{r})$, the Hamiltonian based on Hohenberg and Kohn (HK) [11] approach is defined as

$$\begin{aligned} \hat{H} &= -\frac{1}{2} \sum_i \nabla_i^2 + \frac{1}{2} \sum_{i \neq j} \frac{1}{r_{ij}} + \sum_i V_{\text{ext}}(\mathbf{r}_i) \\ &= \hat{T} + \hat{U}_{ee} + \hat{U}_{\text{ext}}. \end{aligned} \quad (1.11)$$

A unique lowest HK energy as a functional of electronic charge density is given by the variational principle:

$$\begin{aligned} E_{\text{HK}}[n(\mathbf{r})] &= \langle \psi | [\hat{T} + \hat{U}_{ee}] | \psi \rangle + \langle \psi | U_{\text{ext}} | \psi \rangle \\ &= F_{\text{HK}}[n(\mathbf{r})] + \int V_{\text{ext}}(\mathbf{r}) n(\mathbf{r}) \, d\mathbf{r} \geq E_0. \end{aligned} \quad (1.12)$$

Eq. 1.12 makes calculations cheaper by reducing the $3N$ -dimensional problem into a 3-dimensional problem. F_{HK} , the exact form of which is not known, includes all internal kinetic and potential energies of the interacting electron system. The most widely used approach to approximate F_{HK} is the Kohn–Sham (KS) Ansatz [12], which assumes that the exact ground-state charge density of an interacting system is equal to the ground-state charge density of an auxiliary noninteracting system of particles with the Slater wave function defined in Eq. 1.2. The kinetic energy of the auxiliary system as a functional of charge density is

$$T_s[n(\mathbf{r})] = -1/2 \sum_{i=1}^N \langle \chi_i | \nabla_i^2 | \chi_i \rangle, \quad (1.13)$$

and the Hartree energy or the electrostatic potential energy of noninteracting electrons is

$$E_{\text{H}}[n(\mathbf{r})] = \frac{1}{2} \int \int \frac{n(\mathbf{r})n(\mathbf{r}')}{|\mathbf{r} - \mathbf{r}'|} \, d\mathbf{r} \, d\mathbf{r}'. \quad (1.14)$$

Using Eqs. 1.13 and 1.14, which are uniquely determined by n , we can write HK functional in Eq. 1.12 as

$$E_{\text{HK}}[n(\mathbf{r})] = T_s[n(\mathbf{r})] + \int V_{\text{ext}}(\mathbf{r})n(\mathbf{r}) \, d\mathbf{r} + E_{\text{H}}[n(\mathbf{r})] + E_{\text{XC}}[n(\mathbf{r})], \quad (1.15)$$

where the exchange-correlation functional $E_{\text{XC}}[n(\mathbf{r})]$ is the missing energy contribution, which has to be approximated. One can then calculate the ground-state charge density and energy by minimising the HK energy in Eq. 1.15 with respect to the KS orbitals subject to the constraint that they remain orthonormal.

A simple approximation to describe the exchange-correlation functional is the local-density approximation (LDA) [12]

$$E_{\text{XC}}^{\text{LDA}}[n(\mathbf{r})] = \int \epsilon_{\text{XC}}^{\text{LDA}}(n(\mathbf{r})) n(\mathbf{r}) \, d\mathbf{r}, \quad (1.16)$$

where $\epsilon_{\text{XC}}^{\text{LDA}}(n)$ is the XC energy per electron of an interacting homogenous electron

gas (HEG). This approximation works well when the distribution of electrons is slowly varying; however, DFT-LDA does not correctly describe long-range nonlocal correlation [13]. Another widely-used XC energy functional is the Perdew-Burke-Ernzerhof (PBE) [14] functional with an XC energy of the form:

$$E_{\text{XC}}^{\text{PBE}}[n(\mathbf{r})] = \int \epsilon_{\text{XC}}^{\text{PBE}}(n(\mathbf{r}), \nabla n(\mathbf{r})) n(\mathbf{r}) \, \text{d}\mathbf{r}, \quad (1.17)$$

where the semilocal $\epsilon_{\text{XC}}^{\text{PBE}}(n, \nabla n)$ is not only dependent on the electron density but also on its gradient. Unlike the LDA, the PBE functional takes into account the fact that the XC hole in an inhomogeneous system is “off centre” with respect to the electron it surrounds.

Hybrid functionals are another class of approximations in which the XC energy incorporates a portion of exact exchange from HF theory with exchange and correlation parameterised using results from *ab initio* calculations or empirical data. Hybrid functionals describe a wide range of molecular properties accurately; however, calculating the exact HF exchange is computationally expensive. Becke, 3-parameter, Lee-Yang-Parr (B3LYP) [15, 16] and Heyd–Scuseria–Ernzerhof (HSE06) [17, 18] are two common examples of hybrid functionals that we have used. The B3LYP XC functional is of the form:

$$E_{\text{XC}}^{\text{B3LYP}}[n(\mathbf{r})] = \int \epsilon_{\text{XC}}^{\text{B3LYP}}(n(\mathbf{r}), \nabla^2 n_2(\mathbf{r})) n(\mathbf{r}) \, \text{d}\mathbf{r}, \quad (1.18)$$

where $\epsilon_{\text{XC}}^{\text{B3LYP}}(n, \nabla^2 n_2)$ is expressed in terms of the electron density and a Laplacian of the diagonal element of the second-order HF density matrix $n_2(\mathbf{r})$. Unlike B3LYP, the HSE06 functional,

$$E_{\text{XC}}^{\text{HSE06}}[n(\mathbf{r})] = \int \left\{ \epsilon_{\text{XC}}^{\text{PBE}}(n(\mathbf{r}), \nabla n(\mathbf{r})) - \epsilon_{\text{XC}}^{\text{HSE06,SR}}(n(\mathbf{r}), \nabla n(\mathbf{r})) \right\} n(\mathbf{r}) \, \text{d}\mathbf{r}, \quad (1.19)$$

screens the long-range part of the HF exchange by subtracting $\epsilon_{\text{XC}}^{\text{HSE06,SR}}(n, \nabla n)$, a short-range (SR) screened Coulomb potential, from the PBE XC. The HSE06

functionals solves the problem of singularities in the derivative of the orbital energies with respect to k . This singularity is caused by the divergence at $k = 0$ of the Fourier transform of the $1/r$ Coulomb potential.

Currently DFT is the most popular way to include the effects of electron correlation in first-principles calculations. This method is, in reality, fast but does have a certain number of well-known limitations and is in principle only valid for ground-state calculations. If the XC functional were exact, the ground-state energy and charge density would be exact. But the approximate mathematical form of the XC functional causes inaccuracy in the method. DFT often gives qualitatively wrong answers for systems such as excited states, highly correlated and vdW structures. Moreover, the calculated band gap in DFT is always smaller than its experimental value in semiconductors or insulators, where the host electrons cannot completely screen one additional electron in the limit of a large number of electrons because of the existence of the finite energy gap.

1.5 Basis sets

To solve the HK equation in Eq. 1.15, we need to expand the noninteracting wave function in a basis set. According to the Bloch's theorem, the electronic wave function consists of a wavelike part and a cell-periodic part [19].

$$\chi_{i,\mathbf{k}}(\mathbf{r}) = e^{i\mathbf{k}\cdot\mathbf{r}}u_{i,\mathbf{k}}(\mathbf{r}), \quad (1.20)$$

where the wave vectors \mathbf{k} go over the reciprocal lattice vectors of the primitive cell. The cell-periodic part of the wave function at each \mathbf{k} point can be expanded in terms of a discrete plane-wave basis set,

$$u_{i,\mathbf{k}}(\mathbf{r}) = \sum_{\mathbf{G}} c_{i,\mathbf{G}}(\mathbf{k})e^{i\mathbf{G}\cdot\mathbf{r}}, \quad (1.21)$$

where $c_{i,\mathbf{G}}$ are the expansion coefficients and the reciprocal lattice vectors \mathbf{G} are defined by $\mathbf{G} \cdot \mathbf{l} = 2\pi m$ for all \mathbf{l} lattice vector of the crystal and m integers. Therefore each electronic wave function can be written as a sum of plane waves,

$$\chi_{i,\mathbf{k}}(\mathbf{r}) = \sum_{\mathbf{G}} c_{i,\mathbf{k}+\mathbf{G}}(\mathbf{k}) e^{i(\mathbf{k}+\mathbf{G})\cdot\mathbf{r}}. \quad (1.22)$$

Plane waves are a kind of basis set appropriate for periodic systems and in principle, an infinite number of plane waves is required to expand the electronic wave functions at each \mathbf{k} point. However, the coefficients $c_{i,\mathbf{k}+\mathbf{G}}$ for the plane waves with small kinetic energy $(1/2)|\mathbf{k} + \mathbf{G}|^2$ are typically more important than those with large kinetic energy [13]. Hence the plane-wave basis set can be truncated to include only plane waves having kinetic energies smaller than some particular cutoff energy $(1/2)|\mathbf{k}_{\max}|^2$. The truncation at a finite cutoff energy leads to an error in the computed total energy and its derivatives. It is possible to reduce the magnitude of the error in a systematic way by increasing the value of the cutoff energy until the calculated total energy converges within the required tolerance.

In QMC calculations, we use simulation cells, whose translation vectors is $m_1\mathbf{b}_1 + m_2\mathbf{b}_2 + m_3\mathbf{b}_3$, where m_i are integers and \mathbf{b}_i are the primitive vectors of the crystal. If the simulation cell consists of one primitive cell, the first Brillouin zone of the primitive lattice contains a grid of $m_1 \times m_2 \times m_3$ points with the same (reduced) value of \mathbf{k} . The grid of \mathbf{k} -point becomes finer as the simulation cell is made larger and is analogous to the k -point sampling grids used in independent-electron calculations.

Nonlocality of the plane-wave basis set in QMC increases the scaling with system size, which requires the storage proportional to N^2 for electronic orbitals. This problem can be overcome using a localised basis set such as a B-spline (blip) basis [20] on a uniform cubic grid spacing $a = \pi/(2k_{\max})$. The single particle orbitals centred on the grid point at position (X_s, Y_s, Z_s) are therefore represented in terms

of blip function using $\chi_i(\mathbf{r}) = \sum_s c_{is} \phi((x - X_s)/a) \phi((y - Y_s)/a) \phi((z - Z_s)/a)$, where coefficients c_{is} are evaluated by comparing the relationship between B-splines and plane-wave and $\phi(\zeta)$ are

$$\phi(\zeta) = \begin{cases} 1 - \frac{3}{2}\zeta^2 + \frac{3}{4}|\zeta|^3 & 0 \leq |\zeta| \leq 1 \\ \frac{1}{4}(2 - |\zeta|)^3 & 1 < |\zeta| \leq 2 \end{cases}.$$

For any position \mathbf{r} , there are only 64 non-zero blips, which increases the efficiency of calculations.

Another kind of basis functions that can be used in electronic structure calculations are Gaussian basis sets, which are represented as a linear combination of Gaussian primitives,

$$\chi_i(\mathbf{r}) = x^a y^b z^c e^{-\alpha r^2}, \quad (1.23)$$

where α as the Gaussian orbital exponent controls the width of orbitals and a , b and c control angular momentum $l = a + b + c$. Eq. 1.23 can be combined with a periodic images modulated by a phase factor to represent the periodicity of the system. QMC calculations scale better with system size while using Gaussian rather than plane-wave basis sets. Gaussian basis sets also do not require pseudopotentials and periodic boundary conditions, even for isolated molecules however they show basis set superposition errors (BSSE). For example, as two monomers approach each other, the dimer can be artificially stabilised to describe the electronic distribution of each monomer using the extra basis functions from the other one. The error arises from the fact that each monomer accesses additional functions from the other monomer at shorter intermolecular distances whereas at large intermolecular distances, the overlap integrals are too small to provide stabilisation. The energy mismatch due to the short-range and long-range interactions introduces an error.

1.6 Quantum Monte Carlo methods

Quantum Monte Carlo (QMC) simulation is a powerful tool in understanding the properties and behaviour of systems with fewer than 1000 electrons because it involves an explicit treatment of electron correlation and stochastically solves the many-body Schrödinger equation. QMC methods can be used for quantitative calculations of important quantities such as total energies, charge densities, pair-correlation functions and momentum densities for molecules and crystals. These methods have many attractive features for probing the properties of homogeneous electron gases, equations of state, phase transitions, lattice defects, surface phenomena, excited states and band structures [21].

There are many different QMC methods, but we concentrate on the two that we have used: variational quantum Monte Carlo (VMC) and diffusion quantum Monte Carlo (DMC). The VMC method is the calculation of expectation values via Monte Carlo integration over the $3N$ -dimensional space of electron coordinates. By contrast, the DMC method is a projector approach, in which a stochastic imaginary-time evolution is used to improve a starting trial wave function. The VMC and DMC methods are best suited to calculating total energies, because these have the very advantageous zero-variance property: as the trial wave function approaches the exact ground state (or any other exact energy eigenstate) the statistical fluctuations in the energy estimate reduce to zero. The VMC and DMC methods are less well-adapted to study excited states, but have nevertheless been used successfully to calculate a wide range of excited-state properties of atoms, molecules, and solids. These methods are able to simulate only one state at a time, so determining a spectrum of excited states is expensive [22]. The computational time required to calculate the total energy of a system to some given accuracy using the fermion VMC and DMC methods effectively scales as N^3 [22]. The advantageous scaling with system size means that the attainable accuracy does not fall off rapidly as the number of electrons N increases.

In the rest of this section, we describe the general idea of Monte Carlo integration, the VMC method, the DMC method and backflow transformations.

1.6.1 Monte Carlo integration

Monte Carlo (MC) integration is a robust method for a wide range of high-dimensional numerical integration problems. MC integration converges at a rate of $M^{-1/2}$ independent of the dimension of the integral, where M is the number of random samples. For example, suppose

$$I = \int_{\Omega} f(\mathbf{R}) \, d\mathbf{R}, \quad (1.24)$$

where \mathbf{R} is a multi-dimensional vector, $f(\mathbf{R})$ is a nontrivial function and Ω is the region in which we are interested. By decomposing $f(\mathbf{R})$ into a product of a real valued function, $g(\mathbf{R})$ and a probability density function, $P(\mathbf{R})$, I in Eq. 1.24 can be transformed into an integral of the form

$$I = \int_{\Omega} g(\mathbf{R})P(\mathbf{R}) \, d\mathbf{R} \approx \frac{1}{M} \sum_{i=1}^M g(\mathbf{R}_i). \quad (1.25)$$

This transformation is called “importance sampling”, because $g(\mathbf{R})$ is averaged over sampling points that are determined by a positive probabilistic weight $P(\mathbf{R})$ that may be chosen to be large when $|f|$ is large. As the number of sampling points grows, the estimate of the integral becomes increasingly accurate. In general, considering a function $w(\mathbf{R}) \approx |f(\mathbf{R})|$ and choosing $P(\mathbf{R})$ to be the normalised form

$$P(\mathbf{R}) = \frac{w(\mathbf{R})}{\int w(\mathbf{R}) \, d\mathbf{R}}, \quad (1.26)$$

greatly reduces the fluctuations in $g(\mathbf{R})$ that were originally present in $f(\mathbf{R})$, because the summand in Eq. 1.25 is almost a constant as can be seen by considering $g(\mathbf{R}) = f(\mathbf{R})/P(\mathbf{R})$. Assuming the samples are independent, the standard error

in the estimate of Eq. 1.25 is σ/\sqrt{M} , where

$$\sigma^2 \simeq \frac{1}{M-1} \sum_{i=1}^M (g(\mathbf{R}_i) - \langle g(\mathbf{R}) \rangle)^2. \quad (1.27)$$

An efficient way to generate configurations $\{\mathbf{R}_i\}$ distributed according to $P(\mathbf{R})$ is the ‘‘Metropolis algorithm’’ [23]. This algorithm is based on a random walk in the space of the dynamic variable \mathbf{R} . The Metropolis algorithm starts from a random position \mathbf{R} and takes the following steps:

1. Propose a move, $\mathbf{R}' \leftarrow \mathbf{R}$, with the transition probability density $T(\mathbf{R}' \leftarrow \mathbf{R})$, which defines the probability that each particle i moves from $\{\mathbf{r}_i\}$ to $\{\mathbf{r}'_i\}$. The function $T(\mathbf{R}' \leftarrow \mathbf{R})$ affects the efficiency of performing the MC integration. A common choice of T is a Gaussian whose width can be varied to find the maximum efficiency.
2. Accept the move with the following probability

$$P_{\text{accept}}(\mathbf{R}' \leftarrow \mathbf{R}) = \min \left\{ 1, \frac{T(\mathbf{R} \leftarrow \mathbf{R}')P(\mathbf{R}')}{T(\mathbf{R}' \leftarrow \mathbf{R})P(\mathbf{R})} \right\}, \quad (1.28)$$

where the normalisation part of P cancels out.

3. Depending on the acceptance or rejection of the new random move, the new position is respectively \mathbf{R}' or \mathbf{R} . This position is added to the set of configurations \mathbf{R}_i . Return to step 1 to propose the next move and repeat until the required number of samples have been collected.

1.6.2 Slater–Jastrow wave function

The wave function can always be chosen to be real for systems with time-reversal symmetry, which have real Hamiltonians with appropriate boundary conditions. An appropriate trial wave function $\psi_T(\mathbf{X})$ must have the proper symmetry and

include as accurate a description of correlations as possible. Fermion wave functions must be antisymmetric under the exchange of positions of same-spin electrons however ground state boson spatial wave function needs a bosonic symmetry. A single-determinant Slater–Jastrow (SJ) wave function for a fermionic system is

$$\psi_T(\mathbf{X}) = e^{J(\mathbf{X})}\Psi_S(\mathbf{X}), \quad (1.29)$$

where J is the Jastrow factor and Ψ_S is the Slater determinant shown in Eq. 1.2. The single-particle orbitals in the Slater determinants come from a HF code or a DFT code such as CASTEP. The spin variables in Eq. 1.29 can be removed from $\mathbf{X} = (\mathbf{r}, \sigma)$ using a product of determinants of up-spin and down-spin orbitals,

$$\psi_T(\mathbf{R}) = e^{J(\mathbf{R})}\Psi_S^\uparrow(\mathbf{r}_1, \dots, \mathbf{r}_{N_\uparrow})\Psi_S^\downarrow(\mathbf{r}_{N_\uparrow+1}, \dots, \mathbf{r}_N), \quad (1.30)$$

where $\mathbf{R} = (\mathbf{r}_1, \mathbf{r}_2, \dots, \mathbf{r}_N)$ is a $3N$ -dimensional spacial coordinates of electrons. The Jastrow factor $J(\mathbf{R})$ is a symmetric function of the coordinates and contains free optimisable parameters. We have used a general form of the Jastrow function,

$$J(\mathbf{R}) = \frac{1}{2} \sum_{i \neq j}^N u(r_{ij}) + \sum_i^N \sum_I^{N_n} \chi_I(r_{iI}) + \frac{1}{2} \sum_{i \neq j}^N \sum_I^{N_n} f_I(r_{ij}, r_{iI}, r_{jI}) + \frac{1}{2} \sum_{i \neq j}^N p(\mathbf{r}_{ij}), \quad (1.31)$$

where the isotropic functions of u , χ and f are polynomials describing electron–electron correlations, electron–nucleus correlations, and electron–electron–nucleus correlations, respectively and p are cusp-less plane-wave expansions for electron–electron separations.

The SJ wave function in Eq. 1.30 can satisfy the electron–electron “cusp” condition [24, 25]. When two opposite-spin electrons approach one another, the local energy $\hat{H}\psi_T/\psi_T$ diverges due to the divergence in the Coulomb potential. Since the wave function must remain an eigenstate of Hamiltonian, the divergence of the potential at the coalescence point must be canceled out by an equal and opposite divergence

in the kinetic energy. The cusp condition can be imposed on parallel-spin electron pairs as well because the local energy must be finite when $\psi_T = 0$ for two like-spin electrons. The general Kato cusp condition for two arbitrary particles of charges q_i and q_j and masses m_i and m_j , interacting by the Coulomb interaction, is

$$\left. \frac{dJ(\mathbf{R})}{dr_{ij}} \right|_{r_{ij}=0} = \frac{2q_i q_j \mu_{ij}}{d \pm 1}, \quad (1.32)$$

where $\mu_{ij} = m_i m_j / (m_i + m_j)$ and d is the dimensionality. The minus and plus signs are used for distinguishable and indistinguishable particles, respectively. Fig. 1.1 shows the effect of cusp correction on the local energy of a biexciton calculated using SJ wave functions, where the electrons and holes are distinguishable and interact with the Coulomb interaction: it is clear that the divergence in the local energy is removed by using the cusp correction in SJ wave function that satisfies Eq. 1.32. In chapter four, we will describe wave function forms for a biexciton in a 2D semiconductor.

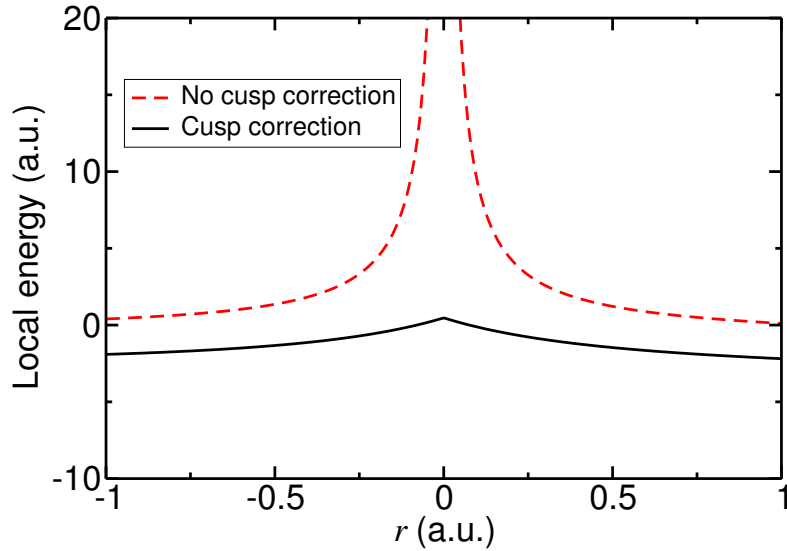


Figure 1.1: Local energy of a 2D biexciton against the separation of two like-spin electrons, r . SJ wave function is used for the particles interacting with Coulomb interaction.

1.6.3 Variational quantum Monte Carlo method

Variational quantum Monte Carlo (VMC) is based on the variational principle for the quantum mechanical zero-temperature ground state. The expectation value of the Hamiltonian with respect to the trial wave function can be evaluated as

$$E_{VMC} = \frac{\langle \psi_T(\mathbf{R}) | \hat{H} | \psi_T(\mathbf{R}) \rangle}{\langle \psi_T(\mathbf{R}) | \psi_T(\mathbf{R}) \rangle} = \frac{\int |\psi_T(\mathbf{R})|^2 E_L(\mathbf{R}) d\mathbf{R}}{\int |\psi_T(\mathbf{R})|^2 d\mathbf{R}} \geq E_0, \quad (1.33)$$

where E_{VMC} provides an upper bound to the exact ground-state energy, E_0 . Eq. 1.33 utilises an importance sampling transformation, where $|\psi_T(\mathbf{R})|^2 / (\int |\psi_T(\mathbf{R})|^2 d\mathbf{R})$ can be interpreted as a probability distribution function at \mathbf{R} , which is sampled by the Metropolis algorithm. Since \hat{H} is an operator, the quantity that is averaged will be the local energy

$$E_L(\mathbf{R}) = \hat{H}\psi_T(\mathbf{R})/\psi_T(\mathbf{R}), \quad (1.34)$$

with variance

$$\sigma^2 = \frac{\int |\psi_T(\mathbf{R})|^2 |E_L(\mathbf{R}) - E_{VMC}|^2 d\mathbf{R}}{\int |\psi_T(\mathbf{R})|^2 d\mathbf{R}}. \quad (1.35)$$

The VMC method is based on Eqs. 1.33– 1.35 and the best ψ_T can be obtained by minimising σ or E_{VMC} with respect to the wave function parameters. The optimisation of wave functions within the VMC method is the most difficult technical aspect of QMC. Ideally, if ψ_T is the exact ground-state wave function, the local energy $E_L(\mathbf{R})$ tends to the ground-state energy and $\sigma^2 \rightarrow 0$; the trial wave function should therefore be chosen to make the local energy as constant as possible.

The problem with Eq. 1.35 is that the weight $|\psi_T(\mathbf{R})|^2 / (\int |\psi_T(\mathbf{R})|^2 d\mathbf{R})$ varies exponentially between electron configurations as the parameters change, resulting in instabilities in optimisation procedures. “Unreweighted variance minimisation” [26, 27] solves this problem by introducing the following variance for a set of M configurations $\{\mathbf{R}\}$ distributed according to the initial $|\psi_T(\mathbf{R})|^2$ (we rewrite

the trial wave function as $\psi_T^{\{N_{opt}\}}(\mathbf{R})$ to denote that it depends on a set of free parameters $\{N_{opt}\}$:

$$\sigma_u^2 = \frac{1}{M-1} \sum_{i=1}^M (E_L^{\{N_{opt}\}}(\mathbf{R}_i) - \bar{E}_u)^2, \quad (1.36)$$

where the unweighted energy \bar{E}_u is the mean value of the local energy.

$$\bar{E}_u = \frac{1}{M} \sum_{i=1}^M E_L^{\{N_{opt}\}}(\mathbf{R}_i). \quad (1.37)$$

The local energy in Eq. 1.34 with respect to $\psi_T^{\{N_{opt}\}}(\mathbf{R})$, together with Eqs. 1.36 and 1.37 are the fundamentals of the unweighted variance optimisation method.

We can also use linear-least-squares (LLS) energy minimisation methods [28–30] to optimise the trial wave function. If we employ N -electron wave functions, which depend on N_{opt} variational parameters collectively denoted by $\boldsymbol{\alpha}_0 = (c, w, q)$, the trial wave function for all M configurations $\{\mathbf{R}_m\}$ may be of the form

$$\psi_T(\boldsymbol{\alpha}_0, \mathbf{R}_m) = e^{J(w, \mathbf{R})} \sum_p c_p \Psi_p(q, \mathbf{R}_m), \quad (1.38)$$

where J is a Jastrow factor including a set of free parameters $\{w\}$ defined in Eq. 1.31, $\sum_p c_p \Psi_p(q, \mathbf{R}_m)$ is a linear combination of Slater determinants of single-particle orbitals with coefficients of $\{c_p\}$ and q nonlinear expansion coefficients of the orbital. It is possible that the trial wave function becomes zero for some variables q causes local energy to diverge when the nodal surface moves through a sampled configuration. To solve the divergence problem in the variational wave-function optimisation, suppose the wave function involves a set of free parameters $\boldsymbol{\alpha}_0$ which changes to $\boldsymbol{\alpha} = \boldsymbol{\alpha}_0 + \delta\boldsymbol{\alpha}$ in each optimisation cycle. The new wave

function is a Taylor expansion in terms of $\delta\boldsymbol{\alpha}$:

$$\begin{aligned}\psi'_T(\boldsymbol{\alpha}, \mathbf{R}_m) &= \psi_T(\boldsymbol{\alpha}_0, \mathbf{R}_m) + \sum_{i=1}^{N_{opt}} \delta\alpha_i \left. \frac{\partial\psi_T(\boldsymbol{\alpha}, \mathbf{R}_m)}{\partial\alpha_i} \right|_{\boldsymbol{\alpha}=\boldsymbol{\alpha}_0} + \mathcal{O}([\delta\boldsymbol{\alpha}]^2) \\ &\simeq \sum_{i=1}^{N_{opt}} a_i \phi_i \quad (\text{for small } \delta\boldsymbol{\alpha}),\end{aligned}\tag{1.39}$$

where the coefficients $\{a_i\}$ and the basis functions $\{\phi_i\}$ are defined as:

$$a_i = \begin{cases} 1 & i = 0 \\ \delta\alpha_i & i \neq 0 \end{cases}\tag{1.40}$$

$$\phi_i = \begin{cases} \psi_T(\boldsymbol{\alpha}_0, \mathbf{R}_m) & i = 0 \\ \left. \frac{\partial\psi_T(\boldsymbol{\alpha}, \mathbf{R}_m)}{\partial\alpha_i} \right|_{\boldsymbol{\alpha}=\boldsymbol{\alpha}_0} & i \neq 0. \end{cases}\tag{1.41}$$

ψ'_T has an $(N_{opt} + 1)$ -dimensional basis formed by the wave function and its derivatives. According to standard diagonalisation on an infinite MC sample, minimising $\langle\psi'_T|\hat{H}|\psi'_T\rangle$ with respect to \mathbf{a} subject to the constraint $\langle\psi'_T|\psi'_T\rangle = \text{constant}$ results in the general eigenvalue equation $(H - ES)\mathbf{a} = 0$, where $H_{ij} = \langle\phi_i|\hat{H}|\phi_j\rangle$, $S_{ij} = \langle\phi_i|\phi_j\rangle$ are the elements of the overlap matrix, and E is an eigenvalue. The lowest eigenvalue gives the lowest-energy state that can be constructed from the basis functions, and the corresponding eigenvector gives the coefficients for this state.

In practice, we look for eigenstates of \hat{H} on a finite MC sample of configurations $\{\mathbf{R}_m\}$ by considering the action of \hat{H} on basis sets $\{\phi_i\}$. Assume that the basis functions span an invariant subspace of the Hamiltonian, which means the action of \hat{H} on any basis sets leads to a linear combination of all the basis sets.

$$\hat{H}|\phi_i\rangle = \sum_{j=0}^{N_{opt}} \mathcal{E}_{ji}|\phi_j\rangle \quad \forall i,\tag{1.42}$$

where \mathcal{E}_{ji} are coefficients. Once \mathcal{E} is determined, $\delta\boldsymbol{\alpha}$ can be found by solving $\mathcal{E}\mathbf{a} = E\mathbf{a}$. To solve Eq. 1.42 and obtain acceptable statistical errors, we use a

least-squares [28] fit by minimising:

$$\chi^2 = \sum_{m=1}^M \sum_{i=0}^{N_{opt}} \left| \frac{\hat{H}\phi_i(\mathbf{R}_m) - \sum_{j=0}^{N_{opt}} \mathcal{E}_{ji}\phi_j(\mathbf{R}_m)}{\psi_T(\boldsymbol{\alpha}_0, \mathbf{R}_m)} \right|^2, \quad (1.43)$$

with respect to $\{\mathcal{E}_{ji}\}$. Suppose $\phi_{mi} = \phi_i(\mathbf{R}_m)/\psi_T(\boldsymbol{\alpha}_0, \mathbf{R}_m)$ and $\phi_{mi}^H = \hat{H}\phi_i(\mathbf{R}_m)/\psi_T(\boldsymbol{\alpha}_0, \mathbf{R}_m)$.

Then $\frac{\partial \chi^2}{\partial \mathcal{E}_{pq}} = 0$ gives

$$\sum_{m=1}^M \left(\phi_{mi}^H - \sum_{j=0}^{N_{opt}} \mathcal{E}_{ji}\phi_{mj} \right) \phi_{mp}^* = 0, \quad (1.44)$$

therefore $\mathcal{E} = (\phi^\dagger \phi)^{-1} \phi^\dagger \phi^H$. In the VMC estimates and the limit of $M \rightarrow \infty$, $\phi^\dagger \phi$ and $\phi^\dagger \phi^H$ are proportional to S and H , respectively. In the limit of perfect sampling, standard diagonalisation and linear-least-squares optimisation solve the same eigenproblem. By finding $\delta \boldsymbol{\alpha}$ and optimising the parameters appear in Eq. 1.39, the trial wave function will be optimised and the energy will converge to a local minimum.

1.6.4 Theory of diffusion quantum Monte Carlo

The quality of results obtained using the VMC method is entirely determined by the quality of the trial wave function. By contrast, the diffusion quantum Monte Carlo (DMC) wave function is generated stochastically, leading to results that are largely free of errors caused by limited basis sets and so on. DMC is the most accurate first-principles total-energy method for systems with a few hundreds of electrons. The aim of using DMC is solving the imaginary-time many-body

Schrödinger equation (ITSE):

$$\begin{aligned}
-\frac{\partial\Phi(\mathbf{R},\tau)}{\partial\tau} &= [\hat{H} - E_T]\Phi(\mathbf{R},\tau) \\
&= -\frac{1}{2}\nabla^2\Phi(\mathbf{R},\tau) + (U(\mathbf{R}) - E_T)\Phi(\mathbf{R},\tau),
\end{aligned}
\tag{1.45}$$

where $\Phi(\mathbf{R},\tau)$ is a function of configuration \mathbf{R} and imaginary time $\tau = it$, $U(\mathbf{R})$ is the potential energy and E_T is an energy offset. A general solution of Eq. 1.45 is

$$\Phi(\mathbf{R},\tau) = \sum_{i=0}^{\infty} c_i \phi_i(\mathbf{R}) e^{-(E_i - E_T)\tau},
\tag{1.46}$$

where E_i and $\phi_i(\mathbf{R})$ are the i th eigenvalue and eigenfunction of the Hamiltonian \hat{H} . In the limit $\tau \rightarrow \infty$, if $E_T = E_0$, and the initial conditions have $c_0 \neq 0$, the ground state is projected out to $\lim_{\tau \rightarrow \infty} \Phi(\mathbf{R},\tau) = c_0 \phi_0(\mathbf{R})$.

Eq. 1.45 without the second term in the second line describes random diffusion of “walkers”; without the first term of Eq. 1.45 results in exponential term. The simulation of Eq. 1.45 by a random walk is inefficient because of the divergences in the branching rate $(U - E_T)$ due to the Coulomb interaction. These divergences lead to large fluctuations in the configuration population and hence large statistical uncertainties in expectation values. These fluctuations can be reduced by a variant of the MC technique of importance sampling described in Sec. 1.6.1. In this procedure, one constructs an analytical trial function, $\psi_T(\mathbf{R})$, based on any available knowledge of ground-state wave function. Here, $\psi_T(\mathbf{R})$ is of the form given in Eq.1.30 with a VMC-optimised Jastrow factor. The trial function is then used to bias the random walk to produce the probability distribution function $f(\mathbf{R},\tau) = \Phi(\mathbf{R},\tau)\psi_T(\mathbf{R})$ rather than $\Phi(\mathbf{R},\tau)$. Substituting $\Phi(\mathbf{R},\tau) = \psi_T^{-1}(\mathbf{R})f(\mathbf{R},\tau)$ into Eq. 1.45 results in the importance-sampled imaginary time Schrödinger equation (ISITSE),

$$-\frac{1}{2}\nabla^2 f(\mathbf{R},\tau) + \nabla \cdot [\mathbf{V}(\mathbf{R})f(\mathbf{R},\tau)] + [E_L(\mathbf{R}) - E_T]f(\mathbf{R},\tau) = -\frac{\partial f(\mathbf{R},\tau)}{\partial\tau},
\tag{1.47}$$

where $\mathbf{V}(\mathbf{R}) = \psi_T^{-1}(\mathbf{R})\nabla\psi_T(\mathbf{R})$ is the drift velocity, which modifies the diffusion process. The advantage of having $E_L(\mathbf{R})$, the local energy defined in Eq. 1.34, in the branching term is that the singularities in the potential energy are avoided. The local energy has both kinetic and potential energy and is much smoother than the potential energy alone. Eq. 1.47 without the third term in the left hand side is a Fokker–Planck (FP) equation, which describes the time evolution of the density of a set of particles under random diffusion in $3N$ -dimensional fluid of velocity field \mathbf{V} . Eq. 1.47 without the first two terms is the branching factor, which gives an exponential growth or decay in the density of particles at each point in the $3N$ -dimensional configuration space. The FP equation is

$$\begin{aligned}
-\frac{1}{2}\nabla^2 f(\mathbf{R}) + \nabla\cdot[\mathbf{V}(\mathbf{R})f(\mathbf{R})] &= -\frac{1}{2}\nabla^2 \int \langle \mathbf{R}|\mathbf{P}\rangle \langle \mathbf{P}|f\rangle d\mathbf{P} \\
&+ \nabla\cdot \int \langle \mathbf{R}|\mathbf{P}\rangle \langle \mathbf{P}|\mathbf{V}(\hat{\mathbf{R}})|f\rangle d\mathbf{P} \\
&= \frac{1}{2} \langle \mathbf{R}|\hat{\mathbf{P}}^2|f\rangle + i \langle \mathbf{R}|[\hat{\mathbf{P}}\cdot\mathbf{V}(\hat{\mathbf{R}})]|f\rangle \\
&= \langle \mathbf{R}|\hat{F}|f\rangle, \tag{1.48}
\end{aligned}$$

where $\hat{F} = (1/2)\hat{\mathbf{P}}^2 + i\hat{\mathbf{P}}\cdot\mathbf{V}(\hat{\mathbf{R}})$ is the FP operator, $\hat{\mathbf{P}}$ is the momentum operator and $\langle \mathbf{R}|\mathbf{P}\rangle = \exp(i\mathbf{P}\cdot\mathbf{R})/(2\pi)^{3N/2}$ for N particles.

The integral form of ISITSE (Eq. 1.47) is

$$f(\mathbf{R}', \tau + \delta\tau) = \int G(\mathbf{R}' \leftarrow \mathbf{R}, \delta\tau) f(\mathbf{R}, \tau) d\mathbf{R}, \tag{1.49}$$

where $\delta\tau$ is an interval in imaginary time. The exact form of Green's function,

$$G(\mathbf{R}' \leftarrow \mathbf{R}, \delta\tau)_{\text{exact}} = \langle \mathbf{R}'|e^{-\delta\tau(\hat{F}+E_L(\hat{\mathbf{R}})-E_T)}|\mathbf{R}\rangle, \tag{1.50}$$

is not explicitly known, however we can construct an approximation using Suzuki–

Trotter expansion [31]

$$\begin{aligned}
G(\mathbf{R}' \leftarrow \mathbf{R}, \delta\tau)_{\text{exact}} &= \langle \mathbf{R}' | e^{-\delta\tau(\hat{F} + E_L(\hat{\mathbf{R}}) - E_T)} | \mathbf{R} \rangle \\
&= \langle \mathbf{R}' | e^{-\delta\tau \frac{E_L(\hat{\mathbf{R}}) - E_T}{2}} e^{-\delta\tau \hat{F}} e^{-\delta\tau \frac{E_L(\hat{\mathbf{R}}) - E_T}{2}} + \mathcal{O}(\delta\tau^3) | \mathbf{R} \rangle \\
&\approx e^{-\delta\tau \frac{E_L(\mathbf{R}') - E_T}{2}} \langle \mathbf{R}' | e^{-\delta\tau \hat{F}} | \mathbf{R} \rangle e^{-\delta\tau \frac{E_L(\mathbf{R}) - E_T}{2}}, \tag{1.51}
\end{aligned}$$

which is accurate for $\delta\tau \rightarrow 0$. The last line of Eq. 1.51 can be rewritten as

$$\begin{aligned}
G(\mathbf{R}' \leftarrow \mathbf{R}, \delta\tau)_{\text{approx}} &\approx G_D(\mathbf{R}' \leftarrow \mathbf{R}, \delta\tau) G_B(\mathbf{R}' \leftarrow \mathbf{R}, \delta\tau) \\
&= \frac{1}{(2\pi\delta\tau)^{3N/2}} \exp\left[-\frac{|\mathbf{R}' - \mathbf{R} - \delta\tau \mathbf{V}(\mathbf{R})|^2}{2\delta\tau}\right] \\
&\quad \times \exp\left[-\frac{\delta\tau}{2}(E_L(\mathbf{R}') + E_L(\mathbf{R}) - 2E_T)\right], \tag{1.52}
\end{aligned}$$

where G_D is the drift-diffusion Green's function and G_B is the branching factor. The DMC Green's function therefore describes the evolution of the density of a set of particles drifting and breeding or dying in a $3N$ -dimensional space. Nevertheless, as $\delta\tau \rightarrow 0$, $G_D G_B$ converges to the exact Green's function and any initial distribution of walkers will converge to the ground state [32]. After a certain number of iterations, the excited state components of f die away; hence $f(\mathbf{R}) = \phi_0(\mathbf{R})\psi_T(\mathbf{R})$ has a mixed distribution and the ground-state energy can be evaluated by the ‘‘mixed estimator’’,

$$E_0 = \frac{\langle \phi_0 | \hat{H} | \psi_T \rangle}{\langle \phi_0 | \psi_T \rangle} = \lim_{\tau \rightarrow \infty} \frac{\int f(\mathbf{R}, \tau) E_L(\mathbf{R}) \, d\mathbf{R}}{\int f(\mathbf{R}, \tau) \, d\mathbf{R}} \approx \frac{1}{M} \sum_{i=1}^M E_L(\mathbf{R}_i). \tag{1.53}$$

1.6.5 Sources of errors in VMC and DMC calculations

Random errors and serial correlations: The error bars in the VMC and DMC calculations are affected by serial correlations caused by the fact that the sampling points are not truly independent of each other. To balance the serial

correlation, the VMC time step is optimised by choosing the VMC transition probability distribution function such that around 50% of moves are accepted. The VMC time step is the variance of the probability distribution function used to generate the random displacement and in principle is a squared length, but can be considered as a time in a diffusion process. We also keep one configuration for every 16 proposed VMC moves and use reblocking analysis to analyse our VMC and DMC data [33]. Reblocking works by grouping the energies of M iterations into blocks of length X with the mean energy $\bar{E} = (1/M) \sum_{i=1}^M E(\{\mathbf{R}_i\})$. As an example, Fig. 1.2 shows how eight elements are transformed into four reblocked sets with the blocking length $X = 2$.

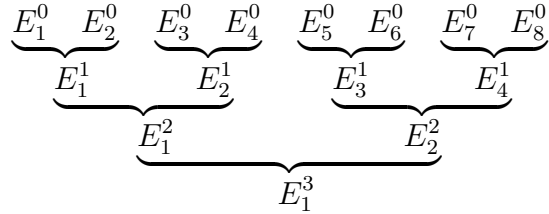


Figure 1.2: Reblocking eight elements into three blocking transformations.

The effect of a reblocking transformation on the variance for $X = 2$ is given by

$$\begin{aligned}
\sigma_{\bar{E}}'^2 &= \frac{\sum_{m=1}^{M/2} \left(\frac{E_{2m-1} + E_{2m}}{2} - \bar{E} \right)^2}{M/2(M/2 - 1)} = \frac{\sum_{m=1}^{M/2} (E_{2m-1} - \bar{E} + E_{2m} - \bar{E})^2}{M(M - 2)} \\
&= \frac{\sum_{m=1}^M (E_m - \bar{E})^2}{M(M - 2)} + \frac{2 \sum_{m=1}^{M/2} (E_{2m-1} - \bar{E})(E_{2m} - \bar{E})}{M(M - 2)} \\
&\approx \sigma_{\bar{E}}^2 + \frac{2 \sum_{m=1}^{M/2} (E_{2m-1} - \bar{E})(E_{2m} - \bar{E})}{M(M - 2)}. \tag{1.54}
\end{aligned}$$

If there is no serial correlation, the last term in Eq. 1.54 is a sum of numbers distributed around zero, which leads to $\sigma_{\bar{E}}'^2 \approx \sigma_{\bar{E}}^2$. When the variance as a function of reblocking transformation number reaches a plateau, the statistical error converges to the true variance and the reblocking transformation number beyond

the plateau is greater than the mean correlation time, which refers to the average number of MC steps between two uncorrelated values of the energy.

To reduce transient effects due to the initial distribution, the length of equilibration must be sufficiently large that the root mean square (RMS) distance diffused by a particle is of the order of the longest length scale in the system. The RMS distance is $\sqrt{2DdAN_{\text{equil}}\delta\tau}$, where $D = 1/(2m)$ is the diffusion constant for the particle mass m , which is 1 for electrons, d is the dimensionality, N_{equil} is the number of moves, A is the acceptance ratio, which is close to 1 in DMC and 1/2 in VMC, and $\delta\tau$ is the time step [34]. The first guess at a DMC time step can be 1/50 of the optimised VMC time step. In fact, the DMC time step $\delta\tau$ should be such that the RMS distance diffused over one time step, i.e. $\sqrt{2DdA\delta\tau}$, is small compared with the shortest length scale in the problem.

Time-step bias: Using the finite imaginary time step $\delta\tau$ in the Green's function of Eq. 1.52 is one of the approximations in DMC. These errors can largely be removed by extrapolating the DMC energy to zero time step.

Pseudopotentials: We have used pseudopotentials in our calculations resulting in an error which could in principle be removed by using an all-electron approach and a Gaussian basis set. The DF pseudopotentials used in our DMC calculations are nonlocal in a core region, which introduces the locality approximation.

Population-control bias: Using a small target configuration population in DMC calculations can cause biased results. Using a large configuration population in DMC has the advantage of reducing population-control bias, but it has the disadvantage of proportionately increasing the computational expense of equilibration, and if the duration of statistics accumulation is reduced, it becomes more difficult to eliminate the effects of serial correlation when calculating error bars.

Population-control bias is small in practice and can be removed by extrapolating the DMC energy to infinite populations.

Finite-size errors: Although the accuracy of QMC for total-energy calculations reaches 10^{-2} eV/atom, finite-size errors present a major challenge in studies of condensed matter. The finite-size errors are due to the limited number of unit cells in the simulation cell and single-particle finite-size errors because of momentum quantisation. The former error may be minimised by calculating the DMC energy for different sizes of supercell and extrapolating the energy to the infinite system size. The latter can also be reduced by averaging over offset to the grid of Bloch \mathbf{k} vectors.

Fixed-node error: The fermionic nature of many-electron systems imposes positive and negative regions in the antisymmetric wave function. This simple fact underlies the fermion sign problem, which troubles all projector QMC methods. Both $\Phi(\mathbf{R}, \tau)$ and $\psi_T(\mathbf{R})$ must have the same nodal surface otherwise there would be regions where $f(\mathbf{R}, \tau)$ is negative. In the importance sampling algorithm that we use, f as a probability distribution can never have a negative value. This fact introduces the DMC fixed-node approximation [35]. Fixed node approximations for fermionic systems is a consistent source of error, which is positive for fermions and may be improved by using backflow wave functions, which are briefly discussed in the next section.

1.6.6 Backflow transformations

The fixed-node DMC algorithm projects out the many-electron wave function with the lowest possible energy expectation value consistent with the fixed nodal surface. The nodal surface of a wave function $\Phi(\mathbf{R}, \tau)$ is the $(3N - 1)$ -dimensional surface on which $\Phi = 0$ and across which it changes sign. The fixed-node method is

computationally stable: DMC results are based on variational principle and not exact unless the trial nodal surface is exact. The Jastrow function $e^{J(\mathbf{R})}$ defined in Eq. 1.31 is always positive and does not move the nodes of a wave function.

Backflow (BF) transformation provides a way to move the nodal surface of a trial wave function by introducing further correlations which allow the orbitals to depend on the positions of other electrons [36–41]. BF correlations are introduced by substituting a set of collective coordinates $\{\mathbf{X}(\mathbf{R})\}$ for coordinates \mathbf{R} in the Slater determinants.

$$\Psi_{BF}(\mathbf{R}) = e^{J(\mathbf{R})}\Psi_S(\{\mathbf{X}(\mathbf{R})\}), \quad (1.55)$$

where $\mathbf{X}_i(\mathbf{R})$ is given by

$$\mathbf{X}_i(\mathbf{R}) = \mathbf{r}_i + \boldsymbol{\xi}_i(\{\mathbf{R}\}), \quad (1.56)$$

in which \mathbf{r}_i is the position of electron i , $\boldsymbol{\xi}_i(\mathbf{R})$ is the BF displacement of particle i that depends on the configuration of the whole system. The form of backflow displacement in homogenous systems has a form of [40, 41]

$$\boldsymbol{\xi}_i = \sum_{i \neq j} \eta_{ij} \mathbf{r}_{ij}, \quad (1.57)$$

where $\eta_{ij} = \eta(r_{ij})$ is a two-body coordinate transformation and $\mathbf{r}_{ij} = \mathbf{r}_i - \mathbf{r}_j$.

In addition to the systematic finite-size error in the ground-state total energy of a system, the VMC and DMC backflow corrections introduces a slowly decaying source of finite-size error, which would become apparent at large system size if the statistical error bars are sufficiently small. Since the DMC energy is variational with respect to the nodal surface, we expect the BF correction to the total energy is proportional to the RMS displacement of the nodes. For a HEG with the density $\rho(\mathbf{r}) = \rho$, the BF displacement of electron i using Eqs. 1.55 and 1.57 is

$$\Delta \mathbf{r}_i = \sum_{j \neq i} \eta(r_{ij}) \mathbf{r}_{ij}, \quad (1.58)$$

The displaced coordinate $\mathbf{r}_i + \Delta\mathbf{r}_i$ is then used in the evaluation of the Slater part of the trial wave function. Hence

$$\Delta r_i^2 = \sum_{j,k \neq i} \eta(r_{ij})\eta(r_{ik})\mathbf{r}_{ij} \cdot \mathbf{r}_{ik}, \quad (1.59)$$

and the average square electron BF displacement is

$$\Delta r^2 \equiv \frac{1}{N} \sum_i \sum_{j,k \neq i} \eta(r_{ij})\eta(r_{ik})\mathbf{r}_{ij} \cdot \mathbf{r}_{ik}. \quad (1.60)$$

The mean square of the electron BF displacement is

$$\begin{aligned} \langle \Delta r^2 \rangle &= \frac{1}{N} \left\langle \sum_i \sum_{j,k \neq i} \eta(r_{ij})\eta(r_{ik})\mathbf{r}_{ij} \cdot \mathbf{r}_{ik} \right\rangle \\ &\approx \frac{1}{N} \left\langle \sum_i \sum_{j \neq i} \eta^2(r_{ij})r_{ij}^2 \right\rangle, \end{aligned} \quad (1.61)$$

supposing that there is no correlation between the BF displacements of electron i due to electrons j and k , where $j \neq k$. The angled brackets in Eq. 1.61 denote an average over configurations generated in the QMC calculation. Hence

$$\begin{aligned} \langle \Delta r^2 \rangle &\approx \frac{1}{N} \int \int \rho_2(\mathbf{r}, \mathbf{r}') \eta^2(|\mathbf{r} - \mathbf{r}'|) |\mathbf{r} - \mathbf{r}'|^2 d\mathbf{r} d\mathbf{r}' \\ &= \frac{1}{N} \int \int \rho_{xc}(\mathbf{r}, \mathbf{r}') \rho \eta^2(|\mathbf{r} - \mathbf{r}'|) |\mathbf{r} - \mathbf{r}'|^2 d\mathbf{r} d\mathbf{r}' \\ &\quad + \frac{1}{N} \int \int \rho^2 \eta^2(|\mathbf{r} - \mathbf{r}'|) |\mathbf{r} - \mathbf{r}'|^2 d\mathbf{r} d\mathbf{r}' \\ &= \int \bar{\rho}_{xc}(\mathbf{r}) \eta^2(r) r^2 d\mathbf{r} + \rho \int \eta^2(r) r^2 d\mathbf{r}, \end{aligned} \quad (1.62)$$

where $\rho_2(\mathbf{r}, \mathbf{r}') = \left\langle \sum_i \sum_{j \neq i} \delta(\mathbf{r} - \mathbf{r}_i) \delta(\mathbf{r}' - \mathbf{r}_j) \right\rangle$ is the pair density, $\rho_{xc}(\mathbf{r}, \mathbf{r}') = \rho_2(\mathbf{r}, \mathbf{r}') / \rho(\mathbf{r}') - \rho(\mathbf{r})$ is the XC hole and $\bar{\rho}_{xc}(\mathbf{r}) = (1/N) \int \rho_{xc}(\mathbf{r} + \mathbf{r}', \mathbf{r}') \rho(\mathbf{r}') d\mathbf{r}'$ is the system-averaged XC hole.

It can be shown that $\eta(r) \approx cr^{-5/2}$ in 2D HEG [40], where c is a positive constant. Substituting η to Eq. 1.62, the finite-size correction to $\langle \Delta r^2 \rangle$ for long range

interactions by the second term is

$$\rho c^2 \int_L^\infty r^{-5} r^2 2\pi r dr = 2\pi\rho c^2/L = \mathcal{O}(N^{-1/2}). \quad (1.63)$$

Therefore $\langle \Delta r^2 \rangle \approx c_1 + c_2 N^{-1/2}$ with constants c_1 and c_2 . The second term is small at large N , so the RMS BF displacement of each electron is

$$\langle \Delta r^2 \rangle^{1/2} \approx c_1^{1/2} + \frac{c_2}{2c_1^{1/2}} N^{-1/2}. \quad (1.64)$$

In general, unless we are close to the optimal nodal surface, the VMC and DMC energies are expected to be linear in changes to the nodal surface. The BF correction per electron B/N is therefore proportional to the RMS change in the nodal surface per electron, which we assume is the same as the overall RMS BF displacement of electrons. Hence

$$\frac{B}{N} \propto \langle \Delta r^2 \rangle^{1/2} = c_1^{1/2} + \frac{c_2}{2c_1^{1/2}} N^{-1/2}. \quad (1.65)$$

The leading-order finite-size error in the BF correction per electron therefore goes as $\mathcal{O}(N^{-1/2})$. If, on the other hand, the Slater–Jastrow backflow (SJB) nodal surface is (approximately) optimal, then the SJ DMC (SJ-DMC) energy must be quadratic in the error in the SJ nodal surface; so the BF correction per electron would be

$$\frac{B}{N} \propto \langle \Delta r^2 \rangle = c_1 + c_2 N^{-1/2}. \quad (1.66)$$

Again the leading-order finite-size correction in the BF correction per electron is $\mathcal{O}(N^{-1/2})$. Comparing with the finite size error in the exact energy per electron for 2D systems which falls off as $\mathcal{O}(N^{-5/4})$ [42], the finite-size error in SJ energy falls off more slowly as $\mathcal{O}(N^{-1/2})$.

To find the effect of backflow correction on the single-particle finite-size error, we compare twist-averaged (TA) VMC and DMC energies of a 14-electron paramagnetic 2D HEG in a triangular cell of density parameter $r_s = 4$ (Table 1.1). The Jastrow factor and backflow function are optimized at different simulation-cell

Bloch vectors \mathbf{k}_s : Γ [fractional coordinates $(0, 0, 0)$], K is [fractional coordinates $(1/3, -1/3, 0)$], M [fractional coordinates $(1/2, 0, 0)$] and two random Bloch vectors in the simulation-cell BZ. Twist averaging is performed by optimising the wave function at a particular \mathbf{k}_s point in the simulation-cell BZ and then the optimised wave function is used in a set of VMC and DMC calculations with 12000 and 1200 twists, respectively. Our twist-averaging method has the obvious advantage of avoiding multiple expensive and noise-introducing wave-function optimisations; however it has the disadvantage that significant momentum-quantisation effects could still be present in the wave function due to the choice of \mathbf{k}_s for optimising the wave function.

Table 1.1: Twist-averaged (TA) VMC and DMC energies of a 14-electron paramagnetic 2D HEG in a triangular cell of density parameter $r_s = 4$. Random stands for random Bloch vectors in the simulation-cell Brillouin zone.

\mathbf{k}_s for opt.	TA-VMC energy (a.u./e)		TA-DMC energy (a.u./e)	
	SJ	SJB	SJ	SJB
Γ	-0.176397(6)	-0.177778(4)	-0.177538(2)	-0.178195(6)
K	-0.176355(6)	-0.177681(5)	-0.177547(2)	-0.178228(7)
M	-0.176378(6)	-0.177640(5)	-0.177535(2)	-0.178201(6)
Random (1)	-0.176385(6)	-0.177656(5)	-0.177541(2)	-0.178225(8)
Random (2)	-0.176386(6)	-0.177666(5)	-0.177542(2)	-0.178247(8)

In Table 1.2 we compare VMC-BF and DMC-BF corrections. The BF correction $E_{\text{BF}} = E_{\text{SJ}} - E_{\text{SJB}}$, where E_{SJ} and E_{SJB} are the SJ- and SJB-QMC energies, respectively. Our results show that the E_{BF} correction in DMC energy is much smaller than that in the VMC energy however it is considerable and depends on the \mathbf{k}_s points where the SJ wave function is optimised.

Table 1.2: Twist-averaged VMC-BF and DMC-BF corrections of a 14-electron paramagnetic 2D HEG with $r_s = 4$ at different \mathbf{k}_s .

\mathbf{k}_s for opt.	$E_{\text{VMC-BF}}$ (a.u./e)	$E_{\text{DMC-BF}}$ (a.u./e)
Γ	0.001381(7)	0.000657(6)
K	0.001326(8)	0.000681(7)
M	0.001262(8)	0.000666(6)
Random (1)	0.001271(8)	0.000684(8)
Random (2)	0.001280(8)	0.000705(8)

DMC binding energy of bilayer graphene

2.1 Introduction

van der Waals (vdW) interactions play a crucial role in a wide range of physical and biological phenomena, from the binding of rare-gas solids to the folding of proteins. Significant efforts are therefore being made to develop computational methods that predict vdW contributions to energies of adhesion, particularly for materials such as multilayer graphene. This task has proved to be challenging, however, because vdW interactions are caused by nonlocal electron correlation effects. Standard first-principles approaches such as DFT with local exchange–correlation functionals do not describe vdW interactions accurately. One technique for including vdW interactions in a first-principles framework is to add energies obtained using pairwise interatomic potentials to DFT total energies; this is the so-called DFT-D scheme [43–47]. The development of vdW density functionals (vdW-DFs) that can describe vdW interactions in a seamless fashion is another promising approach [48–51]. DFT-based random-phase approximation (RPA) calculations of the correlation energy [52, 53] provide a more sophisticated method for treating

vdW interactions; however, RPA atomisation energies are typically overestimated by up to 15% for solids [54, 55], and hence the accuracy of this approach is unclear. Symmetry-adapted perturbation theory based on DFT allows one to calculate the vdW interactions between molecules and hence, by extrapolation, between nanostructures [56]. Finally, empirical interatomic potentials with r^{-6} tails may be used to calculate binding energies [57, 58], although such potentials give a qualitatively incorrect description of the interaction of metallic or π -bonded two-dimensional (2D) materials at large separation [59].

A key test system for methods purporting to describe vdW interactions between low-dimensional materials is bilayer graphene (BLG). Despite a great deal of theoretical and experimental work, the binding energy (BE) of graphene layers remains poorly understood. The cleavage energy of graphite has been measured to be 43(5) meV/atom [57], the BE to be 35(10) meV/atom [60], and the exfoliation energy to be 52(5) meV/atom [61]. More recent experimental work has found the cleavage energy to be 31(2) meV/atom [62]. It has been suggested that the latter result may be substantially underestimated, because the experimental data were analysed using a Lennard-Jones potential, which gives qualitatively incorrect interlayer BEs at large separation [63]. Similar difficulties of interpretation may affect the other experimental results in the literature. The results obtained in these works are widely scattered. The DMC method has previously been applied to calculate the BEs of AB- and AA-stacked graphite [64, 65], which were found to be 56(5) and 36(1) meV/atom, respectively, although these calculations were performed in relatively small simulation supercells, and finite-size effects may limit the accuracy of the results obtained. Several theoretical studies have used methods based on DFT to calculate the BE of BLG [50, 66–70], but there is very little consensus.

In this chapter we provide DMC data for the BE of BLG and the atomisation energy of monolayer graphene (MLG), which we have extrapolated to the thermo-

dynamic limit. The DMC method is the most accurate first-principles technique available for studying condensed matter. Our data can therefore be used as a benchmark for the development of vdW functionals.

2.2 Computational details

We have used the VMC and DMC methods as implemented in the CASINO code [21] to study MLG and BLG. In the former method, Monte Carlo integration is used to evaluate expectation values with respect to trial many-body wave-function forms that may be of arbitrary complexity. In the DMC method [22, 71], a stochastic process governed by the Schrödinger equation in imaginary time is simulated to project out the ground-state component of the trial wave function. Fermionic antisymmetry is maintained by the fixed-node approximation, in which the nodal surface is constrained to equal that of the trial wave function [35]. DMC methods have recently been used to study the BE of hexagonal boron nitride bilayers [72].

Our many-body trial wave-function form consisted of Slater determinants for spin-up and spin-down electrons multiplied by a symmetric, positive Jastrow correlation factor $\exp(J)$ as defined in Eq. 1.29. The Slater determinants contained Kohn-Sham orbitals that were generated using the CASTEP plane-wave DFT code [3] within the LDA. We performed test DMC calculations for 3×3 supercells of MLG and AB-stacked BLG using PBE [14] orbitals. The effect of changing the orbitals on the DMC total energies (and hence the BE) was statistically insignificant.

We used Dirac–Fock pseudopotentials to represent the C atoms [4, 73] and fixed the in-plane lattice parameter at the experimental value of $a = 2.460 \text{ \AA}$. For BLG, we restrict our attention to the nonretarded regime ¹, in which the BE is simply

¹At separations larger than few nanometers, the use of the static Coulomb interaction between electrons in two graphene layers ceases to be valid due to the finite speed of light, resulting in a crossover to a regime in which the attractive forces arise from photon zero-point energy [74] (Appendix A).

the difference between the nonrelativistic total energy per atom in the monolayer and the bilayer. We used vdW-DF layer separations of $d = 3.495 \text{ \AA}$ and 3.384 \AA [75] for the AA- and AB-stacked configurations, respectively.

To improve the scaling of our DMC calculations and to allow the use of 2D-periodic boundary conditions, the orbitals were re-represented in a B-spline (blip) basis [20]. The Jastrow exponent J consisted of polynomial and plane-wave expansions in the electron–ion and electron–electron distances [76]. The free parameters in the Jastrow factor were optimised by unreweighted variance minimisation [26, 27] and the DMC energy was extrapolated linearly to zero time step. The fixed-node error is of uncertain magnitude, but it is always positive, and should largely cancel when the BE is calculated.

2.2.1 Finite-population errors in our DMC data

We have carried out calculations to investigate finite-population errors [77] in our DMC calculations. Figures 2.1(a) and 2.1(b) show the non-twist-averaged DMC ground-state energy per atom for a 3×3 supercell of monolayer graphene and the DMC energy of an isolated, spin-polarised C atom against the reciprocal of the target configuration population. The DMC energies have been extrapolated linearly to zero time step in each case. The function fitted to the DMC data in Fig. 2.1 is $E(N_{\text{pop}}) = E(\infty) + B/N_{\text{pop}}$, where N_{pop} is the target configuration population [77]. For our Slater–Jastrow trial wave function, we find that $B = 1.4(6) \text{ eV}$ for monolayer graphene in a 3×3 supercell. The gradient B is of marginal significance. For populations in excess of 512 configurations the expected bias in the DMC energy is less than $2.7(12) \text{ meV/atom}$. We used target populations of 1024 configurations in our production calculations for supercells of 3×3 primitive cells and target populations of 512 configurations for larger supercells. Population-control biases are always positive and must largely cancel out of the BE of BLG.

For an isolated C atom, the value of B is not statistically significant. We have used a target population of 1024 configurations in our calculation for the C atom; the resulting population-control bias in the DMC energy is less than 1 meV.

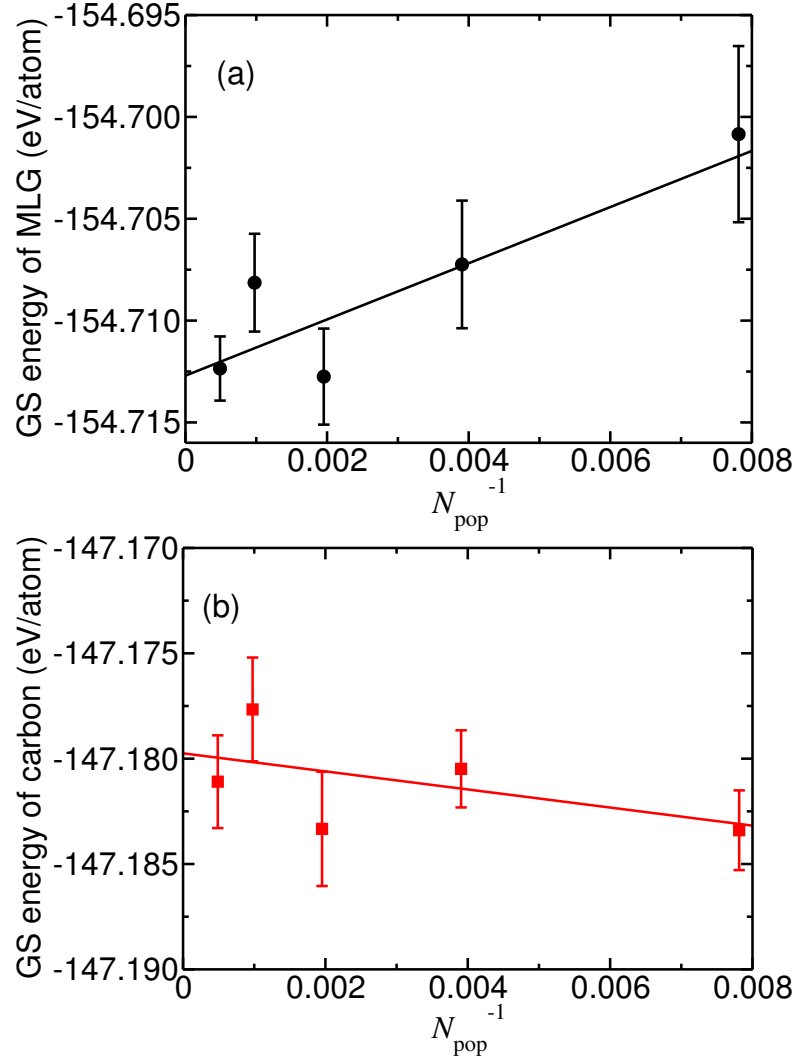


Figure 2.1: (a) Non-twist-averaged DMC ground-state (GS) energy of a 3×3 cell of monolayer graphene and (b) DMC GS energy of a C atom as a function of the reciprocal of the configuration population N_{pop}^{-1} .

2.2.2 Finite-size errors in our DMC data

The principal source of uncertainty in our BE results is the need to use finite simulation cells subject to periodic boundary conditions in DMC calculations for

condensed matter. Finite-size errors in DMC total energies consist of (i) pseudo-random, oscillatory single-particle finite-size errors due to momentum quantisation and (ii) systematic finite-size errors due to the inability to describe long-range two-body correlations and the difference between $1/r$ and the 2D Ewald interaction [78, 79] in a finite periodic cell. By dividing the electron–electron interaction energy into a Hartree term (the electrostatic energy of the charge density) and an exchange–correlation energy (the interaction energy of each electron with its accompanying exchange–correlation hole) and considering the long-range nonoscillatory behaviour of the hole predicted by the RPA, it can be shown that the systematic finite-size error in the interaction energy per electron of a 2D-periodic system is negative and scales asymptotically with system size N as $O(N^{-5/4})$ [42]. The leading-order long-range finite-size error in the kinetic energy per electron behaves in a similar fashion. The finite-size error in the atomisation energy is therefore positive and scales as $O(N^{-5/4})$, and the finite-size error in the BE per atom must also exhibit the $O(N^{-5/4})$ scaling. We also investigated finite-size errors in the asymptotic BE using the Lifshitz theory of vdW interactions [80, 81] with a Dirac model of electron dispersion in graphene. To study finite system sizes, we introduced a cutoff wavelength that depended on the cell size and layer separation. However, near the equilibrium separation, short-range interactions are important and the contribution to the finite-size error from the Lifshitz theory is negligible (Appendix A). In order to eliminate finite-size effects and obtain the atomisation and BEs in the thermodynamic limit, we studied simulation cells consisting of arrays of 3×3 , 4×4 , and 6×6 primitive cells for MLG and BLG at the equilibrium layer separation and 3×3 and 5×5 cells for BLG at nonequilibrium layer separations. We used canonical-ensemble twist averaging [82] (i.e., averaging over offsets to the grid of \mathbf{k} vectors) to reduce the oscillatory single-particle finite-size errors in the ground-state energies of MLG and BLG. To obtain the twist-averaged energy of MLG in a simulation cell containing N_P primitive cells, we performed DMC

calculations at twelve random offsets \mathbf{k}_s to the grid of \mathbf{k} vectors, then fitted

$$E(N_P, \mathbf{k}_s) = \bar{E}(N_P) + b[E_{\text{LDA}}(N_P, \mathbf{k}_s) - E_{\text{LDA}}(\infty)] \quad (2.1)$$

to the DMC energies per atom $E(N_P, \mathbf{k}_s)$. The model function has two fitting parameters: $\bar{E}(N_P)$, which is the twist-averaged DMC energy per atom, and b . $E_{\text{LDA}}(N_P, \mathbf{k}_s)$ is the DFT-LDA energy per atom of MLG obtained using the offset \mathbf{k} -point grid corresponding to the supercell used in the DMC calculations, and $E_{\text{LDA}}(\infty)$ is the DFT-LDA energy per atom obtained using a fine (50×50) \mathbf{k} -point mesh. Finally, we extrapolated our total-energy data to infinite system size by fitting

$$\bar{E}(N_P) = E(\infty) + cN_P^{-5/4} \quad (2.2)$$

to the twist-averaged energies per atom, where the extrapolated energy per atom $E(\infty)$ and c are fitting parameters. The atomisation energy of MLG is the difference between the energy of an isolated, spin-polarised C atom and the energy per atom of MLG.

2.3 Results and discussion

2.3.1 Atomisation energy of monolayer graphene

Our DMC atomisation energies of MLG as a function of system size are plotted in Fig. 2.2. We find the static-nucleus DMC atomisation energy to be 7.395(3) eV/atom with a Slater–Jastrow trial wave function. This is lower than the DMC result of 7.464(10) eV/atom reported in Ref. [83]. Most of this disagreement arises from the use of different pseudopotentials in the two works. Table 2.1 compares the atomisation energies of MLG predicted by DFT with different functionals and by DMC. Our DFT static-nucleus atomisation energies were obtained using the

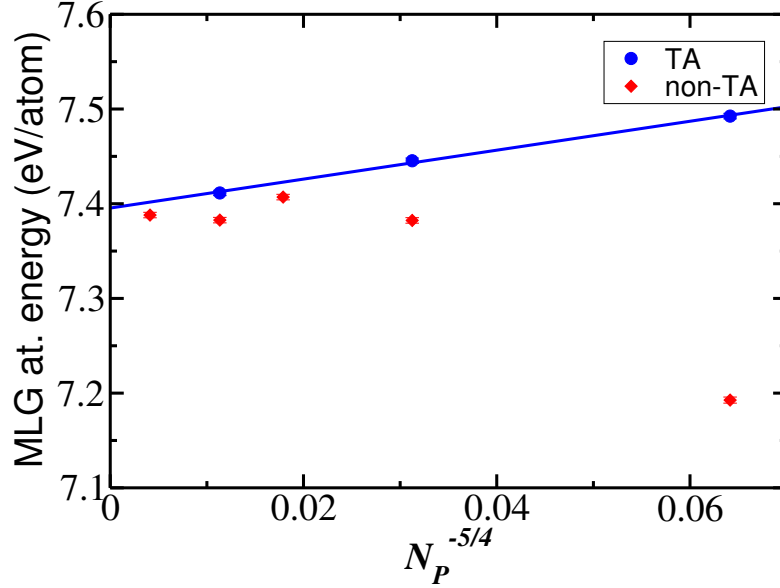


Figure 2.2: Twist-averaged (TA) and non-TA atomisation energies of MLG against $N_P^{-5/4}$ as calculated by DMC, where N_P is the number of primitive cells in the simulation supercell.

Table 2.1: Static-nucleus atomisation energy E_{atom} of monolayer graphene obtained in various DFT and DMC studies. The bond lengths quoted in the table are the ones used in the calculations, not necessarily the optimised bond length for the given method.

Method	Pseudopotential	Bond length (\AA)	E_{atom} (eV/atom)
DFT-LDA [84]		1.412	8.96
DFT-LDA [85]		1.420	8.873
DFT-LDA (pres. wk.)	Ultrasoft [3]	1.420	8.632
DFT-LDA (pres. wk.)	Dirac-Fock [4]	1.420	8.578
DFT-PBE [86]	Norm-conserving [87]	1.440	7.847
DFT-PBE [84]		1.424	7.93
DFT-PBE [83]	Dirac-Fock [88]	1.421	7.906
DFT-PBE (pres. wk.)	Ultrasoft [3]	1.420	7.873
DFT-PBE (pres. wk.)	Dirac-Fock [4]	1.420	7.837
DMC [83]	Dirac-Fock [88]	1.421	7.464(10)
DMC (pres. wk.)	Dirac-Fock [4]	1.420	7.395(3)

LDA and PBE functionals with both ultrasoft [3] and Dirac-Fock pseudopotentials [4] using a plane-wave cutoff energy of 220 Ry. Our DMC calculations used the pseudopotential locality approximation [89]. We compare our results with previous results in the literature [85, 86]. Both DFT-PBE and DFT-LDA calculations overestimate the atomisation energy, but the error in the LDA result is significantly

larger.

The DFT results in Table 2.1 show that using different pseudopotentials changes the calculated atomisation energy of graphene by 40–70 meV/atom, which is very large on the scale of the BE of graphite. However, DFT-LDA and DFT-D calculations at different layer separations show that both ultrasoft and Dirac–Fock pseudopotentials give the same value for the BE of AB-stacked BLG: see Table 2.2. The cancellation of pseudopotential errors between bilayer and monolayer graphene is much larger than between monolayer graphene and an isolated C atom, so our calculation of the BE of BLG is expected to be significantly more accurate than our calculation of the atomisation energy of graphene. It should be noted that pseudopotential errors are at least as bad in DMC calculations as in DFT; although DMC is a highly accurate method, it cannot do better than permitted by the pseudopotentials used to model atoms. Part of the uncertainties are due to the locality approximation and primarily caused by using the pseudopotentials.

Table 2.2: Comparison of DFT and DFT-D BEs of AB-stacked BLG at equilibrium separation 3.384 Å using ultrasoft and Dirac–Fock pseudopotentials.

Method	Pseudopotential	BE (meV/atom)
DFT-PBE	Dirac–Fock [4]	6.03
DFT-PBE	Ultrasoft [3]	4.87
DFT-LDA	Dirac–Fock [4]	12.39
DFT-LDA	Ultrasoft [3]	13.53
DFT-D (TS) [47]	Dirac–Fock [4]	38.35
DFT-D (TS) [47]	Ultrasoft [3]	38.22
DFT-D (OBS) [90]	Dirac–Fock [4]	59.32
DFT-D (OBS) [90]	Ultrasoft [3]	59.58
DFT-D (Grimme) [44]	Dirac–Fock [4]	27.01
DFT-D (Grimme) [44]	Ultrasoft [3]	26.57

The DFT-PBE phonon zero-point energy (ZPE) of MLG was calculated using the method of finite displacements in a 6×6 supercell [91] and found to be 0.165 eV/atom. The ZPE is a correction to be subtracted from the static-nucleus atomisation energy. In principle, an accurate first-principles atomisation energy for

graphene could be used to estimate the BE of graphite by taking the difference of the experimental atomisation energy of graphite [7.371(5) eV/atom [92]] and the ZPE-corrected atomisation energy of MLG. However, the spread of DFT atomisation energies resulting from different choices of pseudopotential (of order 40–70 meV/atom) implies that first-principles pseudopotential calculations cannot currently be used to calculate the BE of graphite by this approach.

2.3.2 Binding energy of bilayer graphene

In Fig. 2.3 we plot the twist-averaged BEs of AA- and AB-stacked BLG as a function of system size. Non-twist-averaged BEs are shown in the inset to Fig. 2.3 and, as expected, show large oscillations due to momentum-quantisation effects. For widely separated graphene layers with nonoverlapping charge densities, single-

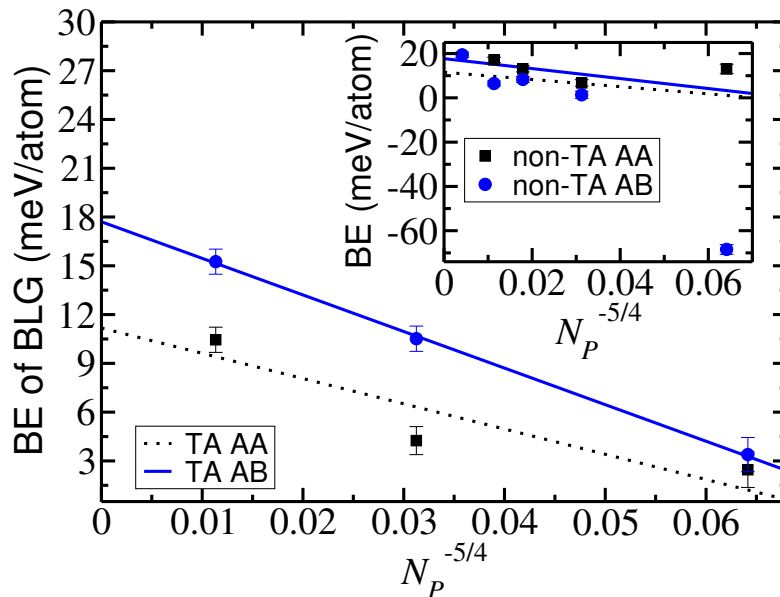


Figure 2.3: Twist-averaged (TA) BLG BE against $N_P^{-5/4}$ as calculated by DMC, where N_P is the number of primitive cells in the simulation supercell. The inset shows non-twist-averaged BEs. The layer separations are the vdW-DF [75] equilibrium values of 3.495 and 3.384 Å for the AA- and AB-stacked structures, respectively.

particle finite-size errors cancel perfectly when the BE is calculated. However,

when the layers are closer together, the cancellation is no longer perfect. In practice, near the equilibrium separation, the single-particle errors in the BE correlate closely with the single-particle errors in the total energy of BLG. To evaluate the BE in the thermodynamic limit, we twist-averaged the BE using Eq. (2.1) with the BE per atom in place of $E(N_P, \mathbf{k}_s)$ and the DFT-LDA total energy per atom of BLG in place of $E_{\text{LDA}}(N_P, \mathbf{k}_s)$. We then extrapolated the twist-averaged BE to infinite system size using Eq. (2.2). As shown in Fig. 2.3, the BE of AB-stacked BLG is larger than that of AA-stacked BLG, confirming that the former is the more stable structure.

The area of a simulation cell with N_P unit cells is $A = \sqrt{3}N_P a^2/2$, where a is the lattice parameter of graphene. If we define the linear size L of the cell via $\pi L^2 = A$ then we may express the twist-averaged BE per atom as $\bar{E}_{\text{bind}}(L) = E_{\text{bind}}(\infty) + c' L^{-5/2}$, where c' is $-0.31(5)$ and $-0.43(5)$ eV $\text{\AA}^{5/2}$ for the AA-stacked and AB-stacked geometries, respectively. The BE is reduced at small supercell sizes L . The use of a finite supercell crudely models the situation where the Coulomb interaction between electrons is screened by a metallic substrate. Hence a metallic substrate is expected to weaken the binding of BLG.

In Fig. 2.4 we plot the BE of AB-stacked BLG against the interlayer separation, as calculated by DFT, DFT-D, and DMC. The layer separations we have studied are not in the asymptotic regime in which the BE falls off as d^{-3} , where d is the interlayer separation [93]. We have fitted the function

$$E_{\text{bind}}(d) = A_4 d^{-4} + A_8 d^{-8} + A_{12} d^{-12} + A_{16} d^{-16} \quad (2.3)$$

to our DMC BE data, where the $\{A_i\}$ are fitting parameters, which we find to be $A_4 = -2.9 \times 10^3$ meV \AA^4 , $A_8 = -2.97 \times 10^5$ meV \AA^8 , $A_{12} = 6.18 \times 10^7$ meV \AA^{12} , and $A_{16} = -1.63 \times 10^9$ meV \AA^{16} . This function fits the DMC data well, with a χ^2 value of 0.007 per data point. The BE found at the minimum of the fitting curve is 17.8(8) meV/atom at the equilibrium separation of 3.43(4) \AA . Although the

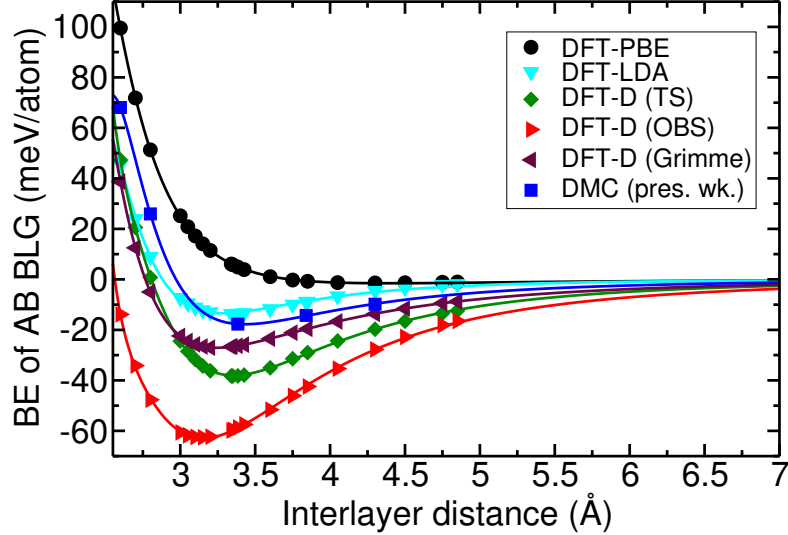


Figure 2.4: BE curve of AB-stacked BLG as a function of interlayer distance calculated using DFT, DFT-D, and DMC methods. Our DFT-D calculations used the Tkatchenko–Scheffler (TS) [47], Ortmann–Bechstedt–Schmidt (OBS) [90], and Grimme [44] vdW corrections.

Table 2.3: BE of BLG (both AA- and AB-stacked) obtained in recent theoretical studies. The layer separations d quoted in the table are the ones used in the calculations, not necessarily the optimised bond length for the given method. “SAPT(DFT)” and “DFT-LCAO-OO” denote symmetry-adapted perturbation theory based on DFT and linear combination of atomic orbitals-orbital occupancy based on DFT, respectively. “MBD” denotes many-body dispersion calculations.

Stacking	Method	d (Å)	BE (meV/atom)
AA	vdW-DF [66]	3.35	10.4
AA	DFT-D [66]	3.25	31.1
AA	DMC (pres. wk.)	3.495	11.5(9)
AB	DFT-LCAO-OO [67]	3.1–3.2	70(5)
AB	SAPT(DFT) [68]	3.43	42.5
AB	vdW-DF [50]	3.6	45.5
AB	vdW-DF [66]	3.35	29.3
AB	DFT-D [66]	3.25	50.6
AB	DFT-D [69]	3.32	22
AB	MBD [70]	3.37	23
AB	DMC (pres. wk.)	3.384	17.7(9)

separation that minimises our fitted BE curve for AB-stacked BLG is somewhat larger than the separation used in our calculation of the BE reported in Table 2.3, the difference between the BEs is not statistically significant. The Tkatchenko–

Scheffler [47] DFT-D scheme shows roughly the same equilibrium separation as DMC, but the magnitude of the BE is substantially larger. In general, the three DFT-D methods studied [44, 47, 90] disagree with each other and with DMC. Indeed, the magnitude of the BE (if not the shape of the BE curve) is best described by the LDA. Table 2.3 clearly shows that the DMC BE of BLG is somewhat less than the BEs predicted by DFT-D, although the latter vary significantly from scheme to scheme.

Our fitted BE curve enables us to calculate the out-of plane zone-centre optical phonon frequency $\omega_{ZO'}$ of AB-stacked BLG. The interlayer BE per atom of BLG can be written as $E_{\text{bind}}(d) = E_0 + \frac{1}{8}m_C\omega_{ZO'}^2(d - d_0)^2 + O(d - d_0)^3$, where E_0 is the BE per atom at the equilibrium separation d_0 , m_C is the mass of a carbon atom, and $\omega_{ZO'}$ is the out-of-plane phonon frequency. A comparison of $\omega_{ZO'}$ frequencies obtained by DFT, DMC, and experiment [94] is shown in Table 2.4. Our DFT-LDA frequency is in reasonable agreement with the result (76.8 cm^{-1}) reported in Ref. [95]. The difference between the $\omega_{ZO'}$ frequency predicted by our fit to our DMC data and the experimental result is negligible [$3(7) \text{ cm}^{-1}$].

Table 2.4: The equilibrium separation d_0 , static-lattice BE at equilibrium separation, and out-of-plane zone-centre optical-phonon frequency $\omega_{ZO'}$ of AB-stacked BLG obtained by DFT, DFT-D, DMC, and experiment. The minimum of the curve fitted to the DMC BE data, which is reported in this table, is in statistical agreement with the DMC BE obtained using a fixed layer separation of 3.384 \AA , which is reported in Table 2.3.

Method	d_0 (\AA)	BE (meV/at.)	$\omega_{ZO'}$ (cm^{-1})
DFT-PBE	4.40	1.53	16
DFT-LDA	3.28	13.38	84
DFT-D (TS)	3.35	38.03	111
DFT-D (OBS)	3.15	62.70	133
DFT-D (Grimme)	3.25	27.08	95
DMC (pres. wk.)	3.43(4)	17.8(8)	83(7)
Exp. [94]			80(2)
Exp. [96]			89.7(15)

2.3.3 Choice of fitting function for the binding-energy curve

We have investigated different fitting functions for our DMC BE data for AB-stacked BLG. In Fig. 2.5 we compare the following fits to the DMC BE:

Fit 1a The maroon long-dashed line shows a fit of

$$E_{\text{bind}}(d) = a + b(d - d_0)^2 + c(d - d_0)^3 \quad (2.4)$$

to the DMC BE data at interlayer separations $d = 2.8, 3.384, \text{ and } 3.84 \text{ \AA}$, where $a, b, \text{ and } c$ are fitting parameters and $d_0 = 3.384 \text{ \AA}$ is fixed at the vdW-DF interlayer equilibrium separation [75].

Fit 1b The red short-dashed line shows a fit of Eq. (2.4) to the DMC BE data at interlayer separations $d = 2.6, 2.8, 3.384, \text{ and } 3.84 \text{ \AA}$. This time $a, b, c, \text{ and } d_0$ are all fitting parameters.

Fit 1c The green dot-dashed line shows a fit of Eq. (2.4) to the DMC BE data at interlayer separations $d = 2.8, 3.384, 3.84, \text{ and } 4.3 \text{ \AA}$. Again, $a, b, c, \text{ and } d_0$ are all fitting parameters.

Fit 1d The blue dash-double dotted line shows a fit of Eq. (2.4) to all our DMC BE data. Again, $a, b, c, \text{ and } d_0$ are all fitting parameters.

Fit 2 The solid black line shows a fit of

$$E_{\text{bind}}(d) = \alpha \exp(-\beta d) + \gamma d^{-4} \quad (2.5)$$

to all our DMC BE data, where $\alpha, \beta, \text{ and } \gamma$ are fitting parameters [64].

Fit 3 The solid magenta line shows a fit of

$$E_{\text{bind}}(d) = A_4 d^{-4} + A_8 d^{-8} + A_{12} d^{-12} + A_{16} d^{-16} \quad (2.6)$$

to all our DMC BE data, where the $\{A_i\}$ are fitting parameters.

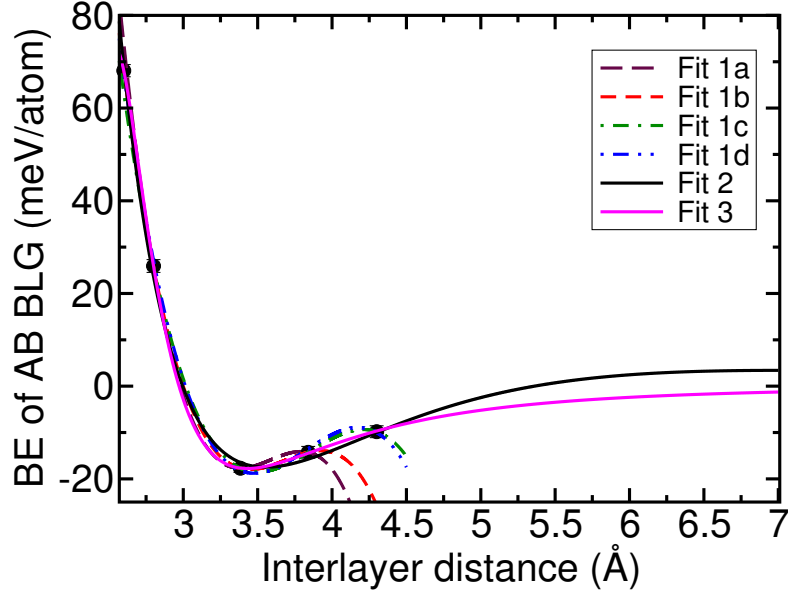


Figure 2.5: DMC BE of AB-stacked BLG against interlayer separation using different fitting curves.

Equation (2.6) has the correct d^{-4} form of decay for the BE at intermediate range and has a reasonable model of the hard-core repulsion. The χ^2 values obtained with Fits 2 and 3 are 1.3 and 0.007 per data point, respectively, compared with 0.4 per data point for Fit 1d, which has the same number of fitting parameters as Fit 3. The χ^2 value per data point for Fits 1a–1c is zero, because the number of data points is equal to the number of parameters. Fit 2 shows unphysical behaviour: the exponential term prefers to be attractive while the d^{-4} tries to be repulsive. We have therefore used Fit 3 to obtain the breathing-mode frequency presented in the Table 2.4.

In Table 2.5 we compare the equilibrium separation d_0 , the corresponding BE $E_{\text{bind}}(d_0)$, the curvature $E''_{\text{bind}}(d_0)$, and the out-of-plane optical phonon frequency (the breathing mode ZO') obtained with the different fits to our DMC BE data.

To evaluate error bars on quantities such as the second derivative of the BE at the minimum and the corresponding phonon frequency, we used bootstrap Monte

Table 2.5: Equilibrium separation d_0 and corresponding BE $E_{\text{bind}}(d_0)$, second derivative of the BE at the minimum $E''_{\text{bind}}(d_0)$, and out-of-plane phonon frequency $\omega_{\text{ZO}'}$ that are obtained by fitting different curves to our DMC data for the BE of BLG. Experimental results [94] are shown for comparison.

Fit	d_0 (Å)	$E_{\text{bind}}(d_0)$ (meV/atom)	$E''_{\text{bind}}(d_0)$ (meV Å ⁻² /atom)	$\omega_{\text{ZO}'}$ (cm ⁻¹)
Fit 1a	3.384	-17.7(9)	131(11)	109(4)
Fit 1b	3.45(4)	-18(1)	110(17)	100(8)
Fit 1c	3.50(4)	-18.6(8)	109(12)	99(7)
Fit 1d	3.48(3)	-18.8(8)	122(9)	105(4)
Fit 2	3.55(2)	-17.5(7)	58(5)	72(3)
Fit 3	3.43(4)	-17.8(8)	76(13)	83(7)
Exp. [94]			70(4)	80(2)
Exp. [96]			89(3)	89.7(15)

Carlo sampling of our data together with repeated χ^2 fits. In Fig. 2.6, histograms of $E''_{\text{bind}}(d_0)$ for Fits 1d, 2 and 3 are shown. The phonon frequencies obtained using Fits 2 and 3 are in good agreement, although the difference between Fits 1d and 3 is more significant. However, we believe Fit 3 to be more reliable because it is constructed to have the correct asymptotic behaviour.

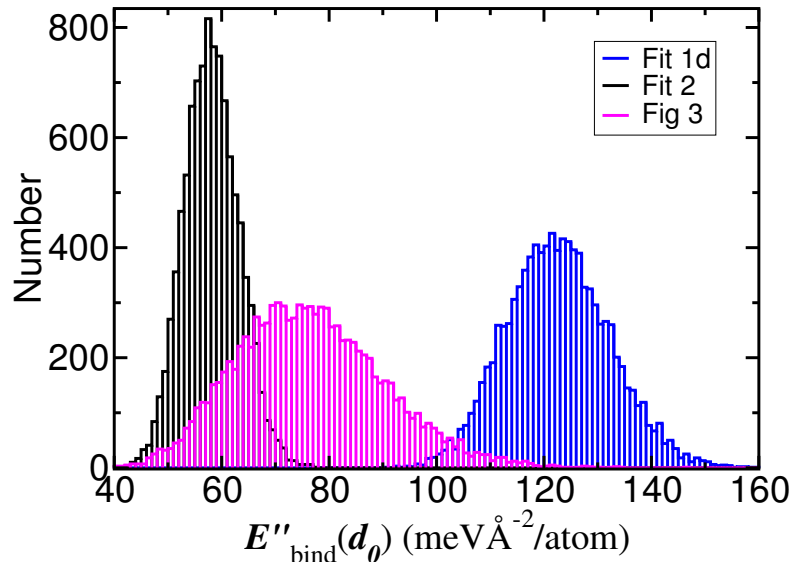


Figure 2.6: Histogram of $E''_{\text{bind}}(d_0)$ obtained in bootstrap Monte Carlo sampling of Fits 1d, 2, and 3 with 10,000 samples.

2.4 Conclusion

In summary, we have used the DMC method to determine the BE of BLG. Our approach includes a full, first-principles treatment of vdW interactions. We have found the static-nucleus atomisation energy of MLG to be 7.395(3) eV/atom, although the uncertainty in this result due to the use of nonlocal pseudopotentials may be as much as 70 meV/atom. We find the BEs of AA- and AB-stacked BLG near their equilibrium separations to be 11.5(9) and 17.7(9) meV/atom, respectively. Our results indicate that current DFT-D and vdW-DF methods significantly overbind 2D materials.

DMC binding energies of G/hBN moiré heterostructures

3.1 Introduction

Van der Waals (vdW) layered heterostructures are materials formed from a stacked sequence of various 2D crystals bonded with weak interlayer vdW-like forces [97]. The first step towards fabricating such heterostructures was made by mechanically transferring monolayer graphene onto a single-crystal hexagonal boron nitride (hBN) substrate [98]. hBN has the same crystal structure as graphene, is an insulator with an atomically flat surface and is free of dangling bonds [98]; hence it plays the role of a perfect substrate to preserve graphene's electronic properties. Double-layer devices based on graphene-on-hBN (G/hBN) have a self-cleaning interface [99] due to the weak vdW interlayer interactions and are of great interest owing to their electronic [98, 100, 101] and optical [102] applications. They are also ideal for plasmon lenses, tunable sensors and light absorbers because of their low plasmon damping [103]. The other properties of such heterostructures is the ability to tune their electronic and optical properties, specially by appropriate combining G/hBN with other 2D monolayers [102].

The peculiar optical and electronic properties of G/hBN distinct from its components arises from moiré patterns [104–106]. The moiré superlattice of G/hBN has a long quasi-periodic hexagonal form due to the small mismatch $\delta = a_{\text{BN}}/a_{\text{G}} - 1$, less than 2%, between the lattice constant of hBN a_{BN} and the lattice constant of graphene a_{G} . Because of the out of plane extension of electron orbitals, which affect the charge carriers in the adjacent 2D layer [107], G/hBN also exhibits Hofstadter’s butterfly or fractal spectrum of magnetic bands when placed in a magnetic field whose magnetic length is comparable to the periodicity of the moiré superlattice [108, 109].

Despite various experimental and theoretical works on the electronic properties of G/hBN, few attempts have been made to investigate the interlayer vdW-like interactions via studying its binding and vibrational properties. The available first-principles studies have compared the interlayer binding energy (BE) of bilayer G/hBN for different stacking configurations within the DFT-LDA, DFT-vdW and DFT-RPA methods [105, 110]. Nevertheless, we have shown in Chap. 2 that DFT gives qualitatively wrong BE values for bilayer graphene due to the lack of description of vdW interactions. Here we study the BE and vibrational properties of bilayer G/hBN using the variational quantum Monte Carlo (VMC) and diffusion quantum Monte Carlo (DMC) methods.

3.2 Computational details

Due to the moiré patterns in a bilayer G/hBN, different kinds of stacking configurations are present, which affect the interlayer vdW interactions. By comparing the DFT total energies of different possible stacking patterns, we have selected four configurations with statistically different DFT energies. The stacking patterns of G/hBN in this work are constructed by translating hBN on top of graphene along the path O–P as shown in Fig. 3.1(a)–(d):

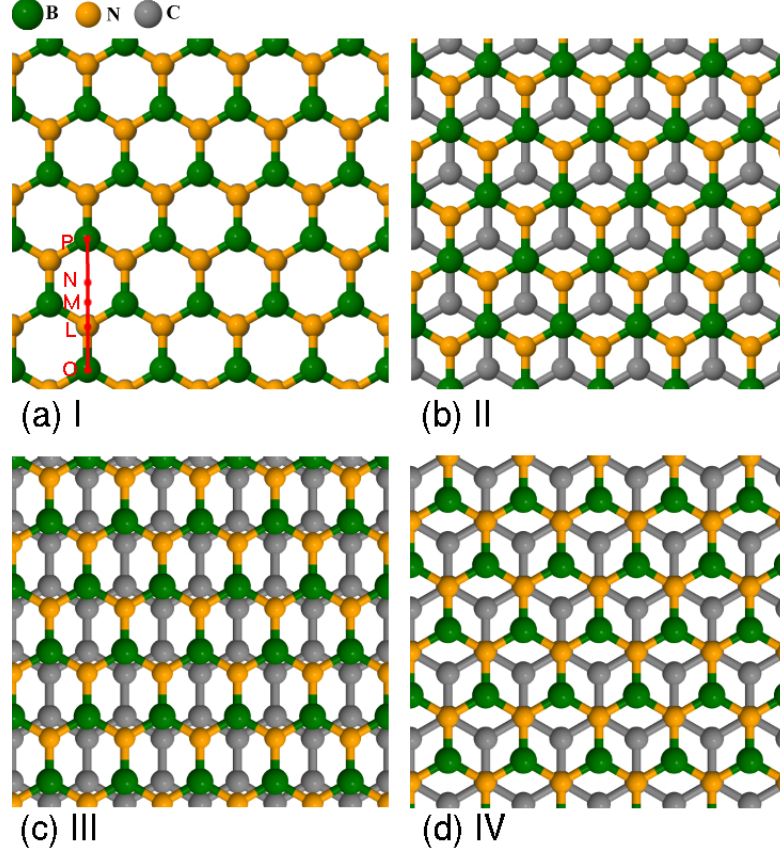


Figure 3.1: Four different stacking configurations of bilayer G/hBN, where B, N and C atoms are shown by green, orange and grey colours, respectively. Monolayer hBN is translating on top of monolayer graphene along the path O–P shown in the stacking pattern (a). Translating hBN in pattern I by $3 a_{C-C}$ from O to P reconstructs AA-stacked form of G/hBN.

- I** Starting from AA-stacking, where boron (green spheres) and nitrogen (orange spheres) atoms are exactly on top of carbon atoms (grey spheres).
- II** Translating hBN from the AA-stacked structure by a C–C bond length a_{C-C} along the path O–L to create a Bernal stacked structure (AB), where all boron atoms are on top of carbon atoms and nitrogen atoms are centred above graphene hexagons.
- III** Translating hBN in AA-stacked by $3/2 a_{C-C}$ along the path O–M.
- IV** Translating hBN in AA-stacked by $2 a_{C-C}$ along the path O–N to form another kind of AB-stacked similar to the pattern II but with the nitrogen and boron atoms swapped.

We calculate the BE per atom E_{BE} of bilayer G/hBN by

$$E_{\text{BE}} = E_{\text{BNG}} - \frac{1}{2}(E_{\text{BN}} + E_{\text{G}}), \quad (3.1)$$

where E_{BNG} , E_{BN} and E_{G} are the total energies per atom of bilayer G/hBN, monolayer hBN and monolayer graphene, respectively. The total energies were calculated using the VMC and DMC methods as implemented in the CASINO code [21]. Our many-body trial wave function contained the antisymmetric Slater determinant for both spin-up and spin-down electrons multiplied by a symmetric Jastrow factor [22]. The Slater determinants consisted of Kohn-Sham orbitals, that were generated using the CASTEP plane-wave DFT code [3].

We choose ultrasoft pseudopotentials [2, 3] and a plane-wave energy cutoff of 50 Ry within the Grimme-PBE functional [44] to let the graphene and hBN layers be buckled while pinning the mean value of layer separation and fixing the height of simulation cells at 16 Å. We also fix the in-plane lattice parameters of both graphene and hBN at the experimental lattice parameter of graphene, $a = 2.460$ Å, since the strain contribution due to the 2% lattice mismatch largely cancels out when the difference in the total energies of monolayers and the bilayer is taken; however, to model the bilayer heterostructure system, the effect of strain should be included.

We generated Kohn-Sham orbitals using a plane-wave energy cutoff of 220 Ry and Dirac–Fock pseudopotentials [4, 73] within the LDA although the effect of changing the functional used to generate the orbitals on the DMC total energies and the BE is statistically insignificant (Sec. 2.2).

To remove the biases due to the finite time steps and populations of walkers, we perform DMC calculations using time steps in the ratio 1:2.5 with the corresponding target configuration populations being in the ratio 2.5:1, and we linearly extrapolated the DMC energies to zero time step and infinite population. The

fixed-node error is of uncertain magnitude, but it is always positive, and should largely cancel when the BE is calculated. To reduce the single-particle finite-size errors caused by momentum quantization and the systematic finite-size errors, we have evaluated the twist-averaged DMC ground-state energies per atom of simulation cells containing 3×3 and 5×5 unit cells for graphene, hBN and G/hBN, then extrapolated them to the thermodynamic limit as described in Sec. 2.2.2.

DFT phonon dispersion curves were calculated using ultrasoft pseudopotentials and a plane-wave cutoff of 50 Ry within LDA functional, which unlike PBE functional shows the weak binding between bilayer vdW structures as discussed in chapter 2. We used a $5 \times 5 \times 1$ supercell with a Brillouin size sampling \mathbf{k} -point mesh of $35 \times 35 \times 1$, and displaced the atoms by $\pm 0.04 \text{ \AA}$ within the finite-displacement method. To improve the accuracy, the initial equilibrium atomic positions were relaxed until the forces were less than $5 \times 10^{-5} \text{ eV\AA}^{-1}$.

3.3 Results and discussion

3.3.1 Time-step errors in our DMC calculations

In order to test the behaviour of DMC energies at different finite time steps, we calculated the non-twist-averaged ground-state DMC energy of monolayer graphene and hBN as well as the BE of G/hBN (stacking form II) for a supercell composed of 3×3 primitive cells. Comparing Figs. 3.2(a)–(c) shows that the time-step errors in the total energies at time step 0.04 are typically around 30 meV/atom, while the error in the BE largely cancels out by taking the difference in the total energies. The DMC total energy of each hexagonal monolayer also behaves linearly up to a small time step of 0.04 a.u. however, the nonlinear part of time step is largely eliminated in the BE resulting in linear behaviour up to a much larger time step of 0.2 a.u. The extrapolated BE using all DMC points at different time steps in

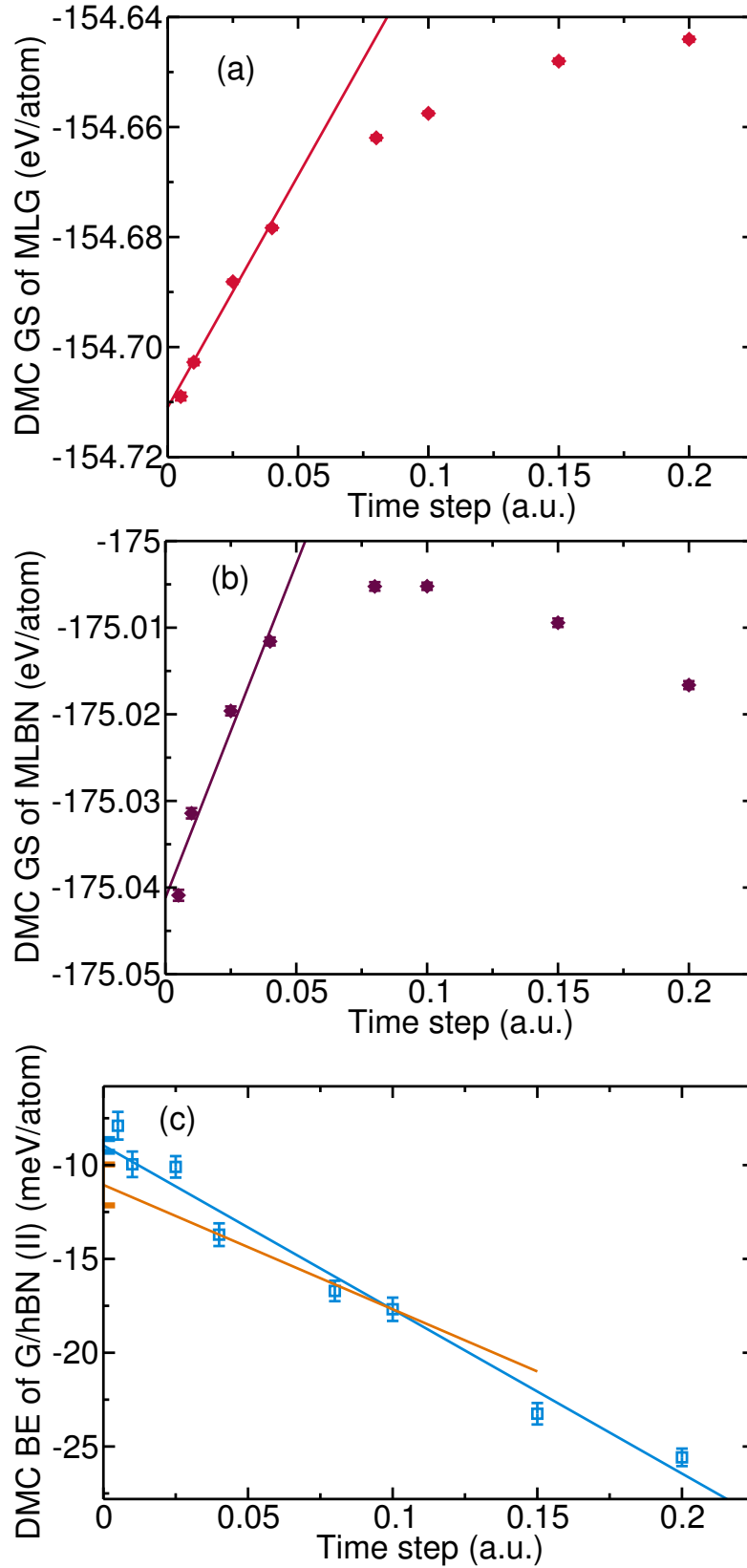


Figure 3.2: (a) Non-twist averaged DMC ground-state (GS) energy of monolayer graphene (MLG), (b) DMC GS energy of monolayer hBN (MLBN), and (c) DMC BE of stacking pattern II of bilayer G/hBN against time step for a supercell consisting of 3×3 primitive cells.

Fig. 3.2(c) is $-8.9(3)$ meV/atom, which is not significantly different from $-11(1)$ meV/atom using two time steps 0.04 and 0.1. We therefore extrapolate all DMC ground-state energies and BEs to zero time step using the latter choice of time step as it considerably reduces the computational time while retaining quantitative accuracy.

3.3.2 DMC binding energy of G/hBN

In Fig. 3.3, we plot the BE curves of bilayer G/hBN for four different stacking configurations as a function of interlayer separation. We fit Eq. 2.3 to the DMC BEs per atom. Our results show that the stacking pattern II is the most stable form of G/hBN. The electrostatic attraction of positive charged B to π_z electron of C atoms keeps them on top of each other while the repulsion of negative charged N by π_z electron of C atoms leads N to the centre of graphene hexagons further from C atoms.

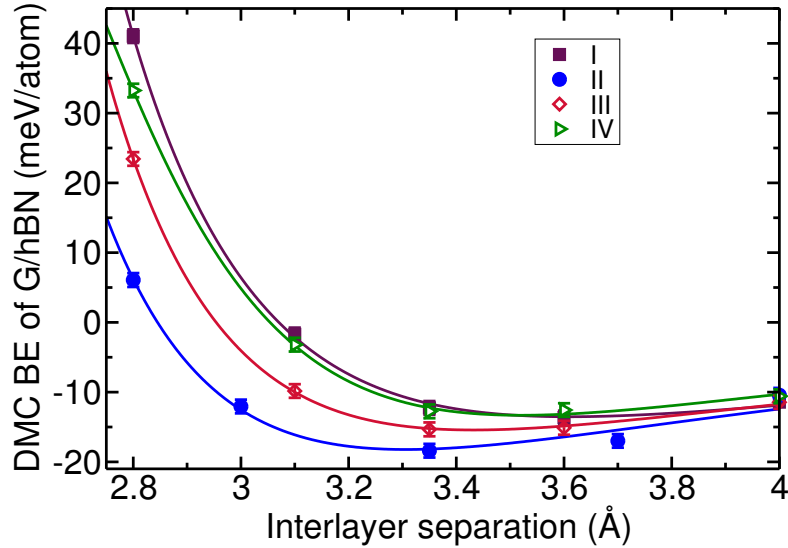


Figure 3.3: DMC BE curve of bilayer G/hBN against the interlayer separation for configuration stacks I–IV introduced in Fig. 3.1.

In Table 3.1, we compare our DMC BEs with that of calculated using DFT for each stacking configuration. The DMC BEs from most to least stable stacks are

18.7(9), 15.5(5), 13.6(6) and 13.4(7) meV/atom, corresponding to configurations II, III, I and IV, respectively. In general, DFT-LDA underestimates the BE by up to 40% while the DFT-vdW overbinds the G/hBN heterostructure by up to 50%. DFT-RPA [105] slightly overbinds the bilayer system compared with our DMC results.

Table 3.1: Comparison of BE of G/hBN using DFT and DMC methods. The DFT-LDA and the first column of DFT-vdW BEs are estimated from the BE graph of Ref. [110]. BEs in the second column of DFT-vdW are obtained in the Ref. [111]. The configurations are introduced in Fig. 3.3.

Conf.	BE (meV/atom)			
	DFT-LDA [110]	DFT-vdW [110, 111]	DFT-RPA [105]	DMC
I	~ 7.5	$\sim 25, 28.50$	15.5	13.6(6)
II	~ 17	$\sim 35, 33.75$	20.75	18.7(9)
III	~ 12.5	~ 30	17.75	15.5(5)
IV	~ 7.5	$\sim 25, 29.50$	16.25	13.4(7)

Comparing the relative DMC BEs in Table 3.2 indicates that the most stable stacking configuration II has a 5.1(8) meV/atom larger BE than the least stable stacked form I. This is similar to the difference of 5.25 meV/atom calculated by DFT-RPA [105] and DFT-vdW [111]. The difference in the DMC BEs of configurations I and IV is 0.2(7) meV/atom, which is negligible as predicted by DFT [105, 110, 111]. Although DFT-LDA and DFT-vdW BEs give quantitatively wrong BEs, they predict the correct trend for the stability of different stacking configurations.

Table 3.2: Relative BE of G/hBN for different stacking patterns (Fig. 3.3) using DFT and DMC methods. The DFT-LDA and the first column of DFT-vdW BEs are estimated from the BE graph of Ref. [110]. The BEs in the second column of DFT-vdW are obtained in Ref. [111]. E_{BE}^X denotes the BE of stacking configuration X .

Type	Relative BE (meV/atom)			
	DFT-LDA [110]	DFT-vdW [110, 111]	DFT-RPA [105]	DMC
$E_{\text{BE}}^{\text{II}} - E_{\text{BE}}^{\text{I}}$	~ 9.5	$\sim 10, 5.25$	5.25	5.1(8)
$E_{\text{BE}}^{\text{II}} - E_{\text{BE}}^{\text{III}}$	~ 4.5	~ 5	3.0	3.2(8)
$E_{\text{BE}}^{\text{II}} - E_{\text{BE}}^{\text{IV}}$	~ 9.5	$\sim 10, 4.25$	4.5	5.3(8)
$E_{\text{BE}}^{\text{IV}} - E_{\text{BE}}^{\text{I}}$	~ 0	$\sim 0, 1$	0.75	0.2(7)

The DMC equilibrium separations in Table 3.3 are within the range 3.31–3.61 Å, which is similar to that of 3.2–3.5 Å and 3.35–3.55 Å predicted by DFT-vdW [110, 111] and DFT-RPA [105], respectively. The DMC equilibrium separation of most stable configuration II is 3.31(3) Å, which is in excellent agreement with the experimental value of 3.32(43) Å [99].

Table 3.3: Comparison of equilibrium interlayer separation of G/hBN using DFT and DMC methods for different stacking configurations introduced in Fig. 3.3.

Conf.	Interlayer separation (Å)		
	DFT-vdW [110, 111]	DFT-RPA [105]	DMC
I	3.5, 3.49	3.55	3.61(3)
II	3.2, 3.30	3.35	3.31(3)
III	3.4	~ 3.4	3.43(4)
IV	3.4, 3.45	3.5	3.53(5)

3.3.3 Breathing mode optical phonon frequency of G/hBN

In figure 3.4, we plot the DFT-LDA phonon dispersion curves at the relaxed in-plane lattice parameter 2.47 Å and the relaxed equilibrium separations of 3.5 and 3.2 Å for stacking configurations I and II, respectively. Our results are in agreement with those obtained using DFT-vdW [111] and different from a recent phonon dispersion obtained using DFT-LDA [112], in which different lattice parameters and different method of displacing atoms are used. We calculate the DFT-LDA out-of-plane zone-centre breathing mode optical phonon (ZO) frequencies to be 72 and 87 cm⁻¹ for stacking arrangements I and II, respectively. ZO frequencies can be measured using Raman spectroscopy.

To calculate the DMC ZO frequencies, we rewrite the interlayer BE per atom of G/hBN within the B–O approximation as

$$E_{\text{BE}}(d) = E_0 + \frac{1}{8}\mu\omega_{\text{ZO}}^2(d - d_0)^2 + \mathcal{O}(d - d_0)^3, \quad (3.2)$$

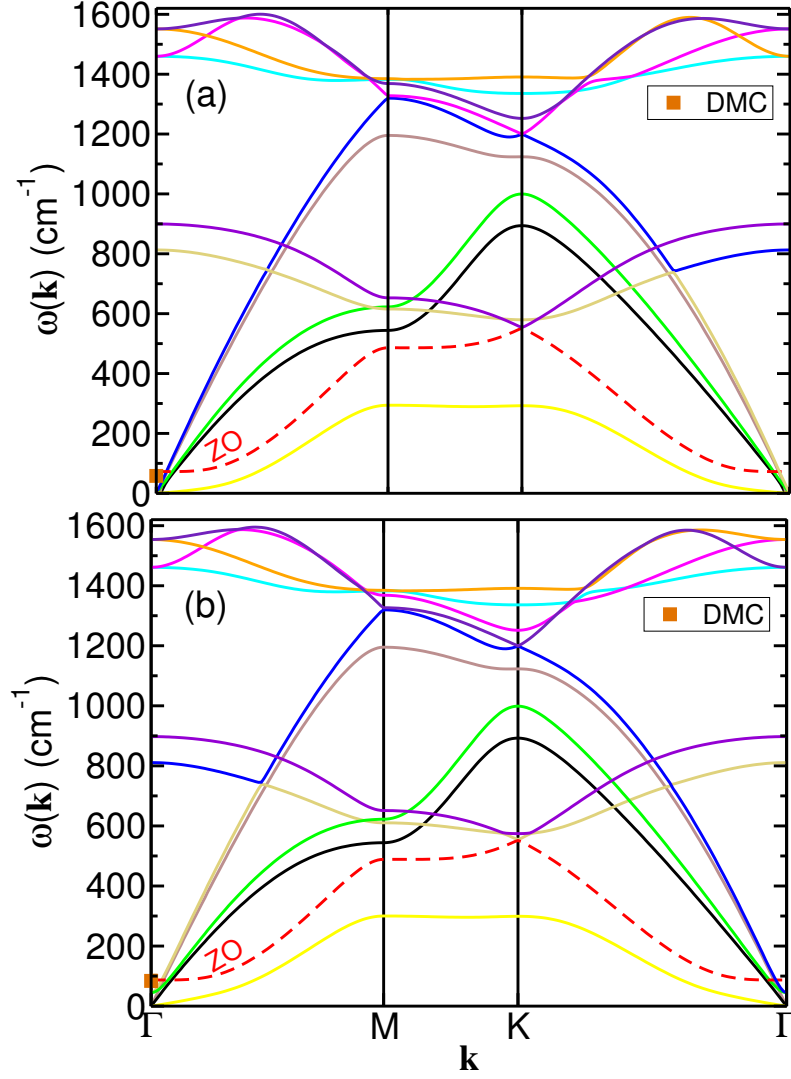


Figure 3.4: DFT-LDA phonon dispersions of bilayer G/hBN for stacking configurations (a) I and (b) II. The ZO frequencies are shown by dashed red curves and the DMC ZO frequencies at Γ point are shown by orange squares.

where E_0 is the BE per atom at the equilibrium separation d_0 , ω_{ZO} is the ZO phonon frequency and $\mu = 2m_c(m_B+m_N)/(2m_c+m_B+m_N)$ is the reduced mass of a primitive cell of G/hBN including the mass of carbon m_c , boron m_B , and nitrogen m_N . The ZO phonon frequency in Eq. 3.2 is obtained by $\omega_{\text{ZO}} = 2\sqrt{E''_{\text{BE}}/\mu}$, where E''_{BE} is the second derivative of the BE at the equilibrium interlayer separation. Table. 3.4 shows that although BEs of G/hBN are changing smoothly from one stack to another, the breathing mode frequencies are 58–84 cm^{-1} , almost the same within the range of error bars for all stacking arrangements. The average of breathing modes over four configurations is 70(15) cm^{-1} .

Table 3.4: DMC equilibrium separation d_0 , static-lattice DMC BE at equilibrium separation, second derivative of the BE at the minimum $E''_{BE}(d_0)$, and ZO frequency ω_{ZO} for four stacks of bilayer G/hBN.

Conf. type	BE (meV/atom)	$E''_{BE}(d_0)$ (meVÅ ⁻² /atom)	ω_{ZO} (cm ⁻¹)
I	13.6(6)	38(5)	58(7)
II	18.7(9)	79(18)	84(19)
III	15.5(5)	54(6)	69(8)
IV	13.4(7)	56(17)	71(21)

3.3.4 DMC in-plane shear mode of G/hBN

In Fig. 3.5 we plot the DMC BE of G/hBN as a function of translating path O–P for different stacking patterns shown in Fig. 3.1. We choose the interlayer separation to be 3.35 Å and fit

$$E_{BE} = A + B\cos(2\pi(x - 1)/3), \quad (3.3)$$

to the DMC BEs E_{BE} , where A and B are fitting parameters and x is the sliding

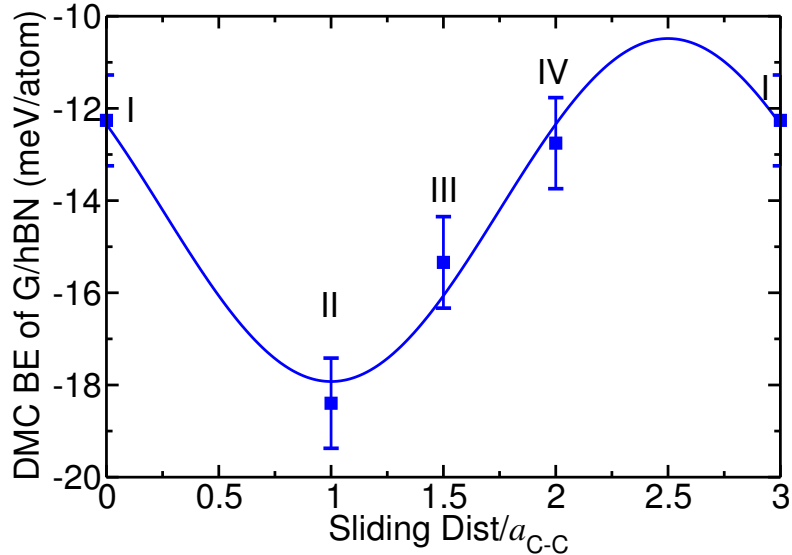


Figure 3.5: DMC BE of bilayer G/hBN against the sliding distance for stacking configurations I–IV introduced in Fig. 3.1.

distance divided by a_{C-C} . The denominator 3 appears in the argument of cos in the fitting curve because the stacking pattern repeats after translating hBN by 3 a_{C-C} . The second derivative of the fitting curve at minimum is 16(3) meV/atom giving

the in-plane phonon frequency or the shear mode $516(97) \text{ cm}^{-1}$; however the error bars in the BEs are quite large, around 1 meV/atom ; and need to be reduced. In practice, a large region of G/hBN would feature all types of configurations, which should be considered in the treatment of shear mode, but here the configuration II is only considered.

3.4 Conclusion

We have found that the BE of G/hBN is $18.7(9) \text{ meV/atom}$ for the most stable stacking form II, where boron atoms in hBN are right above the carbon atom of one sublattice of graphene while nitrogen atoms are centred on the graphene hexagons. Nevertheless, little variation in the BEs of different displacements is less than 5 meV/atom . Our result consisted with weak coupling of layers that allows moiré patterns to form and slightly change the interlayer separation within $3.31 - 3.61 \text{ (\AA)}$. BE of G/hBN is the same as $17.7(9) \text{ meV/atom}$ in AB-stacked bilayer graphene discussed in chapter 2. DFT-LDA considerably underestimates while DFT-vdW overestimates the BE of 2D bilayers. The breathing phonon frequencies for different translation of layers are in the range of $58 - 89 \text{ cm}^{-1}$ and the shear phonon frequency for stacking pattern II is $516(97) \text{ cm}^{-1}$.

Biexcitons in monolayer transition-metal dichalcogenides

4.1 Introduction

During the last five years, many researchers have focused on the remarkable properties of 2D monolayer transition-metal dichalcogenides (TMDCs) such as MoS₂, MoSe₂, MoTe₂, WS₂, WSe₂, and WTe₂. Monolayer TMDCs are semiconductors with a hexagonal plane of transition-metal atoms sandwiched between two hexagonal planes of chalcogen atoms. Unlike graphene that does not have an electronic band gap, these crystals exhibit direct band gaps at the K and the K' points of the hexagonal Brillouin zone, opening up potential applications for optoelectronic devices.

One particular interesting aspect of 2D TMDCs is the strong excitonic effects that are present in their photoabsorption and photoluminescence spectra. Many-body GW calculations indicate that TMDCs exhibit substantial (~ 1 eV) exciton binding energies [113–115]. A number of experimental works have confirmed that the exciton binding energy is large and, furthermore, have reported nonhydrogenic Rydberg lines in the spectra [116, 117]. Experimental works have also found lines

ascribed to trion (charged excitons) [118–120] and biexcitons [121–125].

The nonhydrogenic nature of the excitonic energy spectrum results from nonlocal screening effects, i.e., the modification of the form of the Coulomb interaction between charge carriers by the polarisation of the surrounding atoms in the semiconductor. There have been some incomplete [126] and approximate [127] attempts to study biexcitons in TMDCs. A recent study used the DMC method along with an approximate form of nonlocal screening to provide the binding properties of biexcitons [128]. Another study using the exact form of nonlocal screening within path integral Monte Carlo (PIMC) has shown discrepancies between the theoretical and experimental properties of these charge complexes [129]. Therefore, comprehensive and accurate binding-energy data are urgently required to resolve the discrepancies. In this chapter we provide numerically exact binding-energy data of biexcitons for a wide range of nonlocal screening strengths.

4.2 Electrostatic interactions

Suppose a free-standing 2D semiconductor sheet of zero thickness $z = 0$ contains a continuous charge density $\rho(x, y)\delta(z)$. The electric displacement field is defined as $\mathbf{D} = \epsilon_0\mathbf{E} + \mathbf{P}$, where \mathbf{E} is the electric field, ϵ_0 is the electric permittivity of free space and $\mathbf{P} = \mathbf{P}_{2D}(x, y)\delta(z)$ is the polarisation field or the density of induced electric dipole moments with the in-plane polarisation $\mathbf{P}_{2D}(x, y)$. By using Gauss's law $\nabla \cdot \mathbf{D} = \rho(x, y)\delta(z)$,

$$-\nabla \cdot \mathbf{E} = \nabla^2\phi(\mathbf{r}) = \frac{-\rho(x, y)\delta(z) + [\nabla \cdot \mathbf{P}_{2D}(x, y)]\delta(z)}{\epsilon_0}, \quad (4.1)$$

where the 2D polarisation in terms of the induced charge density ρ_{ind} is

$$[\nabla \cdot \mathbf{P}_{2D}(x, y)]\delta(z) = -\rho_{\text{ind}}(x, y, 0) = -\chi_{2D}\nabla^2\phi(x, y, 0)\delta(z), \quad (4.2)$$

considering the fact that $\mathbf{P}_{2D}(x, y)$ is proportional to the in-plane component of \mathbf{E} and χ_{2D} is the 2D electric polarisability. Substituting Eq. 4.2 into Eq. 4.1 gives

$$\nabla^2\phi(\mathbf{r}) = -\frac{\rho(x, y)\delta(z) + \chi_{2D}[\nabla^2\phi(x, y, 0)]\delta(z)}{\epsilon_0}. \quad (4.3)$$

The Fourier transform of Eq. 4.3 gives the electrostatic potential due to a 2D semiconductor

$$\phi(\mathbf{q}, k) = \frac{\rho(\mathbf{q}) - \chi_{2D}q^2\phi(\mathbf{q}, z = 0)}{\epsilon_0(q^2 + k^2)}, \quad (4.4)$$

where \mathbf{q} and k are the in-plane and z components of the wavevector, respectively. The in-plane electrostatic potential is

$$\begin{aligned} \phi(\mathbf{q}, z = 0) &= \frac{1}{2\pi} \int \phi(\mathbf{q}, k) dk \\ &= \frac{1}{2\epsilon_0 q} [\rho(\mathbf{q}) - \chi_{2D}q^2\phi(\mathbf{q}, z = 0)]. \end{aligned} \quad (4.5)$$

Then by rearranging, we find the in-plane electrostatic potential to be

$$\begin{aligned} \phi(\mathbf{q}, z = 0) &= \frac{2\pi\rho(\mathbf{q})}{4\pi\epsilon_0 q(1 + 2\pi\chi_{2D}q/4\pi\epsilon_0)} \\ &= \frac{2\pi\rho(\mathbf{q})}{4\pi\epsilon_0 q(1 + r^*q)}, \end{aligned} \quad (4.6)$$

where $r^* = 2\pi\chi_{2D}/4\pi\epsilon_0$ is the screening length and $1 + r^*q$ in the denominator is \mathbf{q} -dependent dielectric function $\epsilon(\mathbf{q})$ in the directions parallel to the plane of the 2D system [130]. The polarisability χ_{2D} has SI units of C^2J^{-1} and $4\pi\epsilon_0$ has units of $C^2L^{-1}J^{-1}$; therefore r^* has units of length L.

If the 2D semiconductor contains a point charge q_i at the origin, then the Fourier components of the interaction between a point charge q_j living in the 2D semiconductor in the presence of q_i are

$$w(\mathbf{q}) = \frac{2\pi q_i q_j}{4\pi\epsilon_0 q(1 + r^*q)}. \quad (4.7)$$

By the inverse Fourier transform of Eq. 4.7, we can determine the effective potential $w(\mathbf{r}) = \frac{q_i q_j}{4\pi\epsilon_0 r^*} V(r/r^*)$ between the two point charges, which is the Keldysh potential

$$V\left(\frac{r}{r^*}\right) = \frac{\pi}{2} \left[H_0\left(\frac{r}{r^*}\right) - Y_0\left(\frac{r}{r^*}\right) \right], \quad (4.8)$$

where $H_n(x)$ is a Struve function and $Y_n(x)$ is a Neumann function (Bessel function of the second kind) [131]. The interaction energy at small r^* ($r \gg r^*$) is a Coulomb interaction: $w(\mathbf{r}) \approx q_i q_j / (4\pi\epsilon_0 r)$; while it is approximately logarithmic at large r^* ($r \ll r^*$): $w(\mathbf{r}) \approx q_i q_j [\log(2r^*/r) - \gamma] / (4\pi\epsilon_0 r^*)$, where $\gamma \approx 0.5772$ is Euler's constant. Once $w(\mathbf{r})$ is known, the Schrödinger equation can be solved for charged particles in a 2D semiconductor

$$\left[-\sum_i \frac{\hbar^2}{2m_i} \nabla_i^2 + \frac{1}{2} \sum_{i \neq j} \frac{q_i q_j}{r^*} V\left(\frac{r_{ij}}{r^*}\right) \right] \psi(\mathbf{r}) = E\psi(\mathbf{r}), \quad (4.9)$$

where m_i is the mass of particle i with charge q_i , r_{ij} is the the separation of particles i and j , and E is the energy eigenvalue.

4.3 Units and scaling for different interactions

The Schrödinger equation for an exciton with the logarithmic interaction ($r \ll r^*$) is

$$\left[-\frac{\hbar^2}{2\mu} \nabla_{\text{eh}}^2 - \frac{e^2}{4\pi\epsilon_0 r^*} \left\{ \log\left(\frac{2r^*}{r_{\text{eh}}}\right) - \gamma \right\} \right] \psi_{\text{X}} = E_{\text{X}} \psi_{\text{X}}, \quad (4.10)$$

where E_{X} is the total energy of the exciton and $\mu = m_e m_h / (m_e + m_h)$ is the reduced mass of the electron-hole pair. Let

$$r_0 = \sqrt{\frac{4\pi\epsilon_0 r^* \hbar^2}{2e^2 \mu}}, \quad (4.11)$$

and

$$E_0 = \frac{e^2}{4\pi\epsilon_0 r^*}. \quad (4.12)$$

Using the dimensionless exciton energy $\mathcal{E}_X = E_X/E_0$,

$$\left[-r_0^2 \nabla_{\text{eh}}^2 + \log\left(\frac{r_{\text{eh}}}{r_0}\right) + \gamma - \log(2) - \log\left(\frac{r^*}{r_0}\right) \right] \psi_X = \mathcal{E}_X \psi_X, \quad (4.13)$$

and introducing dimensionless coordinates $\tilde{r} = r/r_0$,

$$\left[-\tilde{\nabla}_{\text{eh}}^2 + \log(\tilde{r}_{\text{eh}}) + \gamma - \log(2) - \log\left(\frac{r^*}{r_0}\right) \right] \psi_X = \mathcal{E}_X \psi_X. \quad (4.14)$$

\mathcal{E}_X in Eq. 4.14 depends on r^* and the reduced mass via the constant term $\log(r^*/r_0)$ in the Hamiltonian. In our calculations, we use the rescaled exciton energy

$$\mathcal{E}_X = \mathcal{E}_{X0} - \frac{1}{2} \log(2\mu r^*), \quad (4.15)$$

where the energy $\mathcal{E}_{X0} = 0.41057739(7)$ is obtained by DMC [132]. The Schrödinger equation for the biexciton with the logarithmic interaction is

$$\left[-\frac{\hbar^2}{2m_e} \nabla_{e_1}^2 - \frac{\hbar^2}{2m_e} \nabla_{e_2}^2 - \frac{\hbar^2}{2m_h} \nabla_{h_1}^2 - \frac{\hbar^2}{2m_h} \nabla_{h_2}^2 \right. \\ \left. + \frac{e^2}{4\pi\epsilon_0 r^*} \left\{ -\log\left(\frac{2r^*}{e^\gamma r_{e_1 h_1}}\right) - \log\left(\frac{2r^*}{e^\gamma r_{e_2 h_2}}\right) - \log\left(\frac{2r^*}{e^\gamma r_{e_1 h_2}}\right) \right. \right. \\ \left. \left. - \log\left(\frac{2r^*}{e^\gamma r_{e_2 h_1}}\right) + \log\left(\frac{2r^*}{e^\gamma r_{e_1 e_2}}\right) + \log\left(\frac{2r^*}{e^\gamma r_{h_1 h_2}}\right) \right\} \right] \psi_{XX} = E_{XX} \psi_{XX}, \quad (4.16)$$

where $m_{e(h)}$ is the mass of the electrons (holes) and E_{XX} is the total energy of the biexciton. Rescaling the biexciton energy $\mathcal{E}_{XX} = E_{XX}/E_0$ and using Eqs. 4.11 and 4.12,

$$\left[-\frac{\mu r_0^2}{m_e} \nabla_{e_1}^2 - \frac{\mu r_0^2}{m_e} \nabla_{e_2}^2 - \frac{\mu r_0^2}{m_h} \nabla_{h_1}^2 - \frac{\mu r_0^2}{m_h} \nabla_{h_2}^2 \right. \\ \left. + \log\left(\frac{r_{e_1 h_1}}{r^*}\right) + \log\left(\frac{r_{e_2 h_2}}{r^*}\right) + \log\left(\frac{r_{e_1 h_2}}{r^*}\right) + \log\left(\frac{r_{e_2 h_1}}{r^*}\right) \right. \\ \left. - \log\left(\frac{r_{e_1 e_2}}{r^*}\right) - \log\left(\frac{r_{h_1 h_2}}{r^*}\right) + 2(\gamma - \log(2)) \right] \psi_{XX} = \mathcal{E}_{XX} \psi_{XX}. \quad (4.17)$$

Then the Schrödinger equation of the biexciton using dimensionless $\tilde{r} = r/r_0$,

$$\left[-\frac{\mu}{m_e} \tilde{\nabla}_{e_1}^2 - \frac{\mu}{m_e} \tilde{\nabla}_{e_2}^2 - \frac{\mu}{m_h} \tilde{\nabla}_{h_1}^2 - \frac{\mu}{m_h} \tilde{\nabla}_{h_2}^2 \right. \\ \left. + \log(\tilde{r}_{e_1 h_1}) + \log(\tilde{r}_{e_2 h_2}) + \log(\tilde{r}_{e_1 h_2}) + \log(\tilde{r}_{e_2 h_1}) \right. \\ \left. - \log(\tilde{r}_{e_1 e_2}) - \log(\tilde{r}_{h_1 h_2}) + 2(\gamma - \log(2)) - 2\log\left(\frac{r^*}{r_0}\right) \right] \psi_{XX} = \mathcal{E}_{XX} \psi_{XX}. \quad (4.18)$$

To find the binding energy (BE) of the biexciton with the logarithmic interaction and its scaling at different r^* , we rewrite the total energy of the exciton in Eqs. 4.14 as

$$\tilde{\mathcal{E}}_X + \gamma - \log(2) - \log\left(\frac{r^*}{r_0}\right) = \mathcal{E}_X, \quad (4.19)$$

and the total energy of the biexciton in Eq. 4.18 as

$$\tilde{\mathcal{E}}_{XX}(\mu) + 2(\gamma - \log(2)) - 2\log\left(\frac{r^*}{r_0}\right) = \mathcal{E}_{XX}. \quad (4.20)$$

The rescaled BE of biexciton in the logarithmic limit is therefore given by

$$E_{\text{BE}}^{\text{log}}(\mu) = 2\mathcal{E}_X - \mathcal{E}_{XX} = 2\tilde{\mathcal{E}}_X - \tilde{\mathcal{E}}_{XX}(\mu). \quad (4.21)$$

Eq. 4.21 shows that the BE of biexciton with the logarithmic interaction is independent of r^* in these units and is constant for a given μ (Fig. 4.1).

The BE of the biexciton at finite r^* in the 2D Keldysh interaction, including the Coulomb interaction ($r^* = 0$) is dependent on r^* and μ :

$$E_{\text{BE}}^{2D}(\mu, r^*) = 2\mathcal{E}_x(\mu, r^*) - \mathcal{E}_{xx}(\mu, r^*), \quad (4.22)$$

where $\mathcal{E}_x = E_x/R_\infty^*$ and $\mathcal{E}_{xx} = E_{xx}/R_\infty^*$ are the dimensionless energies of the exciton E_x and the biexciton E_{xx} defined in Eqs. 4.10 and 4.16, respectively. R_∞^* is the exciton Rydberg:

$$R_\infty^* = \frac{\mu e^4}{2(4\pi\epsilon_0)^2 \hbar^2}, \quad (4.23)$$

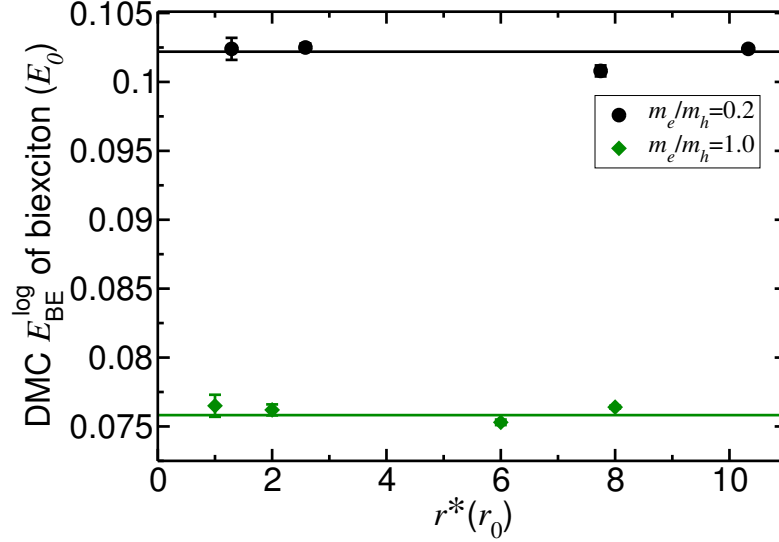


Figure 4.1: The rescaled DMC BE of a biexciton with the logarithmic interaction against r^* at two different mass ratios $m_e/m_h = 0.2$ and $m_e/m_h = 1$.

and the length can be scaled by using the exciton Bohr radius

$$a_0^* = \frac{4\pi\epsilon_0\hbar^2}{\mu e^2}. \quad (4.24)$$

Sometimes we have used the Bohr radius

$$a_0 = \frac{4\pi\epsilon_0\hbar^2}{m_e e^2}, \quad (4.25)$$

to rescale r^* . Excitonic units eliminate the mass ratio dependence from exciton energy.

4.4 Excitons and biexcitons with distinguishable particles

The ground-state wave functions of excitons and biexcitons with distinguishable particles (opposite-spin electrons and holes) are nodeless and symmetric under exchange of electrons and under exchange of holes, leading to the fixed-node DMC

energy being exact. Our trial wave functions for the biexciton are of the form $\psi(\mathbf{R}) = \exp[J(\mathbf{R})]$ with the Jastrow form

$$J(\mathbf{R}) = \frac{1}{2} \sum_{i \neq j} u(r_{ij}) + \sum_{i \neq j; k} H(r_{ij}, r_{ik}, r_{jk}) + u_{eh}(r_{eh}) + u_{ee}(r_{ee}) + u_{hh}(r_{hh}) \quad (4.26)$$

where u and H are, respectively, two-body and three-body cusplless polynomials in the interparticle distances, which are truncated smoothly at finite range [76, 133].

u_{eh} , u_{ee} and u_{hh} are pairwise terms

$$u_{eh}(r_{eh}) = c_1 r_{eh}^2 \log(r_{eh}) e^{-c_2 r_{eh}^2} - [1 - e^{-c_2 r_{eh}^2}] c_3 r_{eh}, \quad (4.27)$$

between electrons and holes (r_{eh}) and

$$u_{ee}(r_{ee}) = c_4 r_{ee}^2 \log(r_{ee}) e^{-c_5 r_{ee}^2}, \quad (4.28)$$

between electrons (r_{ee}) and

$$u_{hh}(r) = c_6 r_{hh}^2 \log(r_{hh}) e^{-c_7 r_{hh}^2}, \quad (4.29)$$

between holes (r_{hh}). The Jastrow form of an exciton only includes u and u_{eh} terms corresponding to the two-body interactions of an electron–hole pair. In Eqs. 4.27–4.29, we require $c_1 = e^2 \mu / [2(4\pi\epsilon_0) \hbar^2 r^*]$, $c_4 = -e^2 m_e / (4(4\pi\epsilon_0) \hbar^2 r^*)$ and $c_6 = -e^2 m_h / (4(4\pi\epsilon_0) \hbar^2 r^*)$ in order to satisfy the analogue of the Kato cusp conditions [24, 25], which ensure that the local energy is nondivergent at coalescence points. c_2 , c_3 , c_5 and c_7 are optimisable parameters but restricted to be positive in order to keep our wave functions normalisable.

Instead of using individual forms u_{eh} , u_{ee} and u_{hh} (Eq. 4.26) for later QMC calculations such as heavy-hole limit and biexcitons with either identical holes or

identical electrons, we introduce a more general and compact form u_0

$$\sum_{i \neq j} u_0(r_{ij}) = \frac{a_1 r_{ij}^2 \log(r_{ij}) + a_2 r_{ij}^2 + a_3 r_{ij}^3}{1 + a_4 r_{ij}^2}, \quad (4.30)$$

where

$$a_1 = \begin{cases} p_i p_j m_i m_j / [2(4\pi\epsilon_0)\hbar^2 r^*(m_i + m_j)] & \text{Distinguishable } e \text{ and } h, \\ p_i p_j m_i m_j / [4(4\pi\epsilon_0)\hbar^2 r^*(m_i + m_j)] & \text{Indistinguishable } e \text{ or } h, \end{cases} \quad (4.31)$$

is determined by the analogue of the Kato cusp conditions for antiparallel- or parallel-spin particles [22]. a_2 to a_4 in Eq. 4.30 are optimisable parameters while we restrict $a_3 < 0$ and $a_4 > 0$ to make the wave functions normalisable. All the free parameters in our trial wave functions for biexcitons containing distinguishable particles are optimised by unreweighted variance minimisation [26, 27] and energy minimisation [28–30].

By calculating the pair distribution function (PDF) we can find some additional information about the system. The electron–hole PDF at $r = 0$ is proportional to the rate of electron–hole recombination. When charge carriers are present at the same point of space, there is likely to be an energy penalty. This effect may be described by introducing an additional contact interaction, which includes electron–electron, electron–hole and hole–hole pair densities that can be evaluated by the PDF. It gives the form of u_{eh} and u_{ee} pairwise terms in the Jastrow function, also indicates the size of the biexciton and whether particles are localised. The PDF is the normalised probability of finding a particle at radial distance r given that there is one at the origin. The PDF between particles i and j in an exciton or a biexciton is,

$$g_{ij}(r) = \frac{1}{2\pi r} \langle \delta(r - |\mathbf{r}_i - \mathbf{r}_j|) \rangle. \quad (4.32)$$

$g(r)$ is accumulated in QMC simply by binning the interparticle distances throughout the simulation. We evaluated the extrapolated estimate of the PDF, which

is twice the DMC mixed estimate minus the VMC estimate. The error in the extrapolated estimate is quadratic in the error in the trial wave function [22].

In Fig. 4.2, we show the PDF of biexcitons with distinguishable particles in the logarithmic interaction for two different mass ratios $m_e/m_h = 0.4$ and $m_e/m_h = 1$. Our results show that the long-range biexciton wave functions are relatively independent of mass ratios changing between 0.4 – 1.

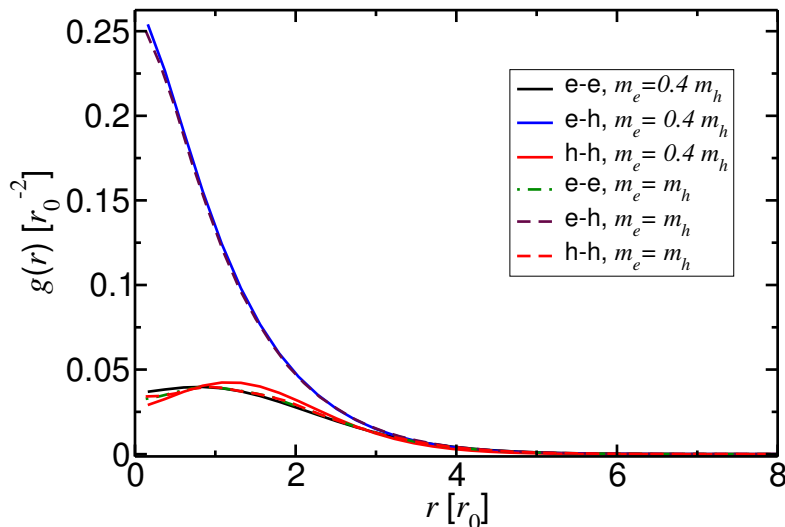


Figure 4.2: The PDF of a biexciton with distinguishable particles against the interparticle separation in the logarithmic limit ($r^* \rightarrow \infty$) and two different mass ratios $m_e/m_h = 0.4$ and $m_e/m_h = 1$.

4.5 Biexcitons with indistinguishable particles

The ground-state wave function of biexcitons composed of indistinguishable particles (e.g., same-spin electrons or same-spin holes) is antisymmetric. Here, we consider a biexciton consisting of same-spin electrons and opposite-spin holes and approximate its wave function by the form $\psi(\mathbf{R}) = S_{ee}(\mathbf{R})\exp[J(\mathbf{R})]$, where J is the Jastrow form contained the first two terms of Eq. 4.26 and u_0 defined in Eq. 4.30. The polynomial term S_{ee} is antisymmetric under the exchange of elec-

trons and is symmetric under the exchange of holes,

$$S_{ee}(\mathbf{R}) = x_{ee} + \eta_{ee}(r_{ee})x_{ee} + \eta_{e_1h_1}(r_{e_1h_1})x_{e_1h_1} + \eta_{e_1h_2}(r_{e_1h_2})x_{e_1h_2} \\ - \eta_{e_2h_1}(r_{e_2h_1})x_{e_2h_1} - \eta_{e_2h_2}(r_{e_2h_2})x_{e_2h_2}, \quad (4.33)$$

where r_{ee} is the electron–electron distance, $r_{e_ih_j}$ ($i, j = 1, 2$) are the electron i –hole j distance and $x_{ee} = r_{ee}\cos(\theta_{ee})$, in which θ_{ee} is the polar angle of r_{ee} . In Eq. 4.33, $\eta_{ee} = \sum_{n \neq 0,1} a_n r_{ee}^n$ and $\eta_{e_ih_j} = \sum_{m \neq 1} b_m r_{e_ih_j}^m$ are cusplless polynomials in r with optimisable parameters a and b . The restrictions in the summands insure that η change smoothly by increasing the order of expansion.

By relabeling S_{ee} for biexcitons consisting of opposite-spin electrons and same-spin holes, we can similarly write the charge conjugation of S_{ee} , S_{hh} , which is antisymmetric under the exchange of holes and symmetric under the exchange of electrons. Therefore, the total energies of biexcitons that we have calculated using S_{ee} for relatively heavy electrons are equivalent to the total energies obtained using S_{hh} for the relatively heavy holes.

S_{ee} for electrons and similarly S_{hh} for holes introduce a correct form of fixed-node wave function by introducing x_{ee} or x_{hh} . Allowing η to vary is effectively backflow transformation of that simple wave function, which introduces some variation of freedom into the node without damaging the topology of the nodal surface. DMC energy of such a system would be variational with respect to the nodal surface.

We optimise our antisymmetric wave function using unweighted variance minimisation, which gives a lower variance of the VMC energy than the energy minimisation method; however, optimising the free parameters in η is the most difficult part of our calculations. It may be due to the non-truncated form of wave function at the finite range of interparticle distances. However our wave function generates correct results as the Jastrow term tends to zero at large particle separations and the variational calculations prevent the energy being large.

For different polynomial order of η in Eq. 4.33, we compare the VMC ground-state energy, variance and DMC energy of biexcitons with same-spin electrons for the logarithmic interaction (Table 4.1) and the 2D Keldysh interaction defined in Eq. 4.8 (Table 4.2). Our results show that increasing the order of η decreases the variances indicating that our wave functions are well-behaved; nevertheless, the VMC and DMC energies are independent of the polynomial order of η . Therefore, we expand η in the antisymmetric wave function to third order to simplify optimisations.

Table 4.1: Order of η in the VMC ground-state energy (E_{VMC}), variance and DMC energy (E_{DMC}) of biexcitons with identical electrons in the logarithmic interaction limit. The mass ratio is $m_h/m_e = 0.125$ and the reduced mass is $\mu = 8/9$. DMC energies are extrapolated to zero time step.

$r^*(a_0^*)$	η order	$E_{\text{VMC}} (E_0)$	Variance (E_0)	$E_{\text{DMC}} (E_0)$
8/9	2	0.2051(4)	0.0093	0.2001(3)
	3	0.2041(1)	0.0091	0.2005(6)
	4	0.207(2)	0.0083	0.1999(4)
	6	0.2073(4)	0.0081	0.2010(3)

Table 4.2: Order of η in the VMC ground-state energy (E_{VMC}), variance and DMC energy (E_{DMC}) of biexcitons with identical electrons interacting via the 2D Keldysh interaction. Here, $m_h/m_e = 0.1$, $\mu = 1/2$, and $r^* = 0$ corresponds to the Coulomb interaction. DMC energies are extrapolated to zero time step.

$r^*(a_0^*)$	η order	$E_{\text{VMC}} (R_\infty^*)$	Variance (R_∞^*)	$E_{\text{DMC}} (R_\infty^*)$
0	2	-8.603(1)	0.0676	-8.6112(4)
	3	-8.605(2)	0.0497	-8.6100(4)
	4	-8.605(2)	0.0439	-8.6112(4)
	6	-8.606(2)	0.0425	-8.6120(4)
4	2	-1.0012(1)	0.00022	-1.0030(2)
	3	-1.0013(1)	0.00021	-1.0032(2)
	4	-1.0013(1)	0.00021	-1.0045(2)
	6	-1.0015(1)	0.00020	-1.0030(2)

4.6 Time-step and population-control biases

We choose the DMC time step such that the RMS distance diffused by each particle in one time step is $\ll r_0$ for the logarithmic interactions and $\ll \min\{r_0, a_0^*\}$ for the 2D Keldysh interactions at finite r^* . In Fig. 4.3 for example, we compare the DMC energies of a biexciton with distinguishable particles at different time steps. The results for the logarithmic interaction and $r^* = r_0$ shows that the DMC energy behaves linearly for time steps up to $0.04\hbar/E_0$.

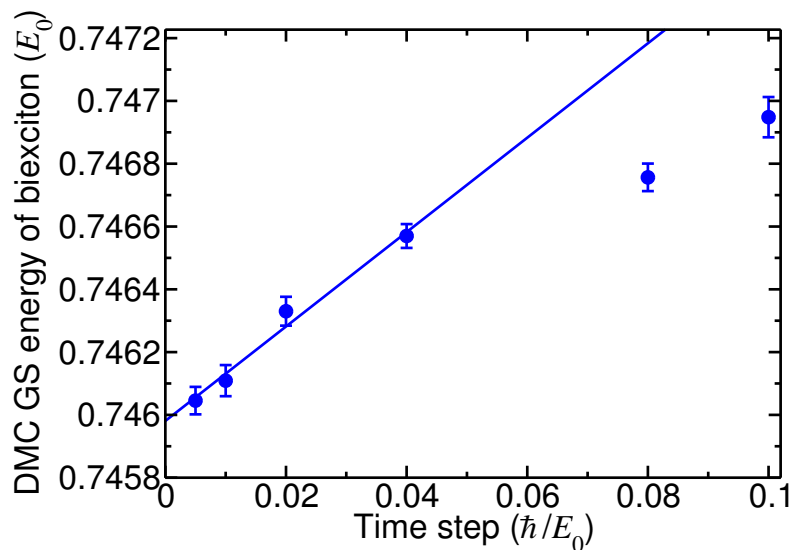


Figure 4.3: DMC ground-state (GS) energy of the biexciton with distinguishable particles against the DMC time step for $\mu = 1/2$ in the logarithmic limit.

To remove the biases due to the finite time steps and populations of walkers, we perform DMC calculations using time steps in the ratio 1:4 with the corresponding target configuration populations being in the ratio 4:1 and linearly extrapolate the DMC energies to zero time step and infinite population.

4.7 Limit of heavy holes

In the limit that the hole mass is large, a biexciton resembles a 2D H_2 molecule, and we may use the B–O approximation [134]. The biexciton total energy is given

by the minimum of the B–O energy curve $U(r)$, where r is the exciton-exciton separation, plus the harmonic zero-point energy of the exciton-exciton vibrations. Higher-order corrections to the energy arise from vibrational anharmonicity.

Consider a biexciton in which the charge carriers interact via the Keldysh interaction. Let $\mathcal{U}(\tilde{r})$ be the B–O curve in Rydberg units, for the case that the electron mass m_e is finite but the hole mass m_h is infinite. Then, at finite electron and hole masses, the B–O potential is $U(r) = \mathcal{U}(r/a_0)R_\infty$ where $R_\infty = m_e e^4 / [2(4\pi\epsilon_0\epsilon)^2 \hbar^2] = (m_e/\mu)R_\infty^*$ is the Rydberg energy and $a_0 = 4\pi\epsilon_0\hbar^2/(m_e e^2) = (\mu/m_e)a_0^*$ is the Bohr radius. Note that $\mathcal{U}(\tilde{r})$ does not depend on the electron or hole mass.

Near the minimum of the potential,

$$\begin{aligned} U(r) &= U(r_{\text{eq}}) + \frac{1}{2}U''(r_{\text{eq}})(r - r_{\text{eq}})^2 + \mathcal{O}(r - r_{\text{eq}})^3 \\ &\equiv U(r_{\text{eq}}) + \frac{1}{2}\frac{m_h + m_e}{2}\omega^2(r - r_{\text{eq}})^2, \end{aligned} \quad (4.34)$$

where $U(r_{\text{eq}})$ is the minimum total energy of the biexciton at the equilibrium separation $r = r_{\text{eq}}$ and U'' is the second derivative of U with respect to r , and $(m_e + m_h)/2$ is the reduced mass of the two excitons.

Then, the total ground-state energy E within the harmonic approximation can be written as

$$\begin{aligned} E &\approx U(r_{\text{eq}}) + \hbar\omega/2 \\ &= \mathcal{U}(r_{\text{eq}})R_\infty + \sqrt{\frac{\hbar^2 R_\infty \mathcal{U}''(r_{\text{eq}})}{2a_0^2(m_h + m_e)}} \\ &= \left[\frac{m_e}{\mu}\mathcal{U}(r_{\text{min}}) + \sqrt{\frac{\mathcal{U}''(r_{\text{min}})m_e^3}{(m_e + m_h)\mu^2}} \right] R_\infty^* \\ &\approx \left[\mathcal{U}(r_{\text{eq}}) + \sqrt{\frac{\mathcal{U}''(r_{\text{eq}})m_e}{m_h}} \right] R_\infty^*, \end{aligned} \quad (4.35)$$

suggesting that the ground-state energy of heavy-hole biexcitons increases as $\sqrt{m_e/m_h}$. The equilibrium separation r_{eq} between heavy holes can be found by direct minimising the B–O ground-state energy with respect to the hole separation.

To find r_{eq} in the logarithmic interaction, we fit

$$e(r) = e_0 + a e^{-r/r_{\text{eq}}} + b \log(r), \quad (4.36)$$

to our QMC biexciton B–O ground-state energies $e(r)$, where e_0 , r_{eq} , a and b are fitting parameters. Fig. 4.4 shows that the DMC ground-state energy e_0 is considerably lower than the VMC ground-state energy, as we expect, while the value of r_{eq} obtained by DMC is slightly higher than that obtained by VMC.

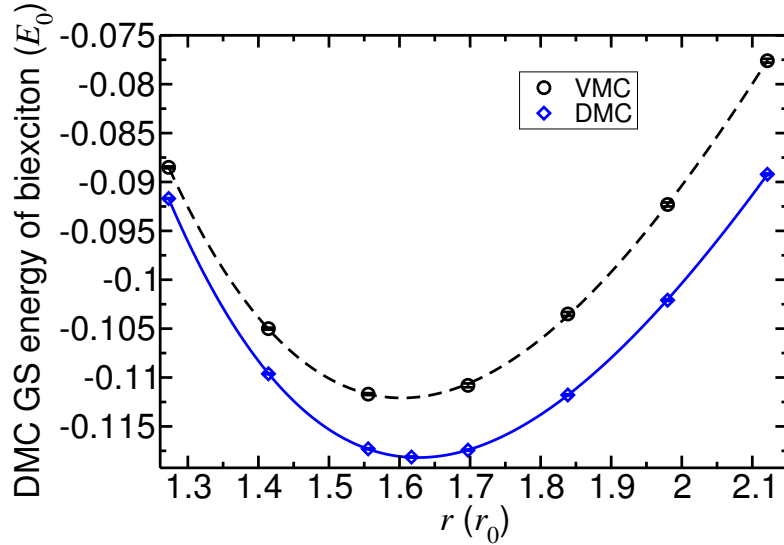


Figure 4.4: DMC ground-state (GS) energy of a heavy-hole biexciton with the logarithmic interaction as a function of hole separation r at $r^* = r_0$. The minimum DMC energy is $e_0 = -0.11828(6)E_0$ at the equilibrium separation $r_{\text{eq}} = 1.6265(7)r_0$ with $U''(r_{\text{eq}}) = 0.3281820(4)E_0/r_0^2$. The VMC equilibrium separation is at $r_{\text{eq}} = 1.604(1)r_0$ with $U''(r_{\text{eq}}) = 0.350490(2)E_0/r_0^2$.

To find r_{eq} for the 2D Keldysh interaction, we fit a polynomial function

$$e(r) = e_0 + \alpha\sqrt{r} + \beta r + \xi r^2, \quad (4.37)$$

to the QMC B–O ground-state energies $e(r)$, where e_0 , α , β and ξ are fitting parameters. The comparison of ground-state energies against the heavy-hole separations at different r^* in Fig. 4.5 and Table 4.3 shows that by increasing r^* in the 2D Keldysh interaction, the equilibrium separation between heavy holes increases, resulting in a reduction of the total energies of biexcitons in excitonic units.

The comparison of U'' and the corresponding r_{eq} calculated using VMC and exact DMC in Table 4.3 shows that VMC gives slightly smaller r_{eq} and slightly larger U'' than DMC for all ranges of r^* in the 2D interaction (similar to the case with logarithmic interaction).

Table 4.3: $U''(r_{\text{eq}})$ and r_{eq} of a heavy-hole biexciton with distinguishable electrons calculated using QMC and the exact DMC ground-state energy e_0 at different finite r^* in the 2D Keldysh interaction defined in Eq. 4.8.

$r^*(a_0^*)$	VMC		DMC		
	$r_{\text{eq}}(a_0^*)$	$U''(r_{\text{eq}})(R_\infty^*/a_0^{*2})$	$r_{\text{eq}}(a_0^*)$	$U''(r_{\text{eq}})(R_\infty^*/a_0^{*2})$	$e_0(R_\infty^*)$
0.5	1.050(1)	1.52(2)	1.0648(5)	1.410(8)	-3.5640(1)
1	1.3863(9)	0.526(6)	1.4050(6)	0.496(4)	-2.49356(8)
2	1.854(1)	0.1774(6)	1.888(1)	0.1634(6)	-1.66770(6)
4	2.526(3)	0.0524(4)	2.570(2)	0.0490(4)	-1.07312(2)
6	3.041(3)	0.0254(1)	3.095(3)	0.0397(1)	-0.81646(4)
8	3.472(3)	0.0151(1)	3.5538(8)	0.0138(2)	-0.66832(4)
60	9.05(2)	0.00033(2)	9.22(8)	0.00036(4)	-0.14678(2)

4.7.1 Binding energy of biexcitons

We calculated the BE of biexcitons at different mass ratios and then fitted the polynomial

$$E_{\text{BE}}(x) = E_{\text{BE}}(0) + A_1x^{1/2} + A_2x + A_3x^{3/2} + A_4x^2, \quad (4.38)$$

to our DMC binding energies $E_{\text{BE}}(x)$, where $x = m_e/m_h$, and $E_{\text{BE}}(0)$ and A_i ($i = 1 - 4$) are fitting parameters.

Fig. 4.6 in the limit of logarithmic interaction shows that the BE of a biexciton

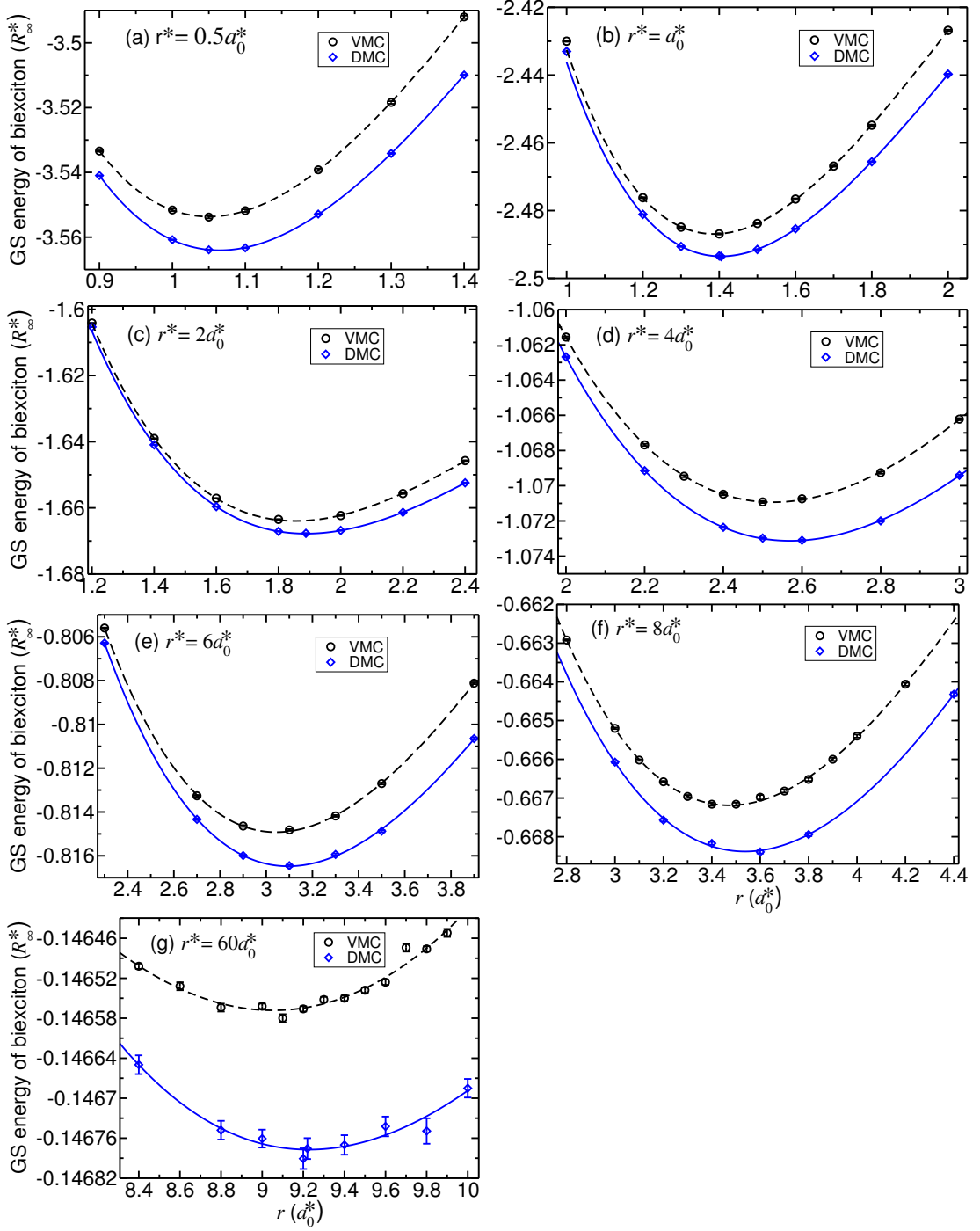


Figure 4.5: VMC and exact DMC ground-state (GS) energies of heavy-hole biexcitons with the 2D Keldysh interaction as a function of hole separations at (a) $r^* = 0.5a_0^*$, (b) $r^* = a_0^*$, (c) $r^* = 2a_0^*$, (d) $r^* = 4a_0^*$, (e) $r^* = 6a_0^*$, (f) $r^* = 8a_0^*$ and (g) $r^* = 60a_0^*$.

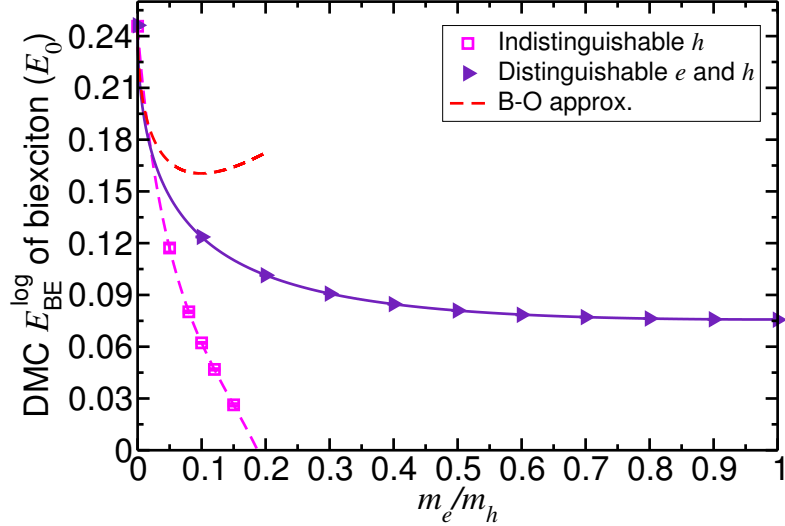


Figure 4.6: DMC BE of a biexciton with the logarithmic interaction against mass ratio m_e/m_h .

with distinguishable particles has the maximum value $0.24629(6)E_0$ at $m_e/m_h = 0$ and gradually falls to $0.0756(1)E_0$ at $m_e/m_h = 1$. However, the BE of biexcitons with indistinguishable holes falls to zero for $m_e/m_h < 0.2$, implying that they are unstable at large mass ratios in 2D TMDCs. The B–O approximation in Fig. 4.6 is obtained using Eq. 4.35, which is in excellent agreement with our DMC calculations in the limit of heavy holes.

In Fig. 4.7(a), we plot the BE of a biexciton with the 2D Keldysh interaction at different finite r^* , including the Coulomb interaction ($r^* = 0$). The BEs at $m_e/m_h = 0$ are obtained using the BE curves as a function of heavy-hole separation plotted in Fig. 4.7(b), where we fitted polynomial curves as a function of \sqrt{r} similar to Eq. 4.38 to our DMC data. The BE at $r^* = a_0^*$ is almost twice as large as that at $r^* = 2a_0^*$ and three times as large as that at $r^* = 4a_0^*$ while the BEs for $r^* > 4a_0^*$ are less than $0.09R_\infty^*$.

We have compared the stability of biexcitons with distinguishable particles and indistinguishable holes in the limit of Coulomb interaction (Fig. 4.8(a)) and $r^* = 8a_0$ (Fig. 4.8(b)). We find that biexcitons with identical holes are unstable, except for $m_e/m_h < 0.3$, while biexcitons consisting of distinguishable particles are stable

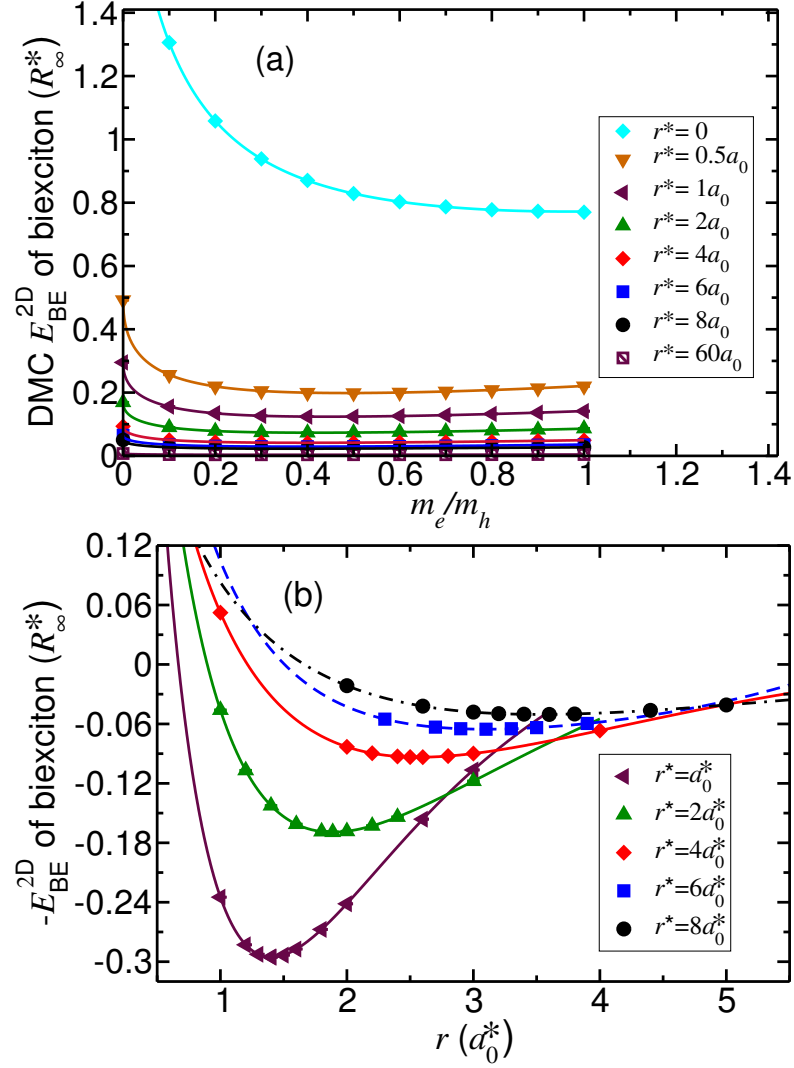


Figure 4.7: (a) DMC BE of biexciton with distinguishable particles against mass ratio m_e/m_h at finite r^* in the 2D Keldysh interaction, where the Coulomb interaction is denoted by $r^* = 0$. The DMC BE is defined by subtracting the total energy of the biexciton from twice of the total energy of the exciton (Eq. 4.22). r^* here are represented in terms of Bohr radius a_0 as defined in Eq. 4.25 (b) The minus DMC BE of heavy-hole biexciton with distinguishable particles against the hole separation for $r^* = 1, 2, 4, 6$ and $8a_0^*$. The BE is defined by subtracting twice of the total energy of the exciton from the total energy of the biexciton.

for different range of mass ratios. The B-O approximation in Fig. 4.8(b) for heavy holes is again in agreement with our DMC calculations.

The BE of biexcitons with distinguishable particles interacting via the Keldysh interactions are plotted in Fig. 4.9 using a polynomial fitting function as a function

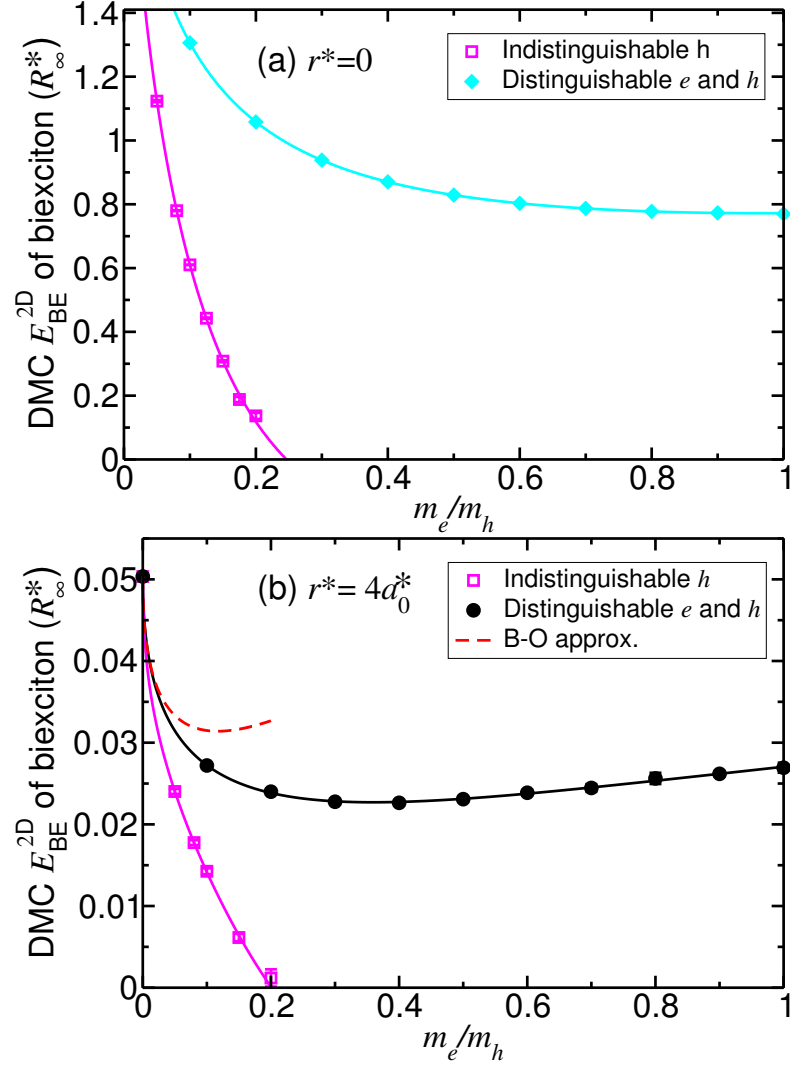


Figure 4.8: Comparison of DMC BE of biexcitons with both distinguishable electrons and holes and biexcitons with indistinguishable holes against mass ratio m_e/m_h with the 2D Keldysh interaction at (a) $r^* = 0$ and (b) $r^* = 4a_0^*$.

of $\sqrt{r^*/(1+r^*)}$ to the fifth order. Our results are in agreement with PIMC data at finite r^* [126]. However, the PIMC data obtained by Velizhanin and Saxena present much larger statistical errors and they quoted a previous DMC result at $r^* = 0$ [135] due to the infeasibility of PIMC.

Fig. 4.10 shows the DMC BEs for biexcitons with distinguishable particles interacting via the 2D Keldysh interaction as a function of mass ratio $y = m_e/m_h/(1 +$

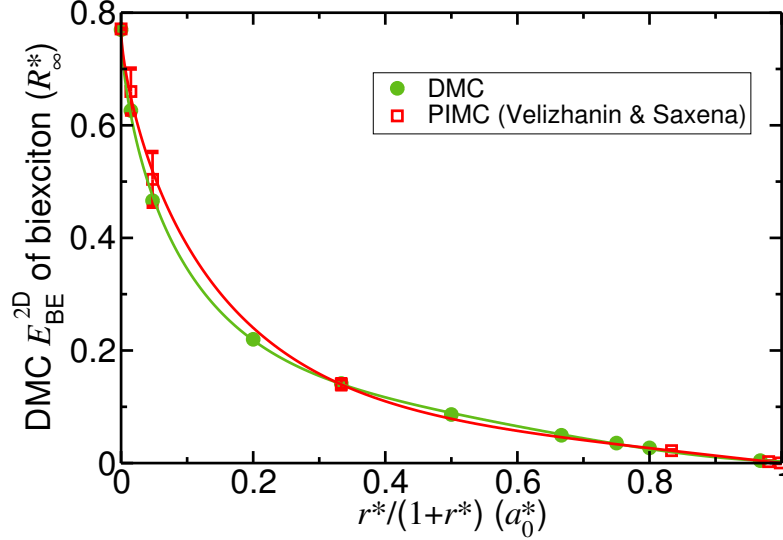


Figure 4.9: Comparing the BE of biexcitons with distinguishable electrons and holes in the 2D Keldysh interaction obtained by DMC and PIMC [126] methods at mass ratio 1.

m_e/m_h) and $x = \tilde{r}^*/(1 + \tilde{r}^*)$, where $\tilde{r}^* = r^*/a_0^*$. The fitting function was

$$E_{BE} = \sum_{i=0}^8 \sum_{j=0}^{8-i} B_{ij} x^i \sqrt{y}^j, \quad (4.39)$$

containing 43 fitting parameters B_{ij} with a quite large $\chi^2 = 651.042$ because some error bars are smaller than 10^{-2} meV.

Our DMC results show that the BEs of 2D TMDCs only dependent weakly on the mass ratios as can be seen in Table 4.4. DMC BEs are in good agreement with PIMC BEs [129] and to a lesser extent the previous DMC study [128]; however the latter work used an approximation to the 2D Keldysh interaction, which is not correct at finite r^* . Despite the agreement between our DMC BEs of biexcitons and the previous theoretical works, our results are up to three times smaller than experiment. DMC method is exact for biexcitons of distinguishable particles. Table 4.4 shows that different mass ratios and r^* give BE in the range of 15 – 26 meV, therefore it is unlikely that uncertainty in these parameters cause such a large disagreement with experiment. There is a possibility that there are misclassifications of donor-bound biexcitons in the experiment, which needs more

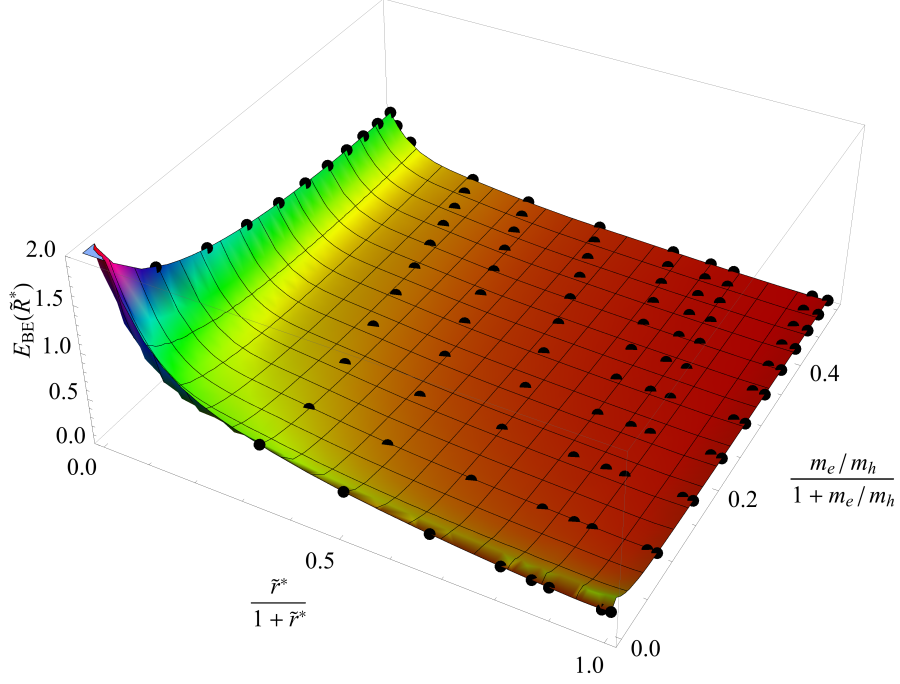


Figure 4.10: DMC BE of biexcitons with distinguishable particles against $\frac{m_e/m_h}{1+m_e/m_h}$ and $\tilde{r}^*/(1+\tilde{r}^*)$, in which $\tilde{r}^* = r^*/a_0^*$. The DMC BE unit is $\tilde{R}^* = e^2/(4\pi\epsilon_0(r^* + 2a_0^*))$.

investigations.

Table 4.4: BEs of biexcitons with distinguishable particles for different monolayer transition-metal dichalcogenides using DFT m_e , m_h and r^* reported in Ref. [129]. The first and second rows in BE (\tilde{R}^*) and DMC BE (meV) are calculated using the values in the first and second rows of mass ratio, respectively. Where a citation is not given in the table, the data were obtained in the present work.

Material	MoS ₂	MoSe ₂	MoTe ₂	WS ₂	WSe ₂	WTe ₂
r^* (Å) [129]	44.7	53.2	73.6	40.2	47.6	53.9
m_e/m_h [129]	0.77	0.80	0.92	0.91	0.94	0.40
	0.87	0.93	0.76	0.65	0.64	
DMC BE (\tilde{R}^*)	0.074	0.074	0.074	0.073	0.073	0.082
	0.073	0.073	0.074	0.074	0.075	
DMC BE (meV)	23.1	19.6	14.2	25.3	21.6	21.4
	23.0	19.4	14.4	26.0	22.2	
DMC BE (meV) [128]	22.7(3)	17.7(3)		23.3(3)	20.2(3)	
PIMC BE (meV) [129]	22.7(5)	19.3(5)	14.4(4)	23.9(5)	20.7(5)	
Exp. BE (meV)	60 [125]			65 [124]	52 [123]	
	70 [121]					

4.8 Conclusion

The formation of 2D biexcitons within the Keldysh interactions are calculated for different mass ratios and nonlocal screening lengths. Biexcitons consisting of distinguishable particles are always stable while indistinguishable electrons or holes make biexcitons stable close to the heavy electron or heavy hole regions, respectively. The DMC BEs of biexcitons containing distinguishable particles are exact and are obtained to be 15 – 26 meV for different monolayer TMDCs, whose screening lengths are 40 – 70 Å and a variety of mass ratios 0.4 – 0.9. Despite the agreement between our results and other theoretical studies, the BEs are around three times less than that reported by experiment. This discrepancy may be caused by the misclassifications of other possible charge complexes such as trion bound exciton in the experiment and needs more investigations.

Quasiparticle and excitonic gaps of one-dimensional carbon chains

5.1 Introduction

Carbon is the fourth most abundant element in the universe and is fundamental to life as we know it. Carbon exists in a number of strikingly different forms, including famous examples such as sp^3 -bonded diamond and two-dimensional sp^2 -bonded graphene. A less well-known form of pure carbon is polyynes, which is a one-dimensional sp -bonded chain of carbon atoms with alternating single and triple bonds. The observed presence of carbon chains in interstellar space and circumstellar shells [136, 137] has inspired considerable effort to synthesise polyynes in the laboratory, leading among other things to the discovery of fullerenes [138]. Recent experiments have shown that it is possible to produce a long linear chain of more than 200 carbon atoms inside a protector such as a double-walled carbon nanotube (DWCNT) [139] and also to synthesise stable oligoynes (short polyyne molecules) with up to 44 carbon atoms [140] and a variety of terminal groups [141–147]. Polyyne is of particular interest as the ideal interconnect in single-molecule nanoelectronic circuitry, including spintronic devices [148–151], and has potential

applications in nanomechanical devices [152–154]. Unfortunately, the characterization of the optical and electronic properties of polyynes continues to present many challenges. Our aim in this work is to address the source of experimental and theoretical discrepancies by establishing the structural and electronic properties of polyynes with quantitative accuracy.

The band gap of polyynes is strongly dependent on the bond-length alternation (BLA) that arises from the so-called Peierls distortion of the linear carbon chain [155]. A carbon chain has a half-filled band structure with degenerate π orbitals; therefore a small distortion can reduce the translational symmetry and introduce gaps into the energy bands at or near the Fermi energy, thereby lowering the total energy. Estimating the gap of extended polyynes by extrapolating from the measured absorption spectra of oligoynes has been attempted in several studies [140, 142, 145, 146, 156–158]; however, long oligoynes are needed to minimise the effects of terminal groups, and the interpretation of the absorption spectra of oligoynes is not always straightforward. Most first-principles studies of the electronic structure of polyynes to date are based on DFT with different exchange–correlation functionals [159–163]. The local LDA and PBE functionals substantially underestimate the gap. Hybrid exchange–correlation functionals such as the B3LYP [15, 16] and HSE06 [17, 18] functionals, which include a fraction of exact exchange, perform significantly better, but the predicted gaps still underestimate the range of gaps indicated by experiment [140, 142, 145, 146, 156–158, 164]. On the other hand, HF theory significantly overestimates gaps. Post-HF quantum-chemistry methods such as Møller–Plesset second-order perturbation theory (MP2) and coupled-cluster singles and doubles with perturbative triples [CCSD(T)] offer a different and potentially far more accurate theoretical approach [165]; however the gap of polyynes has to be obtained by extrapolating the gaps of small, hydrogen-terminated oligoynes to infinite chain length, introducing significant uncertainty into the results. Previous theoretical studies have reported the BLA of polyynes based on HF [160, 165], nonhybrid DFT [160, 165], hybrid DFT [160],

MP2 [160, 165, 166], and CCSD(T) [165, 167] calculations. However, there is no consensus over either the BLA or the band gap of polyynes in the literature [168, 169].

In this chapter, we use highly accurate QMC methods [22, 71] to calculate ground-state and excited-state total energies of isolated hydrogen-terminated oligoynes ($C_{2n}H_2$) and supercells of polyynes subject to periodic boundary conditions. The structure of polyynes is defined by just two parameters, the lattice constant and the BLA, enabling us to carry out a brute-force optimisation of the structure by minimising the QMC total energy. To the best of our knowledge this is the first QMC study of polyynes. We compare our data with experimental and theoretical results in the literature.

5.2 Computational methodology

5.2.1 DFT calculations

Our DFT calculations were performed using the CASTEP plane-wave-basis code [3]. We relaxed the geometries of hydrogen-terminated oligoynes consisting of up to twelve pairs of carbon atoms using DFT-PBE and DFT-HSE06, and we relaxed the geometry of extended polyynes using DFT-HSE06. The widths and heights of our periodic unit cells were fixed at 20 Bohr radii and, for oligoynes, the length was varied so that a constant amount of vacuum (20 Bohr radii) was maintained between images of the molecule. In our DFT calculations for polyynes we used a grid of 30 k points. We used ultrasoft pseudopotentials in our DFT-PBE calculations and norm-conserving pseudopotentials in our DFT-HSE06 calculations. The plane-wave cutoff energy in our DFT geometry optimisations was 25 Ha.

The DFT-PBE zero-point energy and the DFT-LDA and DFT-PBE phonon dis-

persion curves of polyynes were obtained using density functional perturbation theory in a primitive cell with 100 k points in the Brillouin zone for both the electronic calculation and the phonon calculation. The DFT-HSE06 zero-point energy and phonon dispersion curve of polyynes were calculated using 32 primitive-cell k points and the method of finite displacements in supercells of up to 16 primitive cells.

5.2.2 QMC calculations

For our QMC calculations we used the static-nucleus variational and diffusion quantum Monte Carlo (VMC and DMC) methods implemented in the CASINO code [21]. The DMC method has previously been used to study the excitation energies of a variety of molecules and solids [170–174]. The many-body trial wave function was composed of Slater determinants multiplied by a Jastrow correlation factor [22]. We used DFT-PBE orbitals, which were generated by CASTEP using a plane-wave cutoff energy of 120 Ha, and we used Dirac–Fock pseudopotentials [4, 73]. The plane-wave orbitals were re-represented in a blip (B-spline) basis before they were used in the QMC calculations [20], allowing the use of aperiodic (for oligynes) and 1D periodic (for polyynes) boundary conditions in our QMC calculations.

For each oligoyne the DFT highest occupied molecular orbital (HOMO) and HOMO–1 are degenerate, as are the lowest unoccupied molecular orbital (LUMO) and LUMO+1. We have therefore studied the effect of multideterminant (MD) Slater–Jastrow trial wave functions for excited, cationic, and anionic states of oligynes with 4, 6, 8, 10, and 24 carbon atoms as well as a supercell of polyynes composed of 8 primitive cells. The Slater determinants in the MD wave functions contained all the orbital occupancies that are degenerate at the single-particle level. In Table 5.1 we specify the occupancy of the orbitals in the determinants used in our trial wave functions.

We used linear-least-squares energy minimisation [28–30] and unweighted variance minimisation [26, 27] to optimise the MD coefficients and the Jastrow factor, respectively. Using variance minimisation rather than energy minimisation for the Jastrow factor improves the stability. A test for C_4H_2 showed that the effects of additional determinants containing promotions to the LUMO+2 are negligible.

Table 5.1: Number of MD terms and orbital occupancies in each determinant for the neutral ground state, singlet and triplet excited states, cationic and anionic states in each of our calculations. “H” and “L” denote the HOMO and LUMO, respectively. Note that the HOMO and HOMO−1 orbitals are degenerate, as are the LUMO and LUMO+1 orbitals. All orbitals up to HOMO−2 are occupied in each determinant.

State	No. determinants	Orbital occupancy							
		Spin-up				Spin-down			
		H−1	H	L	L+1	H−1	H	L	L+1
Neutral ground state	1	•	•			•	•		
Singlet excited state	8	•		•		•	•		
			•	•		•	•		
		•			•	•	•		
			•		•	•	•		
		•	•			•		•	
		•	•				•		•
		•	•				•		•
		•	•				•		•
Triplet excited state	4		•			•	•	•	
		•				•	•	•	
			•			•	•	•	
						•	•	•	
Cationic state	2	•				•	•		
			•			•	•		
Anionic state	2	•	•	•		•	•		
		•	•		•	•	•		

The free parameters in the Jastrow factor were optimised by unweighted variance minimisation [26, 27] and the determinant expansion coefficients were optimised by energy minimisation [28–30]. The DMC energy was linearly extrapolated to zero time step and we verified that finite-population errors in our results are negligible. Fermionic antisymmetry in DMC is imposed by the fixed-node approximation [35], in which the nodal surface is pinned at that of the trial wave function. The fixed-

node approximation allows us to study excited states by using trial wave functions with the same nodal topology as non-interacting electrons. Because the Jastrow factor is strictly positive, the nodal topology is purely determined by the Slater determinants.

Twist-averaging is less important in one-dimensional systems than two- or three-dimensional systems; for example momentum quantisation in a one-dimensional homogeneous electron gas simply introduces a smooth, $O(n^{-2})$ error in the energy per particle [175].

5.2.3 DMC quasiparticle and excitonic gaps

A crucial quantity that characterises the electronic structure of polyynes is the quasiparticle gap, which is the difference between the electron affinity and the first ionisation potential. The quasiparticle gap is the energy required to create an unbound electron–hole pair and was computed by the DMC method [22]. Quasiparticle gaps are evaluated as

$$\Delta_{\text{qp}} = E_{\text{I}} - E_{\text{A}} = E_{+} + E_{-} - 2E_0, \quad (5.1)$$

where $E_{\text{A}} = E_0 - E_{+}$ and $E_{\text{I}} = E_{-} - E_0$ are the electron affinity and ionisation potential, respectively. E_{+} and E_{-} are the total energies of the system with one more electron and one fewer electron, respectively, than the neutral ground state and E_0 is the ground-state total energy. For each oligoyne we separately relaxed the geometries of the neutral ground state, the cation, and the anion using DFT-HSE06 before evaluating the DMC ionisation potential and electron affinity and hence quasiparticle gap, i.e., we use the adiabatic definition of the quasiparticle gap. For polyynes, where there are just two structural parameters, we relaxed the ground-state geometry using DMC, and then used that geometry to obtain the vertical quasiparticle gap; it was verified that the difference between the vertical

and adiabatic quasiparticle gaps is small for large oligoynes (see Sec. 5.3.3).

Similarly, the excitonic gaps are evaluated as

$$\Delta_{\text{exc}} = E_{\text{pr}} - E_0, \quad (5.2)$$

where E_{pr} is the DMC total energy when a single electron is promoted from the valence-band maximum to the conduction-band minimum (without changing its spin for a singlet excitonic gap; swapping its spin for a triplet excitonic gap). In the ground-state geometry, the singlet excitonic gap is equivalent to the optical absorption gap, i.e., the energy at which the onset of photoabsorption occurs.

The excitonic gaps are smaller than the quasiparticle gap due to the attraction between the excited electron and the hole left in the valence band. The exciton binding energy is the difference between the quasiparticle and excitonic gaps. Fixed-node errors in the DMC total energies are positive and cancel to a significant extent when energy gaps are calculated.

5.2.4 Finite-size effects

The BLA of polyynes in the ground state was evaluated for three supercells consisting of 8, 12, and 16 primitive unit cells. To remove finite-size effects in the energy we fitted

$$E(n) = E(\infty) + An^{-2}, \quad (5.3)$$

where $E(\infty)$ and A are fitting parameters, to our DMC ground-state energies per primitive cell $E(n)$ in supercells of n primitive cells [175].

The DMC quasiparticle and excitonic gaps $\Delta(n)$ of polyynes were calculated for supercells of $n = 8, 10, 12,$ and 16 primitive cells, and then extrapolated to infinite

length by fitting

$$\Delta(n) = \Delta(\infty) + Bn^{-1} \quad (5.4)$$

to the data, where $\Delta(\infty)$ and B are fitting parameters. When a single particle is added to a finite simulation cell subject to periodic boundary conditions, a periodic lattice of quasiparticles is formed. The energy of this unwanted lattice of quasiparticles goes as the Madelung constant of the supercell lattice and results in a significant finite-size error in the electron affinity and ionisation potential. The one dimensional Madelung energy in Hartree atomic units is given by $v_M = [-0.2319 - 2\log(an)]/(an)$, where a is the lattice constant and n is the number of primitive cells. Ignoring logarithmic corrections in one-dimensional systems, the Madelung constant falls off as the reciprocal of the linear size of the supercell, i.e., as $1/n$. Additional finite-size effects in the exciton energy arise from the fact that the energy is evaluated using the Ewald interaction rather than $1/r$. However, by calculating the ground-state energy of an exciton modelled by a single electron and a single hole moving strictly in one dimension in a periodic cell as a function of cell length (Fig. 5.1), we find that these finite-size errors fall off more rapidly, as $1/n^3$. Equation (5.4) is therefore an appropriate fitting function for extrapolating gaps to the thermodynamic limit. The finite-size error in the quasiparticle gap is significantly larger than the finite-size error in the excitonic gap, because we do not change the number of electrons in the simulation cell when calculating the latter. The Madelung constant is negative, and hence the finite-size error in the quasiparticle gap is large and negative, resulting in a negative exciton binding energy at finite system size. Physically this is caused by the fact that, when a charged particle is added to or removed from a finite, periodic cell in which particles interact via the Ewald potential, a neutralising background is implicitly introduced. This neutralising background charge density vanishes in the infinite-system limit, and hence our quasiparticle gaps are only physically meaningful in the infinite-system limit. For a finite molecule, by contrast, the $1/r$ Coulomb interaction is used, and hence no additional neutralising background is introduced

when a charged particle is added to or removed from a neutral molecule.

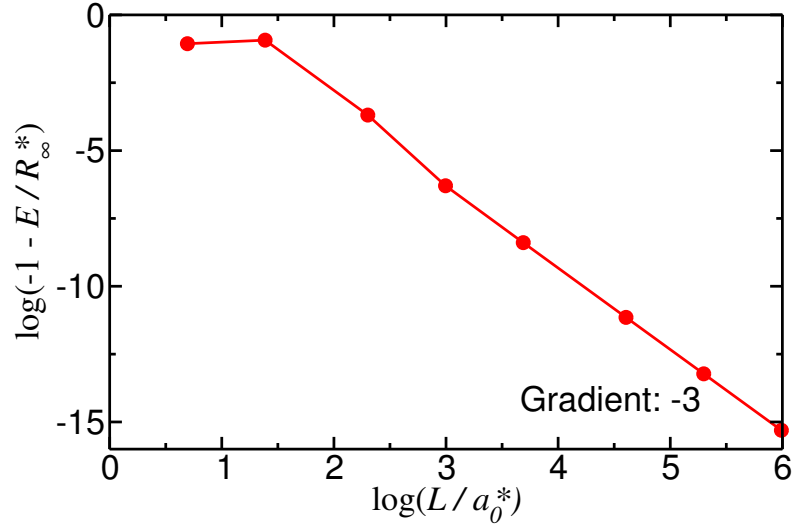


Figure 5.1: Finite-size error in the total energy of a one dimensional exciton against the periodic cell length $L = an$, where a is the lattice constant and n is the number of primitive cells. $R_\infty^* = \mu/2$ is the exciton Rydberg and $a_0^* = 1/\mu$ is the exciton Bohr radius. $\mu = m_e m_h / (m_e + m_h)$ is the reduced mass of the electron–hole pair.

5.2.5 Test of our method: benzene molecule

DMC has proven to be a highly accurate method for calculating excitation energies within the static-nucleus approximation [170–174]. For the case of diamondoids, the DMC excitonic gap was found to be 0.5 eV higher than the experimentally determined optical absorption gap [174, 176]. However the difference with experiment was subsequently shown to be caused by the vibrational renormalization of the gap [177].

As a brief test of our methodology, we have calculated the static-nucleus DMC ionisation potential and singlet and triplet optical-absorption (excitonic) gaps of a benzene molecule in vacuum. The geometry was relaxed in both the neutral ground state and the cationic state using DFT-PBE exchange–correlation functional. The resulting DMC ionisation potential is 9.24(2) eV, which is in excellent agreement with the experimental value of 9.24384(6) eV [178]. If the ground-state geometry

is used for both the ground state and the cation then the static-nucleus DMC ionisation potential is 9.39(3) eV. This illustrates that, when calculating ionisation potentials and electron affinities (and hence quasiparticle gaps) for small molecules, it can be important to relax the geometry in the neutral, cationic, and anionic states.

Static-nucleus DMC predicts the singlet and triplet excitonic gaps of benzene to be 5.63(4) and 4.56(4) eV, respectively, which may be compared with the experimental values of 4.9 eV [179] and 3.9 eV [180], respectively. The DFT vibrational renormalisation of the excitonic gap of benzene ranges from -0.45 eV to -0.50 eV, depending on the choice of exchange–correlation functional[181]. This correction enormously improves the agreement between theory and experiment, as observed in diamondoids [182]. This indicates that we can expect our DMC gaps to be accurate to within 0.2–0.3 eV.

5.3 Results and discussion

5.3.1 Atomic structures and atomisation energies of linear hydrogen-terminated oligoynes

The ground-state BLAs at the centres of oligoynes have previously been calculated using a variety of theoretical methods [162, 167, 183, 184]; some of the results are compared with our DMC and DFT data in Fig. 5.2. The PBE functional completely fails to describe the BLA for long chains, while spin-restricted HF theory predicts a very large BLA. Our DFT-HSE06 BLAs are in agreement with the values previously obtained using the B3LYP functional [162, 183], and are close to the MP2 results wherever the latter are available [184]. However, none of these BLA curves tends to the DMC BLA of polyynes as the chain length increases. By contrast, the CCSD(T) BLAs [167] of oligoynes appear to tend to a limit only

slightly less than the DMC result for polyyne. Our DMC results for the BLA of extended polyyne provide benchmark data with which the results of other theories may be compared.

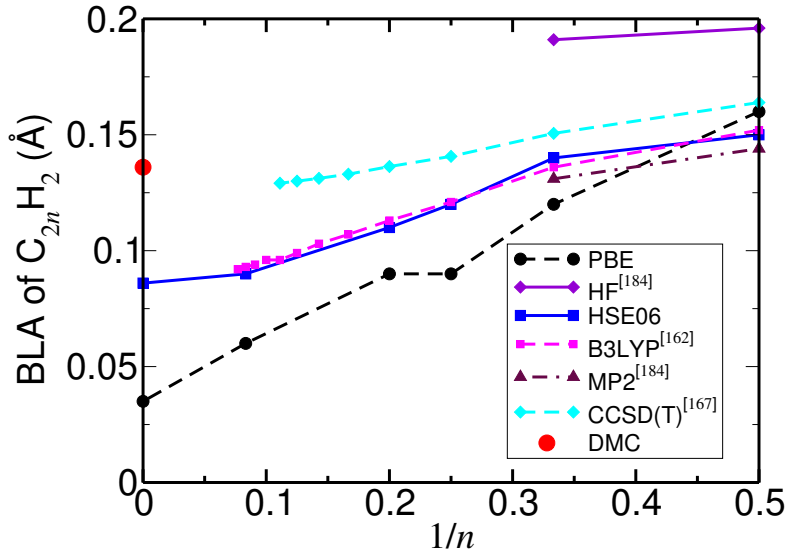


Figure 5.2: Optimised BLA at the centre of a hydrogen-terminated oligoyne in the ground state against the reciprocal of the number n of pairs of carbon atoms.

The DMC static-nucleus atomisation energy of the oligoyne $C_{2n}H_2$ is defined as $2n$ times the DMC total energy of an isolated, spin-polarised carbon atom plus two times the DMC total energy of an isolated hydrogen atom minus the DMC static-nucleus total energy of $C_{2n}H_2$. The DMC atomisation energies of oligoynes obtained using geometries relaxed in DFT-HSE06 and DFT-PBE calculations are compared in Fig. 5.3. For oligoynes consisting of up to five pairs of carbon atoms, the difference between the DMC atomisation energies with the DFT-PBE and DFT-HSE06 geometries is negligible.

5.3.2 Atomic structure and atomisation energy of polyyne

As the number of carbon atoms goes to infinity, the effects of the terminal groups become negligible; therefore polyyne can be considered to be a one-dimensional

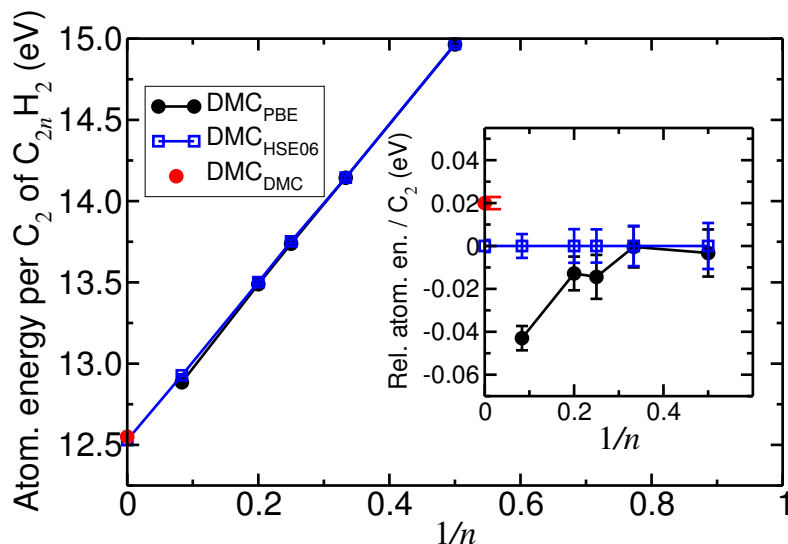


Figure 5.3: Static-nucleus DMC atomisation energies of hydrogen-terminated oligynes as a function of the reciprocal of the number n of pairs of carbon atoms. “DMC_X” indicates a DMC atomisation energy calculated using the geometry optimised by method X. The inset shows the relative atomisation energies of hydrogen-terminated oligynes as a function of the reciprocal of the number n of pairs of carbon atoms.

periodic chain with a primitive cell composed of two carbon atoms with alternating triple and single bonds.

In order to obtain the BLA of an infinite chain, we considered supercells subject to periodic boundary conditions, in which the lattice constant was fixed at the DFT-BLYP [160] value of 2.58 Å. We calculated DMC energies at different BLAs ranging between 0.09 and 0.18 Å and fitted a quadratic to our DMC data, as shown in Fig. 5.4(a), to locate the minimum.

The DMC energy minima of supercells consisting of 8, 12, and 16 primitive cells are at BLAs of 0.152(5), 0.145(2), and 0.144(1) Å, respectively. When the BLA is 0.15 Å, the C≡C triple-bond length is 1.215 Å and the ratio of the C≡C triple-bond length to the lattice constant is 0.471. We then computed the ground-state DMC energy of polyynes at several lattice constants, from 2.4 to 2.7 Å, holding the ratio of the C≡C bond length to the lattice constant at 0.471 for the supercell composed of 8 primitive cells and holding the C≡C bond length at 1.215 Å for

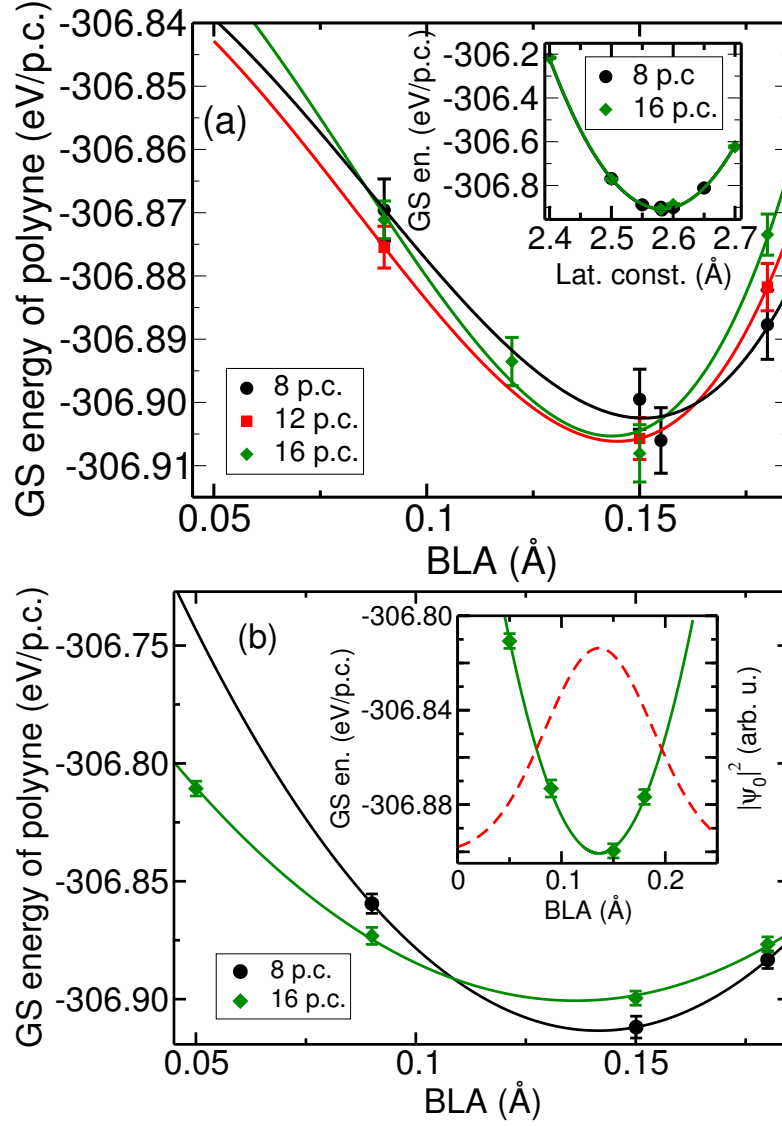


Figure 5.4: (a) Ground-state (GS) DMC energy of polyyne as a function of BLA for lattice constant 2.58 \AA in different sizes of simulation supercell. The inset shows the ground-state DMC energy of polyyne against the lattice constant at a fixed ratio of $\text{C}\equiv\text{C}$ bond length to lattice constant for 8 primitive cells (p.c.) and a fixed $\text{C}\equiv\text{C}$ bond length for 16 p.c.s. (b) GS DMC energy of polyyne as a function of BLA for lattice constant 2.5817 \AA in different sizes of supercell. The minimum of the DMC energy, $-306.901(3) \text{ eV}$ per p.c.s, is at $\text{BLA } b_0 = 0.136(2) \text{ \AA}$. The inset shows the square modulus $|\psi_0|^2$ of the longitudinal optical phonon ground-state wave function for a supercell composed of 16 p.c.s as a function of BLA.

the supercell consisting of 16 primitive cells. The quadratic fits to the DMC data in the inset of Fig. 5.4(a) are in good agreement, and the ground-state energy is minimised at lattice constants of $2.5817(9) \text{ \AA}$ and $2.5822(5) \text{ \AA}$ for supercells of

8 and 16 primitive cells, respectively. Finally, the DMC energy was calculated at lattice constant 2.5817 Å for different BLAs as shown in Fig. 5.4(b) together with quadratic fits. The DMC energy minima for supercells consisting of 8 and 16 primitive cells occur at BLAs of 0.142(2) and 0.136(2) Å, respectively, which are in reasonable agreement. Furthermore, the BLA obtained in a supercell of 16 primitive cells does not differ significantly from the BLA 0.133(2) Å obtained by minimising the DMC energy extrapolated to infinite system size using Eq. (5.3). We therefore report the BLA obtained in a supercell of 16 primitive cells [0.136(2) Å] as our final result.

The DMC data shown in Fig. 5.4 for the ground-state energy per primitive cell $e(b)$ against BLA b can be used to calculate the longitudinal optical (LO) phonon frequency of polyyne at Γ . Near the minimum of the energy we may write

$$e(b) = e_0 + \frac{1}{2} \frac{m_C}{2} \omega^2 \left(\frac{b}{2} - \frac{b_0}{2} \right)^2, \quad (5.5)$$

where b is the bond-length alternation, b_0 and e_0 are constants, $m_C/2$ is the reduced mass of the two carbon atoms in polyyne's primitive unit cell, and ω is the LO phonon frequency at Γ . In terms of the BLA b , the ground-state wave function of the zone-center LO phonon mode of polyyne in Hartree atomic units is

$$\psi_0(b) = \left(\frac{m_C \omega}{2\pi} \right)^{1/4} \exp \left[-\frac{m_C \omega}{2} \left(\frac{b}{2} - \frac{b_0}{2} \right)^2 \right]. \quad (5.6)$$

Fitting Eq. (5.5) to the static-nucleus DMC energy of a supercell composed of 16 primitive cells of polyyne gives $\omega = 2084(5) \text{ cm}^{-1}$. The standard deviation of b in the ground state is $\sigma_b = \sqrt{2/(m_C \omega)} = 0.052 \text{ Å}$. The square modulus of the LO phonon ground-state wave function is plotted in the inset of Fig. 5.4(b).

In Fig. 5.5 we show the DFT-LDA, DFT-PBE, and DFT-HSE06 phonon dispersion curves of polyyne. Our DFT-PBE phonon dispersion curve is in good agreement with previous DFT-PBE results in the literature [185]. By calculating the DMC

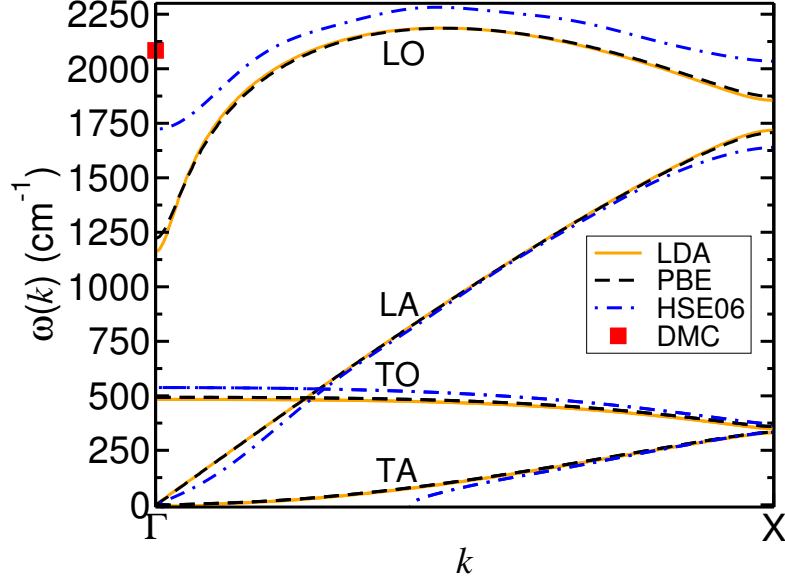


Figure 5.5: Phonon dispersion curve of polyynes calculated using DFT-LDA, DFT-PBE, and DFT-HSE06. The DMC LO frequency at Γ is shown by the red square. “T,” “L,” “A,” and “O” stand for transverse, longitudinal, acoustic, and optical, respectively. We believe the slight instability of the TA branch in the DFT-HSE06 dispersion curve is a numerical artifact.

energy as a function of BLA, we have determined the DMC longitudinal optical (LO) phonon frequency at Γ , which we find to be $2084(5) \text{ cm}^{-1}$. This is significantly higher than the frequencies of 1162, 1223, 1723, and 1844 cm^{-1} obtained using DFT-LDA, DFT-PBE, DFT-HSE06, and DFT-B3LYP [186], respectively. It is clear that DFT provides a poor description of both the Peierls distortion and the related LO phonon behaviour. The LO phonon frequencies of oligynes with up to 40 carbon atoms have been measured by Raman spectroscopy to be in the region of $1900\text{--}2300 \text{ cm}^{-1}$; the precise value depends on the terminal groups, solvent, and the number of carbon atoms in the chain [187].

To evaluate the quasiparticle gap of polyynes, the atomic structure should be in principle be relaxed when an electron is added to or removed from a supercell. Although the effect on the structure becomes vanishingly small as the supercell becomes large [falling off as $O(n^{-1})$, where n is the number of primitive cells in the supercell], the effect on the gap remains finite, because the gap is a difference of total energies, which increase as $O(n)$ with supercell size and depend on the

atomic structure. However, the re-optimisation of the geometry at each system size adds noise that affects the extrapolation to the limit of infinite system size and, as shown in Fig. 5.8, the effect of relaxing the geometries of cations and anions on the quasiparticle gap (i.e., the difference between the vertical and adiabatic quasiparticle gaps) is small for large oligoynes.

In Table 5.2 we compare the equilibrium BLAs and lattice constants of polyynes obtained using different methods. DFT-LDA, PBE, and HSE06 functionals underestimate the BLA of polyynes, while HF theory predicts a larger BLA than DMC. The DMC BLA happens to be in agreement with the Becke-half-and-half-Lee-Yang-Parr (BHHLYP) and Kang-Musgrave-Lee-Yang-Parr (KMLYP) results [160]. The BLA of extended polyynes within a DWCNT has been measured to be 0.1 Å [139], which we expect to be different from our results for free-standing polyynes due to the effects of charge transfer between the polyynes and the DWCNT.

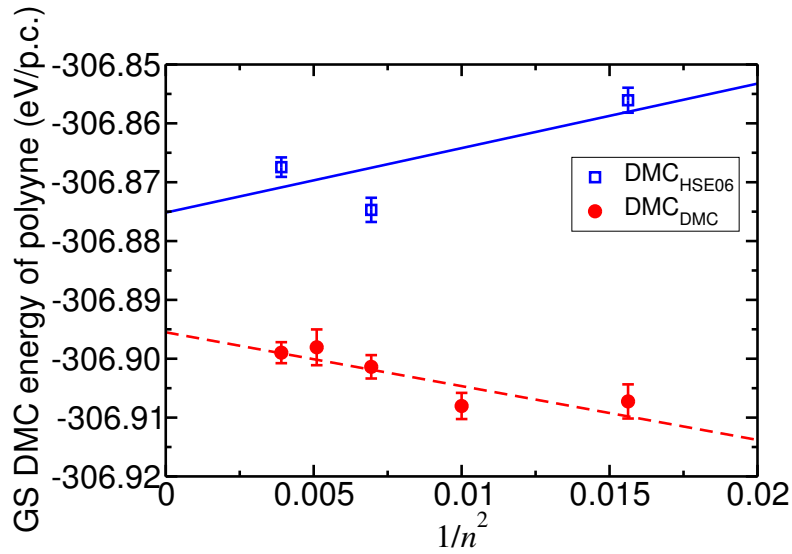


Figure 5.6: Ground-state (GS) DMC energy of polyynes against the reciprocal of the square of the number n of primitive cells (p.c.) in the supercell. “DMC_X” indicates a DMC energy calculated using the geometry optimized by method X.

In Figure 5.6 we compare the ground-state DMC energy of polyynes calculated using BLAs obtained by DMC and DFT-HSE06 as a function of system size. To reduce

Table 5.2: BLA and lattice constant a of polyynes as calculated or measured by different methods. r_1 and r_2 are the C–C and C≡C bond lengths, respectively. “PBC” indicates that periodic boundary conditions were used; otherwise results were obtained by extrapolation from a series of oligoynes. Where known, the number n of pairs of carbon atoms in the longest chain for which calculations were performed is given. Where a citation is not given in the table, the data were obtained in the present work. The experimental result is for polyynes encapsulated in a DWCNT.

Method	n	a (Å)	r_1 (Å)	r_2 (Å)	BLA (Å)
DFT-LDA [160]	PBC	2.566	1.297	1.269	0.028
DFT-LDA [165]	PBC	2.532	1.286	1.246	0.040
DFT-PBE	PBC	2.565	1.300	1.265	0.035
DFT-PBE1PBE [160]	36				0.093
DFT-HSE06	PBC	2.56	1.323	1.237	0.086
DFT-KMLYP [160]	36				0.135
DFT-BHHLYP [160]	36				0.134
DFT-B3LYP [160]	36				0.088
DFT-O3LYP [160]	36				0.067
DFT-BLYP [160]	PBC	2.582	1.309	1.273	0.036
HF [160]	36				0.183
MP2 [160]	20				0.060
MP2 [165]		2.554	1.337	1.217	0.120
MP2/CO [166]		2.6	1.346	1.254	0.092
CCSD [165]		2.559	1.362	1.197	0.165
CCSD(T) [165]		2.565	1.358	1.207	0.151
CCSD(T) [167]	9	2.586	1.357	1.229	0.128
DMC	PBC	2.5817(9)	1.359(2)	1.223(2)	0.136(2)
Exp. in DWCNT [139]	~ 200	2.558	1.329	1.229	0.100

finite-size errors, we considered supercells consisting of 8, 12, and 16 primitive cells, with the BLA and lattice constant fixed as a function of cell size, and we fitted a curve of the form Eq. 5.3. The extrapolated DMC energies with the DFT-HSE06 and DMC geometries are $-306.875(2)$ and $-306.895(2)$ eV per primitive cell, respectively, confirming that DMC is needed for geometry optimisation.

DMC atomisation energies of extended polyynes obtained using DMC and DFT-HSE06 geometries are compared in Table 5.3. The DMC static-nucleus atomisation energy with the DMC geometry is $12.55(1)$ eV, which is outside the range 10.7–11.4 eV estimated by MP2, CCSD, and CCSD(T) methods in Ref. 165; however the

latter were calculated by extrapolating results obtained for hydrogen-terminated oligoynes of up to eight pairs of carbon atoms to infinite chain length, whereas our polyynes calculations use periodic boundary conditions. DFT phonon zero-point energies are reported in the caption of Table 5.3. As shown in Fig. 5.3, the difference between DMC atomisation energies with DFT-PBE and DFT-HSE06 geometries is negligible for small oligoynes.

Table 5.3: Static-nucleus atomisation energy E_c of polyynes as obtained by different methods. “DMC_{DMC}” and “DMC_{HSE06}” indicate that the DMC energy of polyynes was calculated using the DMC- and DFT-HSE06-optimised geometries, respectively. (The DFT-PBE and DFT-HSE06 phonon zero-point energies of polyynes are 0.260 and 0.264 eV per primitive cell (p.c.), respectively. The zero-point energy is a correction that should be subtracted from the atomisation energy before comparison with experiment.)

Method	E_c (eV/p.c.)
DFT-PBE	13.71
DFT-HSE06	12.47
MP2 [165]	11.375
CCSD [165]	10.678
CCSD(T) [165]	11.053
DMC _{HSE06}	12.53(1)
DMC _{DMC}	12.55(1)

5.3.3 Quasiparticle and excitonic gaps of hydrogen-terminated oligoynes

Figure 5.7(a) shows that using a MD trial wave function reduces the DMC singlet and triplet excitonic gaps of small oligoynes (by up to 1.3 eV for C₄H₂). The reduction in singlet gaps is larger than the reduction in triplet gaps. However, Fig. 5.7(b) shows that using a MD wave function does not significantly affect the quasiparticle gaps of oligoynes. As the length of the molecule increases, the effects of using multiple determinants on the excitonic gaps decreases, becoming negligible for polyynes.

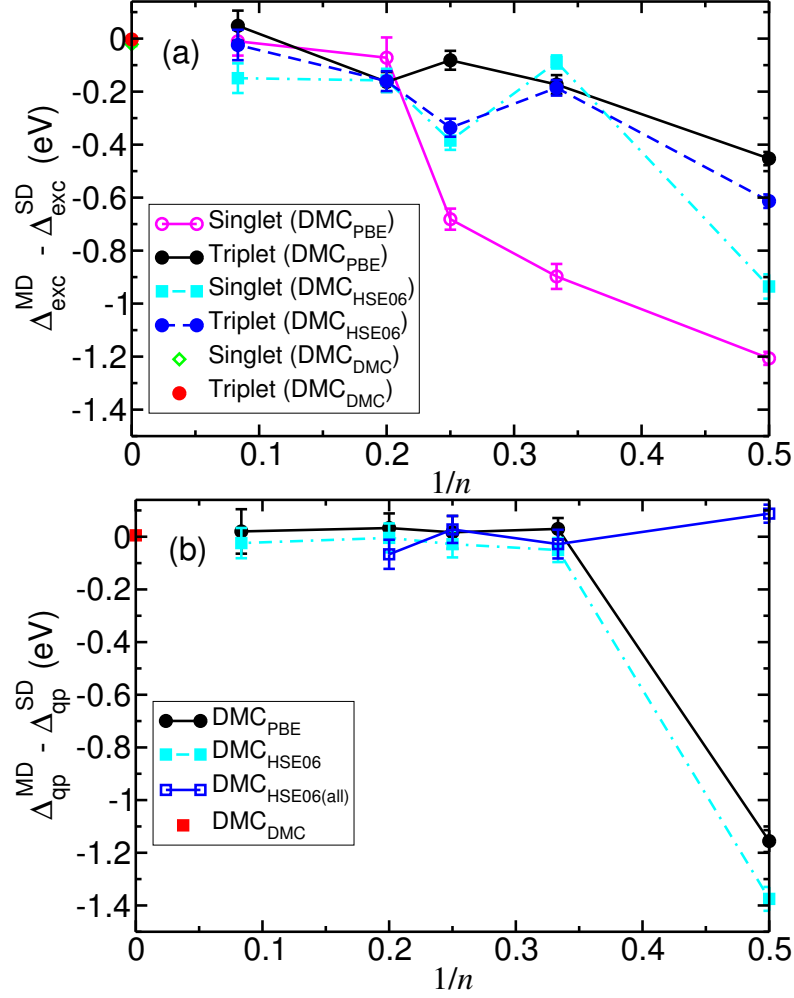


Figure 5.7: (a) Difference ($\Delta_{\text{exc}}^{\text{MD}} - \Delta_{\text{exc}}^{\text{SD}}$) of the DMC excitonic gaps of oligynes obtained using MD and single-determinant Slater–Jastrow trial wave functions as a function of the reciprocal of the number n of pairs of carbon atoms. (b) Difference ($\Delta_{\text{qp}}^{\text{MD}} - \Delta_{\text{qp}}^{\text{SD}}$) of the DMC quasiparticle gaps of oligynes obtained using MD and single-determinant Slater–Jastrow trial wave functions as a function of the reciprocal of the number n of pairs of carbon atoms. DMC_X indicates a DMC gap calculated using the geometry optimised by method X. “X(all)” in the subscript indicates the use of geometries separately optimised using method X for the neutral ground state, cationic state, and anionic state.

The DMC quasiparticle gaps of oligynes are compared with other theoretical results in Fig. 5.8. The HF method overestimates the quasiparticle gap, while DFT with various functionals considerably underestimates the gap. The DMC quasiparticle gaps calculated using DFT-HSE06 and DFT-PBE geometries are in agreement for oligynes consisting of fewer than ten carbon atoms, but gradually start to differ from each other for longer oligynes, with the difference in the DMC

gaps reaching 0.8(1) eV for $C_{24}H_2$. This demonstrates that, not only the method used to calculate the gap, but also the method used to optimise the geometry of polyynes must be highly accurate. Using the ground-state geometry rather than separately optimised geometries for the ground, cationic, and anionic states increases the quasiparticle gap by less than 0.15 eV for oligynes longer than C_8H_2 . The DMC quasiparticle gap of polyynes, evaluated using DMC geometries, is 3.6(1) eV.

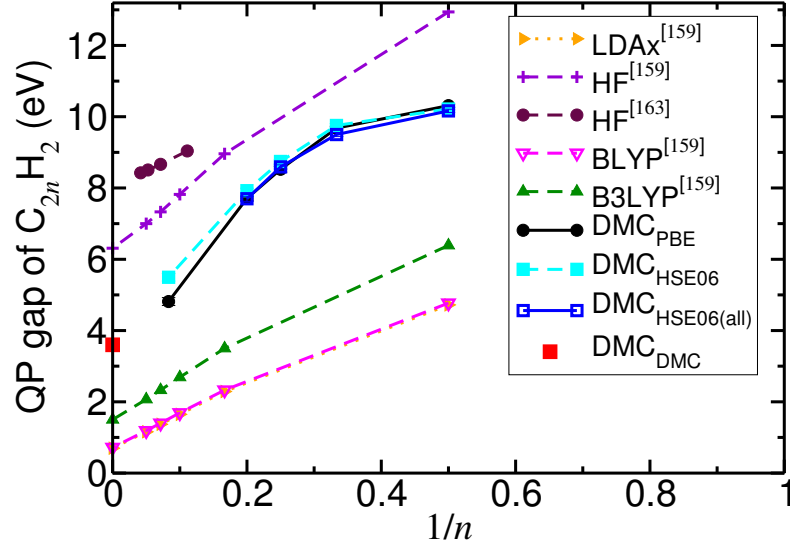


Figure 5.8: Static-nucleus quasiparticle (QP) gaps of hydrogen-terminated oligynes against the reciprocal of the number n of pairs of carbon atoms. “ DMC_{PBE} ” and “ DMC_{HSE06} ” denote DMC gaps calculated using DFT-PBE and DFT-HSE06 ground-state geometries, respectively. “ $DMC_{X(all)}$ ” denotes DMC quasiparticle gaps calculated using geometries optimised by method X separately for the neutral ground state, cationic state, and anionic state.

We plot the singlet and triplet excitonic gaps of different oligynes in Fig. 5.9. Singlet–triplet splitting (the difference of singlet and triplet excitonic gaps) against the reciprocal of the number n of pairs of carbon atoms in oligynes is small about 0.1–0.2 eV as shown in Fig. 5.10. Using DFT-HSE06 geometries instead of DFT-PBE geometries typically increases the DMC gaps by around 0.2 eV for small oligynes.

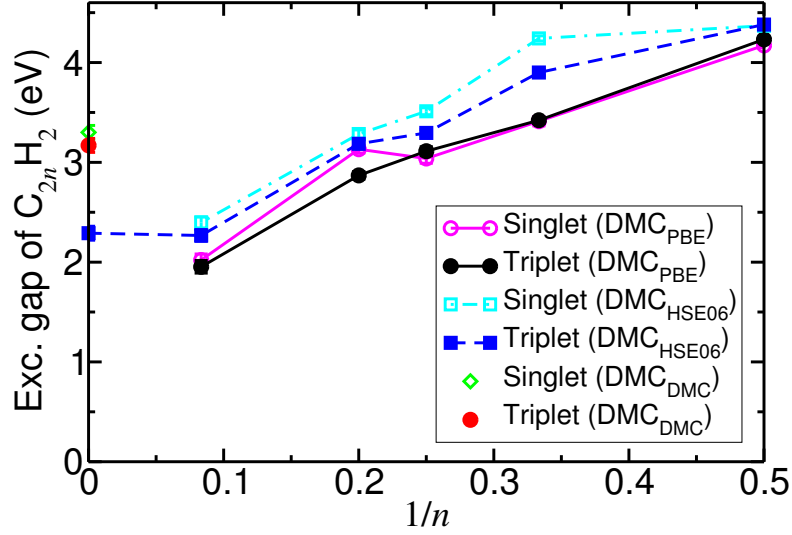


Figure 5.9: DMC static-nucleus singlet and triplet excitonic gaps for oligoynes, whose geometries are optimised by DFT-PBE and DFT-HSE06, against the reciprocal of the number n of pairs of carbon atoms. DMC_X indicates a DMC gap calculated using the geometry optimised by method X.

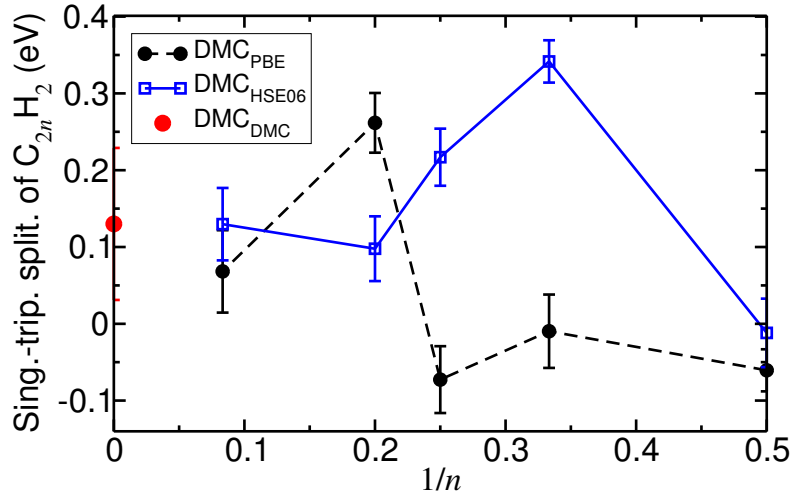


Figure 5.10: DMC singlet-triplet splitting for oligoynes obtained with DFT-PBE and DFT-HSE06 geometries. The polyne limit was obtained using the DMC geometry.

5.3.4 Quasiparticle and excitonic gaps of polyne

Figure 5.11(a) shows the finite-size behaviour of the DMC static-nucleus triplet excitonic gaps of polyne obtained using the DFT-HSE06 and DMC ground-state geometries. In the infinite-system limit, the DMC triplet gaps with the DFT-HSE06 and DMC geometries are 2.29(7) and 3.17(7) eV, respectively. Figure 5.11(b) shows

the static-nucleus triplet and singlet excitonic gaps and the quasiparticle gap of polyynes calculated using the Ewald interaction and the DMC-optimised geometry in different supercells, together with DFT-PBE gaps. The singlet excitonic gap of polyynes is slightly larger than the triplet gap. The DFT-PBE quasiparticle and excitonic gaps are calculated using the DMC-optimised geometry and Eqs. (5.1) and (5.2) at different k -point samplings (which may be unfolded to correspond to supercells of n primitive cells). The triplet excitonic gap calculated by DFT is relatively close to the DMC triplet excitonic gap, while the DFT quasiparticle gap is far too large. The DFT gap predicted by the ground-state band-structure calculation is (as expected) significantly underestimated. The fluctuations in the DFT gaps as a function of supercell size (i.e., k -point grid) are small, suggesting that single-particle errors in the DMC gaps are negligible. However, it is clear that there is a systematically varying finite-size error in the DMC gap. We have reduced the systematic finite-size errors in our DMC gaps by calculating both excitonic and quasiparticle gaps for supercells composed of 8, 10, 12, and 16 primitive cells and then extrapolating to infinite cell size using Eq. (5.4). The finite-size errors in the quasiparticle gaps are larger than the finite-size errors in the excitonic gaps, as discussed in Sec. 5.2.4. The DMC singlet and triplet excitonic gaps of polyynes calculated using the DMC-relaxed geometry are 3.30(7) and 3.17(7) eV, respectively, while the DMC quasiparticle gap is 3.6(1) eV.

To estimate the unscreened exciton binding energy within the Wannier–Mott model, we have calculated the DFT-HSE06 band structure of polyynes (shown in Fig. 5.12). In Hartree atomic units the band effective masses m_e^* and m_h^* of the electrons and holes at the X point of the Brillouin zone are given by

$$m_{e(h)}^* = \left| \frac{1}{(d^2\mathcal{E}_{C(V)}/dk^2)_X} \right|, \quad (5.7)$$

where $\mathcal{E}_C(k)$ and $\mathcal{E}_V(k)$ are the conduction and valence bands, respectively. Numerically differentiating the DFT-HSE06 bands, we find that $m_e^* = 0.046$ a.u. and

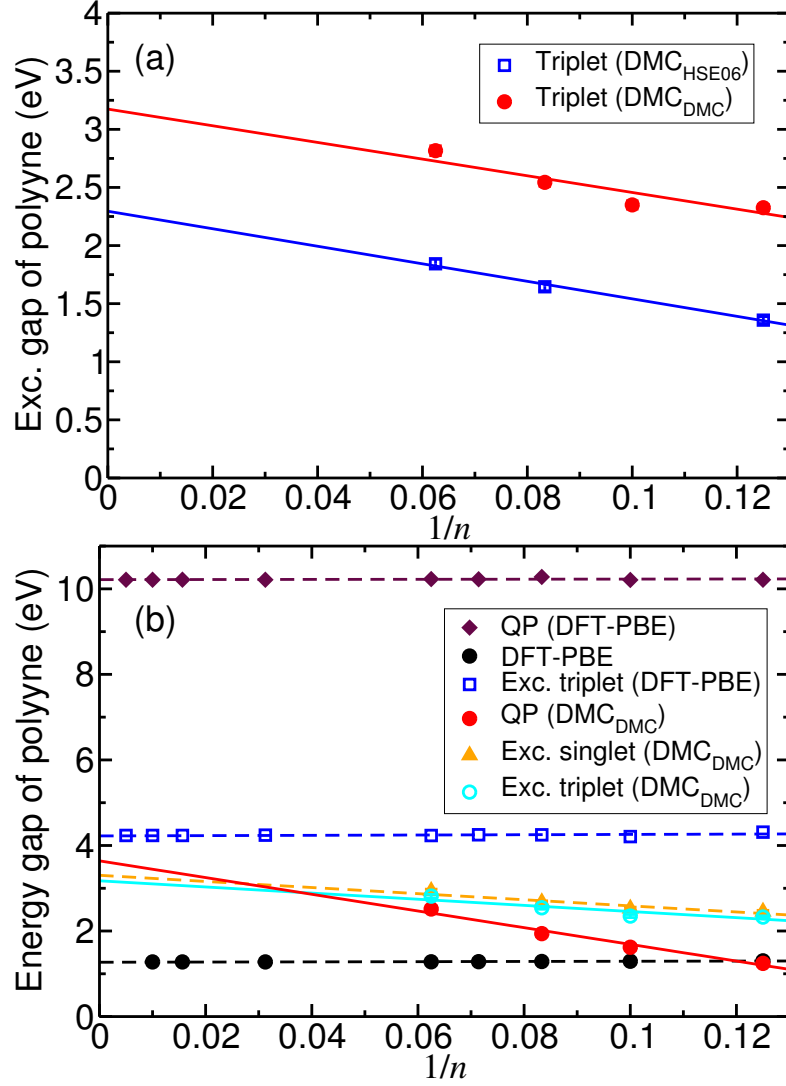


Figure 5.11: (a) DMC excitonic gaps of polyynes against the reciprocal of the number n of primitive cells in the supercell as calculated using the DFT-HSE06 and the DMC ground-state geometries (DMC_{HSE06} and DMC_{DMC}, respectively). (b) Quasiparticle (QP) and excitonic energy gaps of polyynes against the reciprocal of the number n of primitive cells in the supercell as obtained using different methods. The results simply labelled “DFT-PBE” show the band gap obtained in a ground-state band-structure calculation. The results labelled DMC_{DMC} used the DMC ground-state geometry. The DFT calculations used the DMC geometries in the same way as the DMC calculations. At finite size the quasiparticle gap is smaller than the excitonic gap due to the introduction of a neutralising background when a charged particle is added to or removed from a periodic cell, as explained in Sec. 5.2.4.

$m_h^* = 0.050$ a.u. In Hartree atomic units the exciton Bohr radius is $a_0^* = 1/\mu^*$, where $\mu^* = m_e^* m_h^* / (m_e^* + m_h^*)$ is the reduced mass of the electron-hole pair and

we have assumed that the electron and hole interact via the unscreened Coulomb interaction. In this case, the exciton Bohr radius is $a_0^* = 22 \text{ \AA}$, which is slightly smaller than the exciton Bohr radii of about 30 \AA estimated for various other 1D conjugated polymers [188], and is similar to or smaller than the lengths of the simulation cells used in our calculations ($21\text{--}41 \text{ \AA}$). Within the Wannier–Mott model, the unscreened exciton binding energy of polyynes is $1 R_\infty^* = \mu^*/2 = 0.3 \text{ eV}$. In fact we find the DMC static-nucleus exciton binding energy to be $0.3(1) \text{ eV}$, which is consistent with the small measured exciton binding energies of a range of π -conjugated polymers [189, 190].

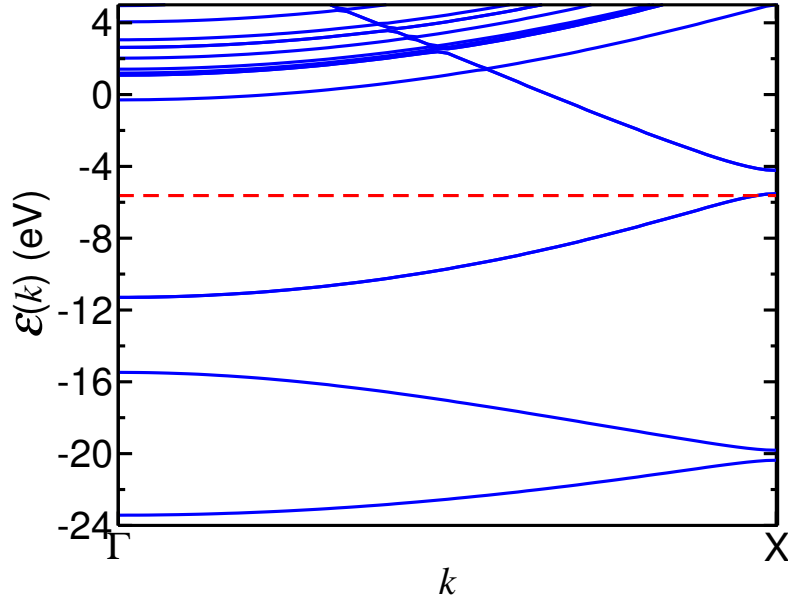


Figure 5.12: DFT-HSE06 band structure of polyynes. The dashed line shows the Fermi energy.

In Table 5.4, we compare the quasiparticle and excitonic gaps of polyynes obtained by different methods. The spread of theoretical results in the literature is remarkable. The static-nucleus DMC gaps were calculated using the DMC ground-state geometry. The DMC static-nucleus singlet excitonic gap is $3.30(7) \text{ eV}$. By extrapolating experimental absorption gaps of oligopynes to infinite chain length, various estimates of the gap of polyynes have been made, ranging from $1.24\text{--}2.56 \text{ eV}$. We note that experimental gaps are strongly affected by finite chain length, solvent, and terminal groups, and that the more recent experimental results on longer

oligoynes (e.g., Ref. 140) are closer to our results.

Table 5.4: Singlet excitonic gaps Δ_{exc} and quasiparticle gaps Δ_{qp} of polyynes obtained by different methods. Most of the gaps were obtained by extrapolation from a series of oligoyne molecules; the number n of pairs of carbon atoms in the largest oligoyne considered in each work is shown where known. The DFT-LDA and DFT-BLYP calculations for polyynes using periodic boundary conditions (PBC) were performed using 133 k points [160]. Where a citation is not given in the table, the data were obtained in the present work.

Method	n	Δ_{exc} (eV)	Δ_{qp} (eV)
DFT-LDA [160]	PBC		0.246
DFT-LDAx [159]	20		0.70
DFT-PW91 [191]	PBC		1.17
DFT-PBE	PBC		1.277
DFT-PBE1PBE [160]	36		1.801
DFT-B88 [159]	20		0.72
DFT-HF [159]	20		6.31
DFT-HF [160]	36		8.500
DFT-LHF [159]	20		0.92
DFT-BLYP [159]	20		0.72
DFT-BLYP [160]	PBC		0.320
DFT-B3LYP [164]	13		1.49
DFT-B3LYP [159]	20		1.50
DFT-B3LYP [160]	36		1.487
DFT-B3LYP [161]	12		1.59
DFT-KMLYP [160]	36		4.438
DFT-BHHLYP [160]	36		3.946
DFT-BHHLYP [161]	12		4.04
DFT-O3LYP [160]	36		0.895
DFT-CAM-B3LYP [161]	12		4.33
DFT-HSE06	PBC		1.301
<i>GW</i> [192]	PBC		0.407
<i>GW</i> [168]	PBC		2.15
MP2 [160]	20		5.541
DMC _{DMC(all)}	PBC	3.30(7)	3.6(1)
Experiment [158]	10	2.20	
Experiment [142]	10	2.20	
Experiment [145]	12	2.18–2.36	
Experiment [164]	10	2.33	
Experiment [156]	10	2.18	
Experiment [157]	12	2.16	
Experiment [146]	12	1.24–1.88	
Experiment [140]	22	2.56	

The vibrational correction to the gap is not as large as in benzene, and the zero-

point correction linearly extrapolated to the thermodynamic limit is $-0.11(2)$ eV[181].

5.4 Conclusions

In summary we have used DMC to calculate the BLA together with the quasiparticle and excitonic gaps of hydrogen-capped oligoynes and extended polyynes. We have found that simpler levels of theory, such as DFT, do not predict either the BLA or the gap with quantitative accuracy. Our DMC calculations show the Peierls-induced BLA of polyynes to be $0.136(2)$ Å, which is significantly higher than DFT predictions. The DMC quasiparticle gap of extended polyynes obtained using the DMC-optimised BLA is $3.6(1)$ eV. The static-nucleus DMC singlet excitonic gap of polyynes is $3.30(7)$ eV. The DMC-calculated zone-centre LO phonon frequency of polyynes is $2084(5)$ cm⁻¹, which is significantly higher than those obtained by DFT, but is consistent with experimental Raman measurements. Our work represents the first direct evaluation of the structural and electronic properties of extended one-dimensional carbon chains using a high-accuracy method.

Overall conclusions

QMC methods are accurate many-body approaches that can be applied for a wide range of extended condensed materials or molecules. They provide accurate zero-temperature ground-state and excited-state energies. Using QMC methods in this work, we have studied the electronic, vibrational and optical properties of several low dimensional materials.

VdW heterostructures or stacked forms of various 2D layers are powerful platforms to design new electronic and optoelectronic devices with engineered properties due to the weak interlayer coupling. Modeling such devices requires the correct form of weak vdW-like interactions between each 2D layer or between the layers and their substrates. VdW interactions make the main contribution to the interlayer BEs, but are wrongly described by the available DFT methods. Our DMC BEs for key test systems such as bilayer graphene and graphene-on-boron nitride can be used as benchmarks to develop vdW functionals in DFT, hopefully enabling the broad applicability of DFT-D or DFT-vdW methods to 2D materials.

The interlayer interactions in vdW heterostructures also create a set of shear modes and layer-breathing modes, corresponding to lateral and vertical displacement of individual layers, respectively. In general, Raman spectroscopy is a key technique for classifying and characterising samples of 2D materials in terms of their point

groups and in particular defining the interlayer vdW and in-plane shear forces. Within the B–O approximation, DMC phonon vibrations are in excellent agreement with experiment wherever they are available. In DFT, the LDA functional produces phonon vibrations closer to experiment than other functionals. Our study shows how first-principles method can be widely used to classify 2D materials. This work could also be extended to study, for example, the phonon properties of vdW structures under the strain.

Another category of 2D materials beyond graphene are TMDCs, which have extensively been studied in the last few years. Around 40 kinds of TMDCs are reported so far, but very limited numbers of studies have reported their optical and electronic properties. Due to the direct band gap in many 2D TMDCs and the bound charge complexes interacting via the strong Coulomb interaction in a reduced dielectric screening environment, they exhibit strong photoluminescence emission compared to the bulk forms, offering innovative opportunities in future 2D optoelectronic devices such as light-emitting diodes and photodetectors. Our exact DMC results for biexcitons show that they are considerably bound in monolayer TMDCs however more investigations needed to classify and model different kinds of bound charge complexes. Our model could be developed to study the optical properties of TMDC heterostructures.

Besides 2D materials, 1D materials such as carbon chains are prospective candidates for nanoelectronic and nanomechanical devices. Due to the Peierls distortion, the electronic and optical properties of 1D carbon chains (polyyne) is very controversial and considerably affected by the geometry. Unlike DFT, the DMC method can be applied to calculate accurately the bond length alternation, the optical phonon frequency and the electronic gaps of extended 1D chains. Based on these experience, the electronic and optical properties of other 1D Peierls-distorted structures such as trans-polyacetylene can be predicted accurately by the DMC method.

Interlayer vdW forces of bilayer graphene

A.1 Introduction

The Lifshitz or vdW theory [193, 194] is valid for the small bodies, whose distances are small comparing with the size of bodies. The fundamental idea is that the interaction between bodies is treated as a fluctuating electromagnetic field and all properties of long range fluctuations and also their contribution to all thermodynamic quantities are explained entirely in terms of the complex dielectric constant of the body. In quantum mechanics, the electromagnetic field is usually described by the Schrödinger operators of the vector potential $\mathbf{A}(\mathbf{r})$ and scalar potential $\phi(\mathbf{r})$. Four dimensional notation of these operators is denoted by $\{A_\alpha\} = (\mathbf{A}, \phi)$ where $\alpha = 0 - 3$. The time dependent operators $A_\alpha(\mathbf{r}, t)$ are also defined by the Heisenberg operators

$$A_\alpha(\mathbf{r}, t) = e^{i\hat{H}t} A_\alpha(\mathbf{r}) e^{-i\hat{H}t}. \quad (\text{A.1})$$

The electric and magnetic fields can be expressed as the choice of gauge, where the scalar potential is zero.

$$\begin{aligned}\mathbf{E}(\mathbf{r}, t) &= -\partial\mathbf{A}(\mathbf{r}, t)/\partial t, \\ \mathbf{H}(\mathbf{r}, t) &= \nabla \times \mathbf{A}(\mathbf{r}, t).\end{aligned}\tag{A.2}$$

The average value of the electric and magnetic fields in the Fourier transformation and in the presence of an external current $\mathbf{j}^{ext}(\mathbf{r}, t)$ satisfy the equations:

$$\begin{aligned}\nabla \times \langle \mathbf{H}(\mathbf{r}, \omega) \rangle &= 4\pi\mathbf{j}^{ext}(\mathbf{r}, \omega) - i\omega\epsilon(\mathbf{r}, \omega)\langle \mathbf{E}(\mathbf{r}, \omega) \rangle, \\ \nabla \times \langle \mathbf{E}(\mathbf{r}, \omega) \rangle &= i\omega\langle \mathbf{H}(\mathbf{r}, \omega) \rangle,\end{aligned}\tag{A.3}$$

where ϵ is the dielectric constant of the region. The statistical or Gibbs average of electric and magnetic fields can be taken using

$$\langle \dots \rangle = \text{tr}\{e^{(F-\hat{H})/T} \dots\},\tag{A.4}$$

in which T is the temperature, the free energy F is used instead of the chemical potential because the chemical potential of electromagnetic field is zero. Eq. A.3 using Eq A.2 can be rewritten as

$$[\epsilon(\mathbf{r}, \omega)\omega^2\delta_{il} - \nabla_{im} \times \nabla_{ml} \times] \langle A_l(\mathbf{r}, \omega) \rangle = -4\pi\mathbf{j}_i^{ext}(\mathbf{r}, \omega).\tag{A.5}$$

The solution of Eq. A.5 can be found using the Green's function method:

$$\langle A_i^{ext}(\mathbf{r}, \omega) \rangle = - \int \mathcal{D}_{il}(\mathbf{r}, \mathbf{r}'; \omega) \mathbf{j}_l^{ext}(\mathbf{r}', \omega) dr',\tag{A.6}$$

where the Green's function \mathcal{D} can be found by solving

$$[\epsilon(\mathbf{r}, \omega)\omega^2\delta_{il} - \nabla_{im} \times \nabla_{ml} \times] \mathcal{D}_{lk}(\mathbf{r}, \mathbf{r}'; \omega) = 4\pi\delta_{ik}\delta(\mathbf{r} - \mathbf{r}').\tag{A.7}$$

Replacing ω by $i|\omega_n|$, the Green's function satisfies

$$[\epsilon(\mathbf{r}, i|\omega_n)|\omega_n^2\delta_{il} + \nabla_{im} \times \nabla_{ml} \times] \mathcal{D}_{lk}(\mathbf{r}, \mathbf{r}'; i|\omega_n) = -4\pi\delta_{ik}\delta(\mathbf{r} - \mathbf{r}'). \quad (\text{A.8})$$

It is possible to find a general form for the vdW part of the thermodynamic quantities for an arbitrary inhomogeneous medium based on the quantum field theory. In quantum field theory, physical quantities are described in perturbation series whose terms can be described by an appropriate Feynman diagram and computed based on Feynman technique. The advantage of the diagram technique is that the terms in the perturbation series can be infinite and the problem can be solved easily by taking a summation over all the infinite sequences which is called “principal diagrams”. Every interline of the diagram are associated with a temperature Green's function for the free particle or a free photon Green's function \mathcal{D} and each intersection of lines (vertex) is related to an interaction operator. Finally, an integration is carried out over the four dimensional coordinates of each vertex in the diagram. The average value of any quantity in the field theory is computed by the equations of motion for the field operators. To preserve the formal similarity with the usual equations of motion, the time t from the real value shifts to the imaginary value of τ which varies from $[-1/T, 1/T]$. The natural unit system $\hbar = c = K_B = 1$ is used here. In a perturbed system, the Hamiltonian is defined as

$$H = H_0 + H_{int}, \quad (\text{A.9})$$

where H_0 is the Hamiltonian of the free particles and photons while H_{int} is the interaction operator:

$$\begin{aligned} H_{int} &= - \int A_\alpha(\mathbf{r}) \cdot \mathbf{j}_\alpha(\mathbf{r}) d^3\mathbf{r}, \\ H_{int}(\tau) &= - \int A_\alpha(\mathbf{r}, \tau) \cdot \mathbf{j}_\alpha(\mathbf{r}, \tau) d^3\mathbf{r}. \end{aligned} \quad (\text{A.10})$$

$A_\alpha(\mathbf{r}, \tau)$ and $\mathbf{j}_\alpha(\mathbf{r}, \tau)$ are defined by using Eq. A.1 with an imaginary time. The

free energy of the thermodynamic system is determined by the relation

$$F = -T\ln(\text{tr}(\rho)), \quad (\text{A.11})$$

where ρ is statistical matrix expressed as

$$\begin{aligned} \rho &= e^{-\frac{H}{T}}, \\ \rho(\tau) &= e^{-\tau H} = e^{-\tau H_0} \mathcal{G}(\tau). \end{aligned} \quad (\text{A.12})$$

where the matrix $\mathcal{G}(\tau)$ is the analogue of the S-matrix in the field theory. It satisfies the equation:

$$-\frac{\partial \mathcal{G}(\tau)}{\partial \tau} = H_{int}(\tau) \mathcal{G}(\tau), \quad \mathcal{G}(0) = 1, \quad (\text{A.13})$$

whose solution is

$$\mathcal{G}(\tau) = T_\tau \exp\left(-\int_0^\tau H_{int}(\tau) d\tau\right), \quad (\text{A.14})$$

where T_τ is the time-ordering operator which orders the operator H in order of increasing time τ . By using Eqs. A.11– A.14, free energy is written as

$$F = F_0 - T\ln(\text{tr}(e^{(F_0-H_0)/T} \mathcal{G})) = F_0 - T\ln\langle \mathcal{G} \rangle_0, \quad (\text{A.15})$$

where F_0 is the free energy of noninteracting particles which defined as $F_0 = -T\ln(\text{tr}(e^{-H_0/T}))$ and $\langle \mathcal{G} \rangle_0 = \text{tr}(e^{(F_0-H_0)/T} \mathcal{G})$. In diagram technique, the total temperature Green's function is defined by the sum of all possible coupled diagrams with two external photon lines. An analytic expression for that is

$$\mathcal{D}_{\alpha\beta}(\mathbf{r}_1, \tau_1; \mathbf{r}_2, \tau_2) = -\frac{\langle T_\tau \{A_\alpha(\mathbf{r}_1, \tau_1) A_\beta(\mathbf{r}_2, \tau_2) \mathcal{G}\} \rangle}{\langle \mathcal{G} \rangle}. \quad (\text{A.16})$$

The total temperature Green's function can be written as

$$\mathcal{D}_{\alpha\beta}(\mathbf{r}_1, \tau_1; \mathbf{r}_2, \tau_2) = \begin{cases} -\text{tr}(e^{(F-H)/T} e^{H(\tau_1-\tau_2)} A_\alpha(\mathbf{r}_1) e^{-H(\tau_1-\tau_2)} A_\beta(\mathbf{r}_2)), & \text{if } \tau_1 > \tau_2 \\ -\text{tr}(e^{(F-H)/T} e^{H(\tau_1-\tau_2)} A_\beta(\mathbf{r}_2) e^{H(\tau_1-\tau_2)} A_\alpha(\mathbf{r}_1)), & \text{if } \tau_2 > \tau_1 \end{cases} \quad (\text{A.17})$$

by which The Green's function have the property $\mathcal{D}(\tau < 0) = \mathcal{D}(\tau + \frac{1}{T})$ where $\tau_1 - \tau_2 = \tau$. It is useful to expand the temperature Green's function $\mathcal{D}_{\alpha\beta}(\mathbf{r}_1, \mathbf{r}_2, \tau)$ in a Fourier series of Green's function.

$$\begin{aligned} \mathcal{D}(\tau) &= T \sum_n e^{-i\omega_n \tau} \mathcal{D}(\omega_n), \\ \mathcal{D}(\omega_n) &= \frac{1}{2} \int_{-1/T}^{1/T} e^{i\omega_n \tau} \mathcal{D}(\tau) d\tau, \quad \omega_n = n\pi T. \end{aligned} \quad (\text{A.18})$$

Transferring $\tau < 0$ to positive τ , the above equation can be rewritten as

$$\mathcal{D}(\omega_n) = \frac{1}{2} (1 + e^{i\omega_n/T}) \int_0^{1/T} e^{i\omega_n \tau} \mathcal{D}(\tau) d\tau, \quad \text{non zero for } \omega_n = 2\pi nT. \quad (\text{A.19})$$

Next, the Fourier series expansion Eq. A.18 is substituted into the all appropriate terms of the perturbation series and taken Fourier transforms with respect to the space variables.

$$\begin{aligned} \mathcal{D}(\mathbf{r}) &= \frac{1}{(2\pi)^3} \int e^{i\mathbf{p}\cdot\mathbf{r}} \mathcal{D}(\mathbf{p}) d\mathbf{p}, \\ \mathcal{D}(\mathbf{p}) &= \int e^{-i\mathbf{p}\cdot\mathbf{r}} \mathcal{D}(\mathbf{r}) d\mathbf{r}. \end{aligned} \quad (\text{A.20})$$

As mentioned before, the vertices in the diagram technique are related to the interaction operators in the system. An even number of fermion lines meet at every vertex, whose coordinates are considered as an integration, which means the

sum of frequencies $\sum_n \omega_n = 2N\pi T$, where N is an integer.

$$\int_0^{1/T} d\tau e^{i\tau \sum \omega_n} = \frac{1}{T} \delta_{\sum \omega_n}, \quad \delta_{\sum \omega_n} \begin{cases} 1, & \text{for } \omega_n = 0. \\ 0, & \text{for } \omega_n \neq 0. \end{cases} \quad (\text{A.21})$$

Integration over the space-time coordinates of the vertices gives rise to Kronecker δ of momentum $\sum \mathbf{p} = 0$ and frequency $\sum \omega_n = 0$ expressing conservation of the energy and momentum. The correction for the Green's function at $T = 0$ can be obtained by replacing all the frequency ω in \mathcal{D} by $i\omega_n$ ($\omega_n = 2n\pi T$). As $T \rightarrow 0$ the main role in the sums over the frequencies ω_n is played by large values of n and therefore, these sums can be replaced by integrals. By noticing that $\Delta\omega = \omega_{n+1} - \omega_n = 2\pi T$, then

$$T \sum_{\omega_n} \dots \rightarrow \frac{1}{2\pi} \int d\omega \dots \quad (\text{A.22})$$

Suppose all the integrals over the momenta of the virtual photons have a cut-off at value k_0 which is much smaller than the reciprocal of the interatomic distances $1/a$. The corresponding expression for the free energy in the approximation where $k_0 a \ll 1$ is

$$\begin{aligned} F = F_0 - \frac{T}{2} \sum_{n=-\infty}^{\infty} & \left[\int \Pi_{ik}(\mathbf{r}_1, \mathbf{r}_2; \omega_n) \mathcal{D}_{ki}^{(0)}(\mathbf{r}_2, \mathbf{r}_1; \omega_n) d\mathbf{r}_1 d\mathbf{r}_2 \right. \\ & + \frac{1}{2} \int \Pi_{ik}(\mathbf{r}_1, \mathbf{r}_2; \omega_n) \mathcal{D}_{kl}^{(0)}(\mathbf{r}_2, \mathbf{r}_3; \omega_n) \\ & \times \Pi_{lp}(\mathbf{r}_3, \mathbf{r}_4; \omega_n) \mathcal{D}_{pi}^{(0)}(\mathbf{r}_4, \mathbf{r}_1; \omega_n) d\mathbf{r}_1 d\mathbf{r}_2 d\mathbf{r}_3 d\mathbf{r}_4 + \dots \\ & + \frac{1}{m} \int \Pi_{ik}(\mathbf{r}_1, \mathbf{r}_2; \omega_n) \mathcal{D}_{kl}^{(0)}(\mathbf{r}_2, \mathbf{r}_3; \omega_n) \dots \\ & \times \Pi_{qs}(\mathbf{r}_{2m-1}, \mathbf{r}_{2m}; \omega_n) \mathcal{D}_{si}^{(0)}(\mathbf{r}_{2m}, \mathbf{r}_1; \omega_n) \\ & \left. d\mathbf{r}_1 \dots d\mathbf{r}_{2m} + \dots \right], \quad (\text{A.23}) \end{aligned}$$

where $\mathcal{D}^{(0)}$ is the Green's function of free photon. F_0 as the unperturbed free energy of the body, includes all the corrections related to the short-range forces

and Π is the polarisation operator which can be obtained by multiplying Eq. A.8 from the left by $\omega_n^2 \delta_{ij} + \nabla_{il} \times \nabla_{lj}$,

$$\Pi_{ij}(\mathbf{r}_1, \mathbf{r}_2; \omega_n) = \frac{1}{4\pi} [\epsilon(\mathbf{r}_1, i|\omega_n|) - 1] \omega_n^2 \delta_{ij} \delta(\mathbf{r}_1, \mathbf{r}_2). \quad (\text{A.24})$$

It is not easy to calculate Eq. A.23 directly, but it can be calculated indirectly by the correction to the stress tensor that includes the interaction between the medium and long wavelength electromagnetic field. Consider the body is subjected to a small deformation with displacement vector $\mathbf{u}(\mathbf{r})$. The change in the free energy δF is equal to $-\int \mathbf{f} \cdot \mathbf{u} dV$ where \mathbf{f} is the force acting on a unit volume of the deformed body. The corresponding change in the unperturbed free energy F_0 is

$$\delta F_0 = \int \mathbf{u} \cdot \nabla p_0 dV, \quad (\text{A.25})$$

where p_0 is the pressure at a given density and temperature without any correction. If the system is isolated and homogenous, \mathcal{D} depends on the coordinate differences $\mathbf{r}_1 - \mathbf{r}_2$ and time difference $\tau_1 - \tau_2$. Hence, by a small change of the displacement on the free energy in Eq. A.23, only polarisation operator changes, whose variation is found by Eq. A.24:

$$\delta \Pi_{ik}(\mathbf{r}_1, \mathbf{r}_2; \omega_n) = \frac{1}{4\pi} \omega_n^2 \delta \epsilon(\mathbf{r}_1, i|\omega_n|) \delta_{ik} \delta(\mathbf{r}_1, \mathbf{r}_2). \quad (\text{A.26})$$

By several implementation, the variation of Eq. A.23 by using Eq. A.26 is

$$\delta F = \delta F_0 - \frac{T}{8\pi} \sum_{n=-\infty}^{\infty} \omega_n^2 \int \mathcal{D}_{li}(\mathbf{r}, \mathbf{r}; \omega_n) \delta \epsilon(\mathbf{r}, i|\omega_n|) d\mathbf{r}. \quad (\text{A.27})$$

As is mentioned before, \mathcal{D} is an even function of $\omega_n = 2n\pi T$, then

$$\delta F = \delta F_0 - \frac{T}{4\pi} \sum_{n=0}^{\infty} \omega_n^2 \int \mathcal{D}_{li}(\mathbf{r}, \mathbf{r}; \omega_n) \delta \epsilon(\mathbf{r}, i|\omega_n|) d\mathbf{r}, \quad (\text{A.28})$$

where the prime on the summation means that the term with $n=0$ is given only a weight of $1/2$. The variation $\delta\epsilon$ is connected with two terms of transport by the medium and change in the density due to deformation.

$$\delta\epsilon = -\mathbf{u} \cdot \nabla\epsilon - \rho \frac{\partial\epsilon}{\partial\rho} \nabla \cdot \mathbf{u}. \quad (\text{A.29})$$

Substituting A.29 and A.25 into A.28, the force \mathbf{f} is

$$\begin{aligned} \mathbf{f} = & -\nabla p_0 - \frac{T}{4\pi} \sum_{n=0}^{\infty} \omega_n^2 \mathcal{D}_{ii}(\mathbf{r}, \mathbf{r}; \omega_n) \nabla \epsilon(\mathbf{r}, i\omega_n) \\ & + \frac{T}{4\pi} \sum_{n=0}^{\infty} \omega_n \nabla [\mathcal{D}_{ii}(\mathbf{r}, \mathbf{r}; \omega_n) \rho \frac{\partial\epsilon(\mathbf{r}, i\omega_n)}{\partial\rho}]. \end{aligned} \quad (\text{A.30})$$

Next, we need to calculate the stress tensor by the force $f_i = -\frac{\partial\sigma_{ik}}{\partial x_k}$. We first introduce two functions:

$$\begin{aligned} \mathcal{D}_{ik}^E(\mathbf{r}, \mathbf{r}'; \omega_n) &= -\omega_n^2 \mathcal{D}_{ik}(\mathbf{r}, \mathbf{r}', \omega_n), \\ \mathcal{D}_{ik}^H(\mathbf{r}, \mathbf{r}'; \omega_n) &= \text{rot}_{il} \text{rot}'_{km} \mathcal{D}_{lm}(\mathbf{r}, \mathbf{r}'; \omega_n). \end{aligned} \quad (\text{A.31})$$

The components of the force using A.30–A.31 and calculating $\epsilon(\mathbf{r}', i\omega_n) \frac{\partial}{\partial x_i} \mathcal{D}_{kk}^E(\mathbf{r}, \mathbf{r}'; \omega_n) + \epsilon(\mathbf{r}, i\omega_n) \frac{\partial}{\partial x_i} \mathcal{D}_{kk}^E(\mathbf{r}, \mathbf{r}'; \omega_n)$ and at the end, setting $\mathbf{r} = \mathbf{r}'$ and some manipulations are

$$\begin{aligned} f_i = & -\frac{\partial p_0}{\partial x_i} + \frac{T}{4\pi} \sum_{n=0}^{\infty} \omega_n \frac{\partial}{\partial x_i} [\mathcal{D}_{kk}^E(\mathbf{r}, \mathbf{r}; \omega_n) \epsilon(\mathbf{r}, i\omega_n) - \mathcal{D}_{kk}^E(\mathbf{r}, \mathbf{r}; \omega_n) \rho(\mathbf{r}) \frac{\partial\epsilon(\mathbf{r}, i\omega_n)}{\partial\rho}] \\ & - \frac{T}{2\pi} \sum_{n=0}^{\infty} \omega_n \left[\frac{\partial}{\partial x_k} \epsilon(\mathbf{r}, i\omega_n) \mathcal{D}_{ik}^E(\mathbf{r}, \mathbf{r}; \omega_n) + \frac{\partial}{\partial x_k} \mathcal{D}_{ik}^H(\mathbf{r}, \mathbf{r}; \omega_n) - \frac{1}{2} \frac{\partial}{\partial x_i} \mathcal{D}_{kk}^H(\mathbf{r}, \mathbf{r}; \omega_n) \right]. \end{aligned} \quad (\text{A.32})$$

Finally, the stress tensor is given by $f_i = -\frac{\partial\sigma_{ik}}{\partial x_k}$.

$$\begin{aligned} \sigma_{ik} = & -\delta_{ik} p_0(\rho, T) - \frac{T}{2\pi} \sum_{n=0}^{\infty} \omega_n \left[-\frac{1}{2} \delta_{ik} \left(\epsilon(\mathbf{r}, i\omega_n) - \rho(\mathbf{r}) \frac{\partial\epsilon(\mathbf{r}, i\omega_n)}{\partial\rho} \right) \mathcal{D}_{\ell\ell}^E(\mathbf{r}, \mathbf{r}; \omega_n) \right. \\ & \left. - \frac{1}{2} \delta_{ik} \mathcal{D}_{\ell\ell}^H(\mathbf{r}, \mathbf{r}; \omega_n) + \epsilon(\mathbf{r}, i\omega_n) \mathcal{D}_{ik}^E(\mathbf{r}, \mathbf{r}; \omega_n) + \mathcal{D}_{ik}^H(\mathbf{r}, \mathbf{r}; \omega_n) \right]. \end{aligned} \quad (\text{A.33})$$

Stress tensor in A.33 involves $\mathcal{D}^E(\mathbf{r}, \mathbf{r}')$ and $\mathcal{D}^H(\mathbf{r}, \mathbf{r}')$ which becomes infinite at $\mathbf{r} = \mathbf{r}'$. This is because of the fact that the short wavelength electromagnetic oscillations make an infinite contribution to \mathcal{D}_{ik} , unless we introduce an appropriate cutoff. The vdW contribution that we are going to find is for the long wavelength oscillations and independent of the character of the cutoff. Therefore, the vdW contribution can be obtained from A.33 by a suitable subtraction in the Green's function

$$\lim_{\mathbf{r}' \rightarrow \mathbf{r}} \{ \mathcal{D}(\mathbf{r}, \mathbf{r}') - \bar{\mathcal{D}}(\mathbf{r}, \mathbf{r}') \}, \quad (\text{A.34})$$

where $\bar{\mathcal{D}}$ is the Green's function of a homogenous unbounded medium, whose dielectric constant coincides with that for inhomogeneous medium at the point at which the vdW force is computed. If the chemical potential in the system is constant, part of the total stress tensor A.33, $-\delta_{ik} p_0(\rho, T) + \frac{T}{4\pi} \sum_{n=0}^{\infty} \rho(\mathbf{r}) \frac{\partial \epsilon(\mathbf{r}, i\omega_n)}{\partial \rho} \mathcal{D}_{\ell\ell}^E(\mathbf{r})$, turns to be constant uniform pressure in the system and make no contribution to the total force acting on the body. Finally, if the surface of the bodies 1 and 2 are at the planes $x = 0$ and $x = \ell$, the region between the bodies is ℓ , then the force \mathbf{f} acting on a unit area of the surface of body 2 equals to

$$\begin{aligned} f(\ell) = \sigma'_{xx}(\ell) = \frac{T}{4\pi} \sum_{n=0}^{\infty} \epsilon_3 [& \mathcal{D}_{yy}^E(\ell, \ell; \omega_n) + \mathcal{D}_{zz}^E(\ell, \ell; \omega_n) - \mathcal{D}_{xx}^E(\ell, \ell; \omega_n)] \\ & + \mathcal{D}_{yy}^H(\ell, \ell; \omega_n) + \mathcal{D}_{zz}^H(\ell, \ell; \omega_n) - \mathcal{D}_{xx}^H(\ell, \ell; \omega_n) \end{aligned}, \quad (\text{A.35})$$

where ϵ_3 is the dielectric constant of the region between the bodies. A positive and negative forces respectively correspond to attraction and repulsion between the bodies.

A.2 vdW forces between two slabs

Consider two slabs are located perpendicular to x axis in different media as is shown in Fig. A.1. ϵ_1, ϵ_3 and ϵ_5 are dielectric constant of media surrounding the slabs and

$\epsilon_2(\mathbf{r}, \omega_n)$ and $\epsilon_4(\mathbf{r}, \omega_n)$ referring to the dielectric function of two anisotropic slabs.

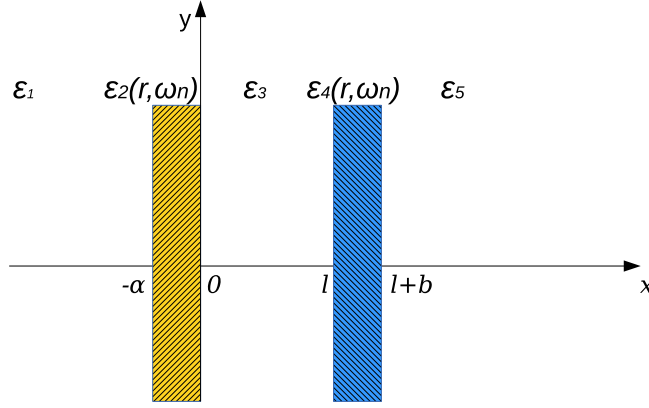


Figure A.1: Two slabs are placed in three different media.

The force \mathbf{f} acting on unit area of the surface of the second slab at a distance of ℓ from the first one depends on the Green's function $\mathcal{D}_{ik}(\mathbf{r}, \mathbf{r}')$ that is in terms of the differences $y - y'$ and $z - z'$ due to the homogeneity of the problem along the y and z axes. The Fourier transformation of the Green's function can be written as

$$\mathcal{D}_{ik}(\mathbf{x}, \mathbf{x}', \mathbf{q}; \omega_n) = \iint e^{-iq_y(y-y')-iq_z(z-z')} \mathcal{D}_{ik}(\mathbf{r}, \mathbf{r}'; \omega_n) d(y-y') d(z-z'). \quad (\text{A.36})$$

Photon Green's function which is defined in Eq. A.8 is recalculated for $i = k = y$.

$$\begin{aligned} \epsilon(\mathbf{r}, i\omega_n)\omega_n^2 \mathcal{D}_{yy}(\mathbf{r}, \mathbf{r}'; \omega_n) + \sum_{ymn} \frac{\partial}{\partial n} \sum_{mpl} \frac{\partial}{\partial p} \mathcal{D}_{ly}(\mathbf{r}, \mathbf{r}'; \omega_n) &= -4\pi\delta(\mathbf{r} - \mathbf{r}') \\ \Rightarrow \epsilon(\mathbf{r}, i\omega_n)\omega_n^2 \mathcal{D}_{yy}(\mathbf{r}, \mathbf{r}'; \omega_n) - \frac{\partial^2}{\partial x^2} \mathcal{D}_{yy}(\mathbf{r}, \mathbf{r}'; \omega_n) + \frac{\partial^2}{\partial x \partial y} \mathcal{D}_{xy}(\mathbf{r}, \mathbf{r}'; \omega_n) \\ + \frac{\partial^2}{\partial z \partial y} \mathcal{D}_{zy}(\mathbf{r}, \mathbf{r}'; \omega_n) - \frac{\partial^2}{\partial z^2} \mathcal{D}_{yy}(\mathbf{r}, \mathbf{r}'; \omega_n) &= -4\pi\delta(\mathbf{r} - \mathbf{r}'). \end{aligned}$$

Taking the Fourier transformation of the above equation by using Eq. A.36, moving the y axis along the vector \mathbf{q} and using the fact that $\mathcal{F}[\frac{d}{dr} \mathcal{D}(\mathbf{r}, \mathbf{r}')] = -i\mathbf{q}\mathcal{D}(\mathbf{x}, \mathbf{x}')$,

the Green's functions changes to

$$\begin{aligned}
& \epsilon(\mathbf{q}, i\omega_n)\omega_n^2 \mathcal{D}_{yy}(\mathbf{x}, \mathbf{x}', \mathbf{q}; \omega_n) - \frac{\partial^2}{\partial x^2} \mathcal{D}_{yy}(\mathbf{x}, \mathbf{x}', \mathbf{q}; \omega_n) + \frac{\partial^2}{\partial x \partial y} \mathcal{D}_{xy}(\mathbf{x}, \mathbf{x}', \mathbf{q}; \omega_n) \\
& + \frac{\partial^2}{\partial z \partial y} \mathcal{D}_{zy}(\mathbf{x}, \mathbf{x}', \mathbf{q}; \omega_n) - \frac{\partial^2}{\partial z^2} \mathcal{D}_{yy}(\mathbf{x}, \mathbf{x}', \mathbf{q}; \omega_n) = -4\pi\delta(\mathbf{x} - \mathbf{x}') \\
& \Rightarrow (w^2 - \mathbf{q}^2 - \frac{d^2}{dx^2}) \mathcal{D}_{yy}(\mathbf{x}, \mathbf{x}', \mathbf{q}; \omega_n) - i\mathbf{q} \frac{d}{dx} \mathcal{D}_{xy}(\mathbf{x}, \mathbf{x}', \mathbf{q}; \omega_n) = -4\pi\delta(\mathbf{x} - \mathbf{x}'),
\end{aligned} \tag{A.37}$$

where $w = \sqrt{\epsilon(\mathbf{q}, i\omega_n)\omega_n^2 + \mathbf{q}^2}$. Similarly, for the other components of the Green's function we can obtain the following equations.

$$\begin{aligned}
& (w^2 - \frac{d^2}{dx^2}) \mathcal{D}_{zz}(\mathbf{x}, \mathbf{x}', \mathbf{q}; \omega_n) = -4\pi\delta(\mathbf{x} - \mathbf{x}'), \\
& w^2 \mathcal{D}_{xy}(\mathbf{x}, \mathbf{x}', \mathbf{q}; \omega_n) - i\mathbf{q} \frac{d}{dx} \mathcal{D}_{yy}(\mathbf{x}, \mathbf{x}', \mathbf{q}; \omega_n) = 0, \\
& w^2 \mathcal{D}_{xx}(\mathbf{x}, \mathbf{x}', \mathbf{q}; \omega_n) - i\mathbf{q} \frac{d}{dx} \mathcal{D}_{xy}(\mathbf{x}, \mathbf{x}', \mathbf{q}; \omega_n) = -4\pi\delta(\mathbf{x} - \mathbf{x}'), \\
& (w^2 - \mathbf{q}^2 - \frac{d^2}{dx^2}) \mathcal{D}_{xy}(\mathbf{x}, \mathbf{x}', \mathbf{q}; \omega_n) - i\mathbf{q} \frac{d}{dx} \mathcal{D}_{xx}(\mathbf{x}, \mathbf{x}', \mathbf{q}; \omega_n) = 0.
\end{aligned} \tag{A.38}$$

The components of the Green's function \mathcal{D}_{xz} and \mathcal{D}_{yz} are equal to zero. The solution of this system reduces to the solution of just two equations:

$$\begin{aligned}
& (w^2 - \frac{d^2}{dx^2}) \mathcal{D}_{zz}(\mathbf{x}, \mathbf{x}', \mathbf{q}; \omega_n) = -4\pi\delta(\mathbf{x} - \mathbf{x}'), \\
& (w^2 - \frac{d^2}{dx^2}) \mathcal{D}_{yy}(\mathbf{x}, \mathbf{x}', \mathbf{q}; \omega_n) = -\frac{4\pi w^2}{\epsilon(\mathbf{q}, i\omega_n)\omega_n^2} \delta(\mathbf{x} - \mathbf{x}'),
\end{aligned} \tag{A.39}$$

and then \mathcal{D}_{xy} and \mathcal{D}_{xx} are defined by the following equations.

$$\begin{aligned}
& \mathcal{D}_{xy}(\mathbf{x}, \mathbf{x}', \mathbf{q}; \omega_n) = \frac{i\mathbf{q}}{w^2} \frac{d}{dx} \mathcal{D}_{yy}(\mathbf{x}, \mathbf{x}', \mathbf{q}; \omega_n), \\
& \mathcal{D}_{xx}(\mathbf{x}, \mathbf{x}', \mathbf{q}; \omega_n) = \frac{i\mathbf{q}}{w^2} \frac{d}{dx} \mathcal{D}_{xy}(\mathbf{x}, \mathbf{x}', \mathbf{q}; \omega_n) - \frac{4\pi}{w^2} \delta(\mathbf{x} - \mathbf{x}').
\end{aligned} \tag{A.40}$$

The solution of the Green's function, can be found from the conditions that \mathcal{D} and $d\mathcal{D}/dx$ are continuous on the boundary. By using the boundary conditions and A.35, together with the inverse Fourier transformation at $\mathbf{r} = \mathbf{r}' = \ell$:

$$f(\ell) = -\frac{T}{\pi} \sum'_{n=0} \int_{2\pi/\lambda}^{\infty} q \, dq \, w_3\left(\frac{1}{\Delta} + \frac{1}{\Delta}\right), \tag{A.41}$$

where λ is the screening length. If The thickness of both slabs are equal to a , ϵ_1 and ϵ_5 equal to ϵ_3 as well as $\epsilon_2(\mathbf{q}, \omega_n) = \epsilon_4(\mathbf{q}, \omega_n)$, Δ and $\bar{\Delta}$ are:

$$\begin{aligned}\Delta &= 1 - e^{2w_3\ell} \left[\frac{(w_2 - w_3)^2 - (w_2 + w_3)^2 e^{2w_2a}}{w_2^2 - w_3^2 - (w_2^2 - w_3^2) e^{2w_2a}} \right]^2, \\ \bar{\Delta} &= 1 - e^{2w_3\ell} \left[\frac{(w_2 - \frac{\epsilon_2}{\epsilon_3} w_3)^2 - (w_2 + \frac{\epsilon_2}{\epsilon_3} w_3)^2 e^{2w_2a}}{w_2^2 - \frac{\epsilon_2^2}{\epsilon_3^2} w_3^2 - (w_2^2 - \frac{\epsilon_2^2}{\epsilon_3^2} w_3^2) e^{2w_2a}} \right]^2.\end{aligned}\quad (\text{A.42})$$

The force \mathbf{f} acting on unit area of each two bodies in media 2 and 4 can be obtained by substituting A.42 into A.41

$$\begin{aligned}f(\ell) &= \frac{T}{\pi} \sum_{n=0}^{\infty} \int_{2\pi/\lambda}^{\infty} qw_3 \, dq \left\{ \left[e^{2w_3\ell} \left(\frac{(w_2 - w_3)^2 - (w_2 + w_3)^2 e^{2w_2a}}{w_2^2 - w_3^2 - (w_2^2 - w_3^2) e^{2w_2a}} \right)^2 - 1 \right]^{-1} \right. \\ &\quad \left. + \left[e^{2w_3\ell} \left(\frac{(w_2 - \frac{\epsilon_2}{\epsilon_3} w_3)^2 - (w_2 + \frac{\epsilon_2}{\epsilon_3} w_3)^2 e^{2w_2a}}{w_2^2 - \frac{\epsilon_2^2}{\epsilon_3^2} w_3^2 - (w_2^2 - \frac{\epsilon_2^2}{\epsilon_3^2} w_3^2) e^{2w_2a}} \right)^2 - 1 \right]^{-1} \right\},\end{aligned}\quad (\text{A.43})$$

where $w_2 = \sqrt{\epsilon_2 \omega_n^2 + q^2}$ and $w_3 = \sqrt{\epsilon_3 \omega_n^2 + q^2}$ depend on ω_n and ϵ and λ is the screening length which depends on the system size by

$$\lambda = \sqrt{\ell^2 + D^2}.\quad (\text{A.44})$$

in which D is the length of the system. ω_n in the usual unit is $\omega_n = 2\pi n K_B T / \hbar$. At large n , the summation in A.43 changes to integral with respect to the value $dn = \frac{\hbar}{2\pi K_B T} d\omega$ therefore the temperature drops out of A.43. By transforming to a new integration variable p by substitution $q = \omega_n \sqrt{\epsilon_3(p^2 - 1)}$ and changing the unit system from natural to the usual unit, the force per unit area of A.43 changes to:

$$f(\ell) = \frac{K_B T}{\pi} \sum_{n=0}^{\infty} \int_{\frac{2\pi}{\sqrt{\ell^2 + D^2}}}^{\infty} wq \, dq \left\{ \frac{1}{r_{TE}^2 e^{2\ell w} - 1} + \frac{1}{r_{TM}^2 e^{2\ell w} - 1} \right\},\quad (\text{A.45})$$

where r_{TE} and r_{TM} are reflection coefficients on the slabs for two independent

polarization of the electromagnetic field, p-polarised transverse electric (TE) and s-polarised transverse magnetic (TM), respectively.

$$r_{TE} = \frac{(s_2^2 - p^2)(1 - e^{2\sqrt{\epsilon_3}\omega s_2 a/c})}{(s_2 - p)^2 - (s_2 + p)^2 e^{2\sqrt{\epsilon_3}\omega s_2 a/c}}, \quad (\text{A.46})$$

and

$$r_{TM} = \frac{(s_2^2 - \frac{\epsilon_2}{\epsilon_3} p^2)(1 - e^{2\sqrt{\epsilon_3}\omega s_2 a/c})}{(s_2 - \frac{\epsilon_2}{\epsilon_3} p)^2 - (s_2 + \frac{\epsilon_2}{\epsilon_3} p)^2 e^{2\sqrt{\epsilon_3}\omega s_2 a/c}}, \quad (\text{A.47})$$

where $w = \sqrt{\epsilon\omega_n^2/c^2 + q^2}$, c is the speed of light, ϵ is the relative permittivity of the media surrounding the layers, D is the length of the system, ω_n is the Matsubara frequencies $\omega_n = 2\pi n K_B T/\hbar$. The prime near the summation sign means that the term of $n = 0$ has the weight of $1/2$.

A.3 vdW forces in bilayer graphene

The same approach can be used for two pristine graphene sheets separated by a distance ℓ . In the framework of the Dirac model, the reflection coefficients are expressed in terms of the polarisation tensor calculated in ref [195]. At large n , the summation in A.45 changes to integral with respect to the value $dn = \frac{\hbar}{2\pi K_B T} d\omega$ therefore the temperature drops out of it.

$$f(\ell) = \frac{\hbar}{2\pi^2} \int_0^\infty d\omega \int_{\frac{2\pi}{\sqrt{\ell^2 + D^2}}}^\infty w q dq \left\{ \frac{1}{r_{TE}^2 e^{2\ell w} - 1} + \frac{1}{r_{TM}^2 e^{2\ell w} - 1} \right\} \quad (\text{A.48})$$

For un-doped bilayer graphene at zero temperature, the energy per unit area is obtained as [81].

$$\begin{aligned}
E &= \frac{\hbar}{2\pi^2} \int_{\ell_0}^{\infty} d\ell \int_0^{\infty} d\omega \int_{\frac{2\pi}{\sqrt{\ell^2+D^2}}}^{\infty} wq \, dq \left\{ \frac{1}{r_{TE}(q, \omega)^2 e^{2\ell\omega} - 1} + \frac{1}{r_{TM}(q, \omega)^2 e^{2\ell\omega} - 1} \right\}, \\
r_{TE}(q, \omega) &= \frac{\alpha\pi}{2\sqrt{v(q, \omega)} + \alpha\pi}, \\
r_{TM}(q, \omega) &= \frac{\alpha\pi\sqrt{v(q, \omega)}}{2 + \alpha\pi\sqrt{v(q, \omega)}}, \\
v(q, \omega) &= v_f^2 + (1 - v_f^2)\frac{\omega^2}{w^2c^2},
\end{aligned} \tag{A.49}$$

where $v_f = 1/300$ is the dimensionless Fermi velocity, $\alpha = e^2/(\hbar c) = 1/300$ is the fine-structure constant. In this model, two layers are interacting via the zero-point and thermal fluctuations of the electromagnetic field using the Dirac model. The short wavelength electromagnetic oscillations make an infinite contribution to \mathcal{D}_{ik} , leading the stress tensor tends to infinity therefore we find vdW interactions for long wavelength oscillations. Here, it is supposed that the separation between sheets is big enough so that the wave functions in different layers do not overlap and also the interband transitions are negligible as the layers are narrow enough so that only one level is occupied in each layer and the closest unoccupied level is far enough up.

Another study has reported the Casimir energy between two un-doped graphene layers embedded in a dielectric medium calculated by using Coulomb coupling method between density fluctuations[80, 196]. The force per unit area of each graphene layer is calculated by considering just the interlayer correlation energy as follows:

$$\begin{aligned}
f(\ell) &= \int \frac{d^2q}{4\pi^2} f_c(q, \ell) \langle \rho_q^1 \rho_{-q}^2 \rangle \\
&= \frac{\hbar}{2\pi^2} \int_0^{\infty} d\omega \int_{\frac{2\pi}{\sqrt{\ell^2+D^2}}}^{\infty} q^2 \, dq \frac{1}{e^{2q\ell} \left(1 + \frac{16}{g\beta} \sqrt{1 + \omega^2/(vq)^2} \right)^2 - 1}
\end{aligned} \tag{A.50}$$

where the Coulomb coupling between density fluctuations ρ_q^1 and ρ_q^2 are given by $v_c(q, \ell) = e^2 e^{-q\ell/(2\epsilon_3 q)}$ with elementary charge e and the relative permittivity of media surrounding the layers ϵ_3 . $f_c(q, \ell) = -\partial_\ell v_c(q, \ell)$ is the Coulomb force. v is the carrier velocity 10^6 m/s in graphene, g is the degeneracy parameter with the value of 4 (2 for spin and 2 for the cone degeneracy) and $\beta = e^2/(2\epsilon_3 \hbar v) \sim 13.6$ is effective coulomb coupling constant of graphene. Then the vdW energy per unit area of each layer is given by:

$$E = \frac{\hbar}{2\pi^2} \int_{\ell_0}^{\infty} d\ell \int_0^{\infty} d\omega \int_{\frac{2\pi}{\sqrt{\ell^2 + D^2}}}^{\infty} q^2 dq \frac{1}{e^{2q\ell} \left(1 + \frac{16}{g\beta} \sqrt{1 + \omega^2/(vq)^2}\right)^2 - 1} \quad (\text{A.51})$$

To solve A.49 and A.51, the parameters are considered as follows: the speed of light $c = 3 \times 10^{18}$ Å/s, $\hbar = 6.58211928 \times 10^{-16}$ eV.s, relative permittivity of the media between two layers $\epsilon_3 = 1$, Initial interlayer separation $\ell_0 = 3.384$ Å and the length of a graphene layer composed of N unit cells $D = \sqrt{2.46^2 N \frac{\sqrt{3}}{2\pi}}$ where 2.46 is graphene lattice constant. The vdW energy per unit area of the layers multiplied by the area of the graphene unit cell $2.46^2 \sqrt{3}/2 = 5.241 \text{Å}^2$ and divided by 2 (the number of atoms per primitive cell) gives energy in terms of eV/atom. The vdW energy for two infinite length free standing graphene layers using both A.49 and A.51 are obtained 8.8 meV/atom, which is almost twice smaller than that calculated using DMC method for limited system length (Fig. A.2).

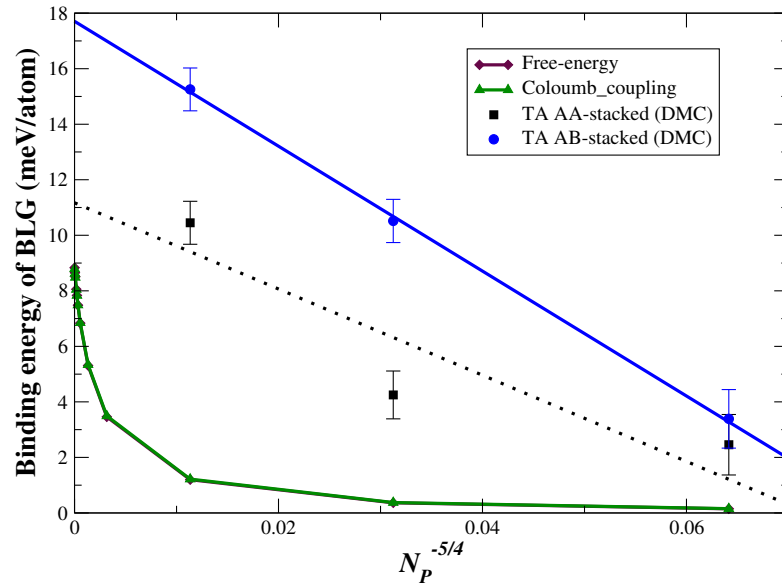


Figure A.2: Comparison of vdW energy of bilayer graphene obtained by Coloumb coupling method A.51, thermal free energy A.49 method and binding energy of AA-stacked and AB-stacked obtained by DMC for bilayer composed of 9, 16 and 36 unit cells which is extrapolated to infinite system size.

Bibliography

- [1] J. J. Thomson, *Phil. Mag. S.* **44**, 293 (1897).
- [2] D. Vanderbilt, *Phys. Rev. B* **41**, 7892 (1990).
- [3] S. Clark, M. Segall, C. Pickard, P. Hasnip, M. Probert, K. Refson, and M. Payne, *Z. Kristallographie* **220**, 567 (2005), reproduced with permission from the publisher.
- [4] J. R. Trail and R. J. Needs, *J. Chem. Phys.* **122**, 014112 (2005).
- [5] D. R. Hartree, *Proc. Camb. Phil. Soc.* **24**, 89 (1928).
- [6] A. Szabo and N. S. Ostlund, *Modern Quantum Chemistry: Introduction to Advanced Electronic Structure Theory* (New York: Free, 1982).
- [7] G. Giuliani and V. Giovanni, *Quantum theory of the electron liquid* (Cambridge University Press, 2005).
- [8] J. A. Pople, *Rev. Mod. Phys.* **71**, 1267 (1999).
- [9] P. R. Taylor, G. Bacskey, N. Hush, and A. Hurley, *Chem. Phys. Lett.* **41**, 444 (1976).
- [10] C. Møller and M. S. Plesset, *Phys. Rev.* **46**, 618 (1934).
- [11] P. Hohenberg and W. Kohn, *Phys. Rev.* **136**, B864 (1964).
- [12] W. Kohn and L. J. Sham, *Phys. Rev.* **140**, A1133 (1965).
- [13] M. C. Payne, M. P. Teter, D. C. Allan, T. A. Arias, and J. D. Joannopoulos, *Rev. Mod. Phys.* **64**, 1045 (1992).
- [14] J. P. Perdew, K. Burke, and M. Ernzerhof, *Phys. Rev. Lett.* **77**, 3865 (1996).
- [15] C. Lee, W. Yang, and R. G. Parr, *Phys. Rev. B* **37**, 785 (1988).
- [16] A. D. Becke, *J. Chem. Phys.* **98**, 5648 (1993).
- [17] J. Heyd, G. E. Scuseria, and M. Ernzerhof, *J. Chem. Phys.* **118**, 8207 (2003).
- [18] J. Heyd, G. E. Scuseria, and M. Ernzerhof, *J. Chem. Phys.* **124**, 219906 (2006).

- [19] N. W. Ashcroft and N. D. Mermin, in *Solid State Physics* (Harcourt College Publishers, New York : Holt, Rinehart and Winston, South Melbourne ; London, 1976).
- [20] D. Alfè and M. J. Gillan, *Phys. Rev. B* **70**, 161101 (2004).
- [21] R. J. Needs, M. D. Towler, N. D. Drummond, and P. López Ríos, *J. Phys.: Condens. Matter* **22**, 023201 (2010).
- [22] W. M. C. Foulkes, L. Mitas, R. J. Needs, and G. Rajagopal, *Rev. Mod. Phys.* **73**, 33 (2001).
- [23] N. Metropolis, A. W. Rosenbluth, M. N. Rosenbluth, A. H. Teller, and E. Teller, *J. Chem. Phys.* **21**, 1087 (1953).
- [24] T. Kato, *Comm. Pure and Appl. Math.* **10**, 151 (1957).
- [25] R. T. Pack and W. B. Brown, *J. Chem. Phys.* **45** (1966).
- [26] C. J. Umrigar, K. G. Wilson, and J. W. Wilkins, *Phys. Rev. Lett.* **60**, 1719 (1988).
- [27] N. D. Drummond and R. J. Needs, *Phys. Rev. B* **72**, 085124 (2005).
- [28] M. P. Nightingale and V. Melik-Alaverdian, *Phys. Rev. Lett.* **87**, 043401 (2001).
- [29] J. Toulouse and C. J. Umrigar, *J. Chem. Phys.* **126**, 084102 (2007).
- [30] C. J. Umrigar, J. Toulouse, C. Filippi, S. Sorella, and R. G. Hennig, *Phys. Rev. Lett.* **98**, 110201 (2007).
- [31] M. Suzuki, *Commun. Math. Phys.* **51**, 183 (1976).
- [32] N. D. Drummond, unpublished (2012).
- [33] H. Flyvbjerg and H. G. Petersen, *J. Chem. Phys.* **91**, 461 (1989).
- [34] R. Needs, M. Towler, N. Drummond, and P. López Ríos, in *CASINO version 2.13 user manual* (University of Cambridge, 2015).
- [35] J. B. Anderson, *J. Chem. Phys.* **65** (1976).
- [36] E. Wigner and F. Seitz, *Phys. Rev.* **46**, 509 (1934).
- [37] R. P. Feynman, *Phys. Rev.* **94**, 262 (1954).
- [38] R. P. Feynman and M. Cohen, *Phys. Rev.* **102**, 1189 (1956).
- [39] M. A. Lee, K. E. Schmidt, M. H. Kalos, and G. V. Chester, *Phys. Rev. Lett.* **46**, 728 (1981).
- [40] Y. Kwon, D. M. Ceperley, and R. M. Martin, *Phys. Rev. B* **48**, 12037 (1993).
- [41] Y. Kwon, D. M. Ceperley, and R. M. Martin, *Phys. Rev. B* **58**, 6800 (1998).

- [42] N. D. Drummond, R. J. Needs, A. Sorouri, and W. M. C. Foulkes, *Phys. Rev. B* **78**, 125106 (2008).
- [43] S. Grimme, *J. Comp. Chem.* **25**, 1463 (2004).
- [44] S. Grimme, *J. Comp. Chem.* **27**, 1787 (2006).
- [45] M. Hasegawa, K. Nishidate, and H. Iyetomi, *Phys. Rev. B* **76**, 115424 (2007).
- [46] S. Grimme, J. Antony, S. Ehrlich, and H. Krieg, *J. Chem. Phys.* **132**, 154104 (2010).
- [47] A. Tkatchenko and M. Scheffler, *Phys. Rev. Lett.* **102**, 073005 (2009).
- [48] H. Rydberg, M. Dion, N. Jacobson, E. Schröder, P. Hyldgaard, S. I. Simak, D. C. Langreth, and B. I. Lundqvist, *Phys. Rev. Lett.* **91**, 126402 (2003).
- [49] M. Dion, H. Rydberg, E. Schröder, D. C. Langreth, and B. I. Lundqvist, *Phys. Rev. Lett.* **92**, 246401 (2004).
- [50] S. D. Chakarova-Käck, E. Schröder, B. I. Lundqvist, and D. C. Langreth, *Phys. Rev. Lett.* **96**, 146107 (2006).
- [51] T. Thonhauser, V. R. Cooper, S. Li, A. Puzder, P. Hyldgaard, and D. C. Langreth, *Phys. Rev. B* **76**, 125112 (2007).
- [52] S. Lebègue, J. Harl, T. Gould, J. G. Ángyán, G. Kresse, and J. F. Dobson, *Phys. Rev. Lett.* **105**, 196401 (2010).
- [53] T. Olsen and K. S. Thygesen, *Phys. Rev. B* **87**, 075111 (2013).
- [54] H. Eshuis, J. Bates, and F. Furche, *Theor. Chem. Acc.* **131**, 1084 (2012).
- [55] X. Ren, P. Rinke, C. Joas, and M. Scheffler, *J. Mater. Sci.* **47**, 7447 (2012).
- [56] B. Jeziorski, R. Moszynski, and K. Szalewicz, *Chemical Reviews* **94**, 1887 (1994).
- [57] L. A. Girifalco and R. A. Lad, *J. Chem. Phys.* **25** (1956).
- [58] L. A. Girifalco, M. Hodak, and R. S. Lee, *Phys. Rev. B* **62**, 13104 (2000).
- [59] J. F. Dobson, A. White, and A. Rubio, *Phys. Rev. Lett.* **96**, 073201 (2006).
- [60] L. X. Benedict, N. G. Chopra, M. L. Cohen, A. Zettl, S. G. Louie, and V. H. Crespi, *Chem. Phys. Lett.* **286**, 490 (1998).
- [61] R. Zacharia, H. Ulbricht, and T. Hertel, *Phys. Rev. B* **69**, 155406 (2004).
- [62] Z. Liu, J. Z. Liu, Y. Cheng, Z. Li, L. Wang, and Q. Zheng, *Phys. Rev. B* **85**, 205418 (2012).
- [63] T. Gould, Z. Liu, J. Z. Liu, J. F. Dobson, Q. Zheng, and S. Lebgue, *J. Chem. Phys.* **139**, 224704 (2013).

- [64] L. Spanu, S. Sorella, and G. Galli, *Phys. Rev. Lett.* **103**, 196401 (2009).
- [65] P. Ganesh, J. Kim, C. Park, M. Yoon, F. A. Reboredo, and P. R. C. Kent, *J. Chem. Theo. and Comp.* **10**, 5318 (2014).
- [66] I. V. Lebedeva, A. A. Knizhnik, A. M. Popov, Y. E. Lozovik, and B. V. Potapkin, *Phys. Chem. Chem. Phys.* **13**, 5687 (2011).
- [67] Y. J. Dappe, P. G. Bolcatto, J. Ortega, and F. Flores, *Journal of Physics: Condensed Matter* **24**, 424208 (2012).
- [68] R. Podeszwa, *J. Chem. Phys.* **132**, 044704 (2010).
- [69] T. Gould, S. Lebgue, and J. F. Dobson, *Journal of Physics: Condensed Matter* **25**, 445010 (2013).
- [70] W. Gao and A. Tkatchenko, *Phys. Rev. Lett.* **114**, 096101 (2015).
- [71] D. M. Ceperley and B. J. Alder, *Phys. Rev. Lett.* **45**, 566 (1980).
- [72] C.-R. Hsing, C. Cheng, J.-P. Chou, C.-M. Chang, and C.-M. Wei, *New J. Phys.* **16**, 113015 (2014).
- [73] J. R. Trail and R. J. Needs, *J. Chem. Phys.* **122**, 174109 (2005).
- [74] H. B. G. Casimir and D. Polder, *Phys. Rev.* **73**, 360 (1948).
- [75] I. Brihuega, P. Mallet, H. González-Herrero, G. Trambly de Laissardière, M. M. Ugeda, L. Magaud, J. M. Gómez-Rodríguez, F. Ynduráin, and J.-Y. Veullen, *Phys. Rev. Lett.* **109**, 196802 (2012).
- [76] N. D. Drummond, M. D. Towler, and R. J. Needs, *Phys. Rev. B* **70**, 235119 (2004).
- [77] C. J. Umrigar, M. P. Nightingale, and K. J. Runge, *J. Chem. Phys.* **99** (1993).
- [78] D. Parry, *Surf. Sci.* **54**, 195 (1976).
- [79] B. Wood, W. M. C. Foulkes, M. D. Towler, and N. D. Drummond, *J. Phys.: Cond. Mat.* **16**, 891 (2004).
- [80] G. Gómez-Santos, *Phys. Rev. B* **80**, 245424 (2009).
- [81] G. L. Klimchitskaya and V. M. Mostepanenko, *Phys. Rev. B* **87**, 075439 (2013).
- [82] C. Lin, F. H. Zong, and D. M. Ceperley, *Phys. Rev. E* **64**, 016702 (2001).
- [83] H. Shin, S. Kang, J. Koo, H. Lee, J. Kim, and Y. Kwon, *J. Chem. Phys.* **140**, 114702 (2014).
- [84] G. Graziano, J. Klimeš, F. Fernandez-Alonso, and A. Michaelides, *J. Phys.: Cond. Mat.* **24**, 424216 (2012).

- [85] M. Hasegawa and K. Nishidate, *Phys. Rev. B* **70**, 205431 (2004).
- [86] A. Hansson, F. de Brito Mota, and R. Rivelino, *Phys. Rev. B* **86**, 195416 (2012).
- [87] N. Troullier and J. L. Martins, *Phys. Rev. B* **43**, 1993 (1991).
- [88] M. Burkatzki, C. Filippi, and M. Dolg, *J. Chem. Phys.* **126**, 234105 (2007).
- [89] L. Mitáš, E. L. Shirley, and D. M. Ceperley, *J. Chem. Phys.* **95**, 3467 (1991).
- [90] F. Ortmann, F. Bechstedt, and W. G. Schmidt, *Phys. Rev. B* **73**, 205101 (2006).
- [91] K. Refson, P. R. Tulip, and S. J. Clark, *Phys. Rev. B* **73**, 155114 (2006).
- [92] W. Haynes, in *CRC Handbook of Chemistry and Physics, 91st Edition* (CRC Press, Inc., Boca Raton, 2010–2011) pp. 5–1.
- [93] J. F. Dobson, T. Gould, and G. Vignale, *Phys. Rev. X* **4**, 021040 (2014).
- [94] C. H. Lui and T. F. Heinz, *Phys. Rev. B* **87**, 121404 (2013).
- [95] S. K. Saha, U. V. Waghmare, H. R. Krishnamurthy, and A. K. Sood, *Phys. Rev. B* **78**, 165421 (2008).
- [96] A. Ferrari and S. Milana, (unpublished) presented at Graphene Week Conference (2015).
- [97] A. K. Geim and I. V. Grigorieva, *Nature* **499**, 419 (2013).
- [98] C. Dean, A. Young, I. Meric, C. Lee, L. Wang, S. Sorgenfrei, K. Watanabe, P. Taniguchi, T. Kim, K. Shepard, and J. Hone, *Nat. Nano.* **5**, 722 (2010).
- [99] S. Haigh, A. Gholinia, R. Jalil, S. Romani, L. Britnell, D. Elias, K. Novoselov, L. Ponomarenko, A. Geim, and R. Gorbachev, *Nat. Mater.* **11**, 764 (2012).
- [100] H. Wang, T. Taychatanapat, A. Hsu, K. Watanabe, T. Taniguchi, P. Jarillo-Herrero, and T. Palacios, *Elec. Dev. Lett., IEEE* **32**, 1209 (2011).
- [101] I. Meric, C. Dean, A. Young, J. Hone, P. Kim, and K. L. Shepard, *Proc. IEEE* **101**, 1609 (2013).
- [102] F. Withers, O. Del Pozo-Zamudio, A. Mishchenko, A. P. Rooney, A. Gholinia, K. Watanabe, T. Taniguchi, S. J. Haigh, A. K. Geim, A. I. Tartakovskii, and K. S. Novoselov, *Nat. Mater.* **14**, 301 (2015).
- [103] A. Woessner, M. B. Lundberg, Y. Gao, A. Principi, P. Alonso-González, M. Carrega, K. Watanabe, T. Taniguchi, G. Vignale, M. Polini, J. Hone, R. Hillenbrand, and F. H. L. Koppens, *Nat. Mater.* **14**, 421 (2015).
- [104] J. Xue, J. Sanchez-Yamagishi, D. Bulmash, P. Jacquod, A. Deshpande, K. Watanabe, T. Taniguchi, P. Jarillo-Herrero, and B. J. LeRoy, *Nat. Mater.* **10**, 282 (2011).

- [105] B. Sachs, T. O. Wehling, M. I. Katsnelson, and A. I. Lichtenstein, *Phys. Rev. B* **84**, 195414 (2011).
- [106] M. Yankowitz, J. Xue, D. Cormode, J. D. Sanchez-Yamagishi, K. Watanabe, T. Taniguchi, P. Jarillo-Herrero, P. Jacquod, and B. J. LeRoy, *Nat. Phys.* **8**, 382 (2012).
- [107] J. R. Wallbank, M. Mucha-Kruczynski, X. Chen, and V. I. Fal'ko, *Ann. Phys. (Berlin)* **527**, 359 (2015).
- [108] C. R. Dean, L. Wang, P. Maher, C. Forsythe, F. Ghahari, Y. Gao, J. Katoch, M. Ishigami, P. Moon, M. Koshino, T. Taniguchi, K. Watanabe, K. L. Shepard, J. Hone, and P. Kim, *Nature* **497**, 598 (2013).
- [109] L. Wang, Y. Gao, B. Wen, Z. Han, T. Taniguchi, K. Watanabe, M. Koshino, J. Hone, and C. R. Dean, **350**, 1231 (2015).
- [110] Y. Fan, M. Zhao, Z. Wang, X. Zhang, and H. Zhang, *App. Phys. Lett.* **98**, 083103 (2011).
- [111] G. J. Slotman, G. A. de Wijs, A. Fasolino, and M. I. Katsnelson, *Ann. Phys. (Berlin)* **526**, 381 (2014).
- [112] S. Jung, M. Park, J. Park, T.-Y. Jeong, H.-J. Kim, K. Watanabe, T. Taniguchi, D. H. Ha, C. Hwang, and Y.-S. Kim, *Sci. Rep.* **5**, 16642 (2015).
- [113] A. Ramasubramaniam, *Phys. Rev. B* **86**, 115409 (2012).
- [114] T. Cheiwchanchamnangij and W. R. L. Lambrecht, *Phys. Rev. B* **85**, 205302 (2012).
- [115] D. Y. Qiu, F. H. da Jornada, and S. G. Louie, *Phys. Rev. Lett.* **111**, 216805 (2013).
- [116] A. Chernikov, T. C. Berkelbach, H. M. Hill, A. Rigosi, Y. Li, O. B. Aslan, D. R. Reichman, M. S. Hybertsen, and T. F. Heinz, *Phys. Rev. Lett.* **113**, 076802 (2014).
- [117] Z. Ye, T. Cao, K. O'Brien, H. Zhu, X. Yin, Y. Wang, S. G. Louie, and X. Zhang, *Nature* **513**, 214 (2014).
- [118] J. S. Ross, S. Wu, H. Yu, N. J. Ghimire, A. M. Jones, G. Aivazian, J. Yan, D. G. Mandrus, D. Xiao, W. Yao, and X. Xu, *Nat. Commun.* **4**, 1474 (2013).
- [119] K. F. Mak, K. He, C. Lee, G. H. Lee, J. Hone, T. F. Heinz, and J. Shan, *Nat. Mater.* **12**, 207 (2013).
- [120] Y. Lin, X. Ling, L. Yu, S. Huang, A. L. Hsu, Y.-H. Lee, J. Kong, M. S. Dresselhaus, and T. Palacios, *Nano Lett.* **14**, 5569 (2014).
- [121] C. Mai, A. Barrette, Y. Yu, Y. G. Semenov, K. W. Kim, L. Cao, and K. Gundogdu, *Nano Lett.* **14**, 202 (2014).

- [122] J. Shang, X. Shen, C. Cong, N. Peimyoo, B. Cao, M. Eginligil, and T. Yu, *ACS Nano* **9**, 647 (2015).
- [123] Y. You, Z. Xiao-Xiao, T. C. Berkelbach, M. S. Hybertsen, D. R. Reichman, and T. F. Heinz, *Nat. Phys.* **11**, 477 (2015).
- [124] G. Plechinger, P. Nagler, J. Kraus, N. Paradiso, C. Strunk, C. Schller, and T. Korn, *Phys. Stat. Solidi* **9**, 457 (2015).
- [125] E. J. Sie, A. J. Frenzel, Y.-H. Lee, J. Kong, and N. Gedik, *Phys. Rev. B* **92**, 125417 (2015).
- [126] K. A. Velizhanin and A. Saxena, *Phys. Rev. B* **92**, 195305 (2015).
- [127] T. C. Berkelbach, M. S. Hybertsen, and D. R. Reichman, *Phys. Rev. B* **88**, 045318 (2013).
- [128] M. Z. Mayers, T. C. Berkelbach, M. S. Hybertsen, and D. R. Reichman, *Phys. Rev. B* **92**, 161404 (2015).
- [129] I. Kylänpää and H.-P. Komsa, *Phys. Rev. B* **92**, 205418 (2015).
- [130] P. Cudazzo, I. V. Tokatly, and A. Rubio, *Phys. Rev. B* **84**, 085406 (2011).
- [131] L. V. Keldysh, *JETP* **29**, 658 (1979).
- [132] B. Ganchev, N. Drummond, I. Aleiner, and V. Fal'ko, *Phys. Rev. Lett.* **114**, 107401 (2015).
- [133] P. López Ríos, P. Seth, N. D. Drummond, and R. J. Needs, *Phys. Rev. E* **86**, 036703 (2012).
- [134] G. G. Spink, P. López Ríos, N. D. Drummond, and R. J. Needs, arXiv e-prints: 1505.07411 .
- [135] B. Stébé and A. Ainane, *Superlatt. and Microstruct.* **5**, 545 (1989).
- [136] H. W. Kroto, J. R. Heath, S. C. O'Brien, R. F. Curl, and R. E. Smalley, *Astrophys. J.* **267**, 362 (1995).
- [137] W. W. Duley, *Astrophys. J.* **10**, 362 (2000).
- [138] H. W. Kroto, J. R. Heath, S. C. O'Brien, R. F. Curl, and R. E. Smalley, *Nature* **318**, 162 (1985).
- [139] L. Shi, P. Rohringer, K. Suenaga, Y. Niimi, J. Kotakoski, J. C. Meyer, H. Peterlik, P. Ayala, and T. Pichler, arXiv:1507.04896v2 (2015).
- [140] W. A. Chalifoux and R. R. Tykwinski, *Nat. Chem.* **2**, 967 (2010).
- [141] R. J. Lagow, J. J. Kampa, H.-C. Wei, S. L. Battle, J. W. Genge, D. A. Laude, C. J. Harper, R. Bau, R. C. Stevens, J. F. Haw, and E. Munson, *Science* **267**, 362 (1995).

- [142] T. Gibtner, F. Hampel, J.-P. Gisselbrecht, and A. Hirsch, *Chem. Eur. J.* **8**, 408 (2002).
- [143] M. Tsuji, T. Tsuji, S. Kuboyama, S.-H. Yoon, Y. Korai, T. Tsujimoto, K. Kubo, A. Mori, and I. Mochida, *Chem. Phys. Lett.* **355**, 101 (2002).
- [144] R. Matsutani, T. Kakimoto, K. Wada, T. Sanada, H. Tanaka, and K. Kojima, *Carbon* **46**, 1103 (2008).
- [145] W. Mohr, J. Stahl, F. Hampel, and J. A. Gladysz, *Chem. Eur. J.* **9**, 3324 (2003).
- [146] M. Samoc, G. T. Dalton, J. A. Gladysz, Q. Zheng, Y. Velkov, H. Ågren, P. Norman, and M. G. Humphrey, *Inorg. Chem.* **47**, 9946 (2008).
- [147] W. A. Chalifoux, M. J. Ferguson, R. McDonald, F. Melin, L. Echevoyen, and R. R. Tykwinski, *J. Phys. Org. Chem.* **25**, 69 (2012).
- [148] Ž. Crljen and G. Baranović, *Phys. Rev. Lett.* **98**, 116801 (2007).
- [149] B. Standley, W. Bao, H. Zhang, J. Bruck, C. N. Lau, and M. Bockrath, *Nano Lett.* **8**, 3345 (2008).
- [150] K. H. Khoo, J. B. Neaton, Y. W. Son, M. L. Cohen, and S. G. Louie, *Nano Lett.* **8**, 2900 (2008).
- [151] P. E. Hopkins, *Appl. Phys. Lett.* **96**, 041901 (2010).
- [152] R. H. Baughman, *Science New Series*, **312**, 1009 (2006).
- [153] M. Liu, V. I. Artyukhov, H. Lee, F. Xu, and B. I. Yakobson, *ACS Nano* **7**, 10075 (2013).
- [154] V. I. Artyukhov, M. Liu, and B. I. Yakobson, *Nano Lett.* **14**, 4224 (2014).
- [155] R. Peierls, *Quantum theory of solids* (Oxford University Press, Oxford, 1955) pp. 108–112.
- [156] S. Eisler, A. D. Slepko, E. Elliott, T. Luu, R. McDonald, F. A. Hegmann, and R. R. Tykwinski, *J. Am. Chem. Soc.* **127**, 2666 (2005).
- [157] Q. Zheng, J. C. Bohling, T. B. Peters, A. C. Frisch, F. Hampel, and J. A. Gladysz, *Chem. Eur. J.* **12**, 6486 (2006).
- [158] R. Dembinski, T. Bartik, B. Bartik, M. Jaeger, and J. A. Gladysz, *J. Am. Chem. Soc.* **122**, 810 (2000).
- [159] M. Weimer, W. Hieringer, F. D. Sala, and A. Görling, *Chem. Phys.* **309**, 77 (2005).
- [160] S. Yang and M. Kertesz, *J. Phys. Chem. A* **110**, 9771 (2006).
- [161] M. J. G. Peach, E. I. Tellgren, P. Salek, T. Helgaker, and D. J. Tozer, *J. Phys. Chem. A* **111**, 11930 (2007).

- [162] C. Zhang, Z. Cao, H. Wu, and Q. Zhang, *Int. J. Quantum Chem.* **98**, 299 (2004).
- [163] A. Imamura and Y. Aoki, *Int. J. Quantum Chem.* **113**, 423 (2013).
- [164] F. Zhuravlev and J. A. Gladysz, *Chem. A Eur. J.* **10**, 6510 (2004).
- [165] A. Abdurahman, A. Shukla, and M. Dolg, *Phys. Rev. B* **65**, 115106 (2002).
- [166] T. D. Poulsen, K. V. Mikkelsen, J. G. Fripiat, D. Jacquemin, and B. Champagne, *J. Chem. Phys.* **114**, 5917 (2001).
- [167] C. D. Zeinalipour-Yazdi and D. P. Pullman, *J. Phys. Chem. B* **112**, 7377 (2008).
- [168] A. Al-Backri, V. Zólyomi, and C. J. Lambert, *J. Chem. Phys.* **140**, 104306 (2014).
- [169] C. J. Lambert, *Chem. Soc. Rev.* **44**, 875 (2015).
- [170] L. Mitáš and R. M. Martin, *Phys. Rev. Lett.* **72**, 2438 (1994).
- [171] A. J. Williamson, R. Q. Hood, R. J. Needs, and G. Rajagopal, *Phys. Rev. B* **57**, 12140 (1998).
- [172] M. D. Towler, R. Q. Hood, and R. J. Needs, *Phys. Rev. B* **62**, 2330 (2000).
- [173] A. J. Williamson, J. C. Grossman, R. Q. Hood, A. Puzder, and G. Galli, *Phys. Rev. Lett.* **89**, 196803 (2002).
- [174] N. D. Drummond, A. J. Williamson, R. J. Needs, and G. Galli, *Phys. Rev. Lett.* **95**, 096801 (2005).
- [175] R. M. Lee and N. D. Drummond, *Phys. Rev. B* **83**, 245114 (2011).
- [176] F. Marsusi, J. Sabbaghzadeh, and N. D. Drummond, *Phys. Rev. B* **84**, 245315 (2011).
- [177] C. E. Patrick and F. Giustino, *Nat. Commun.* **4**, 2006 (2013).
- [178] G. Nemeth, H. Selzle, and E. Schlag, *Chem. Phys. Lett.* **215**, 151 (1993).
- [179] J. P. Doering, *J. Chem. Phys.* **51**, 2866 (1969).
- [180] A. Hiraya and K. Shobatake, *J. Chem. Phys.* **94**, 7700 (1991).
- [181] E. Mostaani, B. Monserrat, N. D. Drummond, and C. J. Lambert, Unpublished, arXiv e-prints::1601.04324 (2016).
- [182] F. Giustino, S. G. Louie, and M. L. Cohen, *Phys. Rev. Lett.* **105**, 265501 (2010).
- [183] T. Pino, H. Ding, F. Güthe, and J. P. Maier, *J. Chem. Phys.* **114** (2001).
- [184] U. Mölder, P. Burk, and I. A. Koppel, *Int. J. Quantum Chem.* **82**, 73 (2001).

- [185] S. Cahangirov, M. Topsakal, and S. Ciraci, *Phys. Rev. B* **82**, 195444 (2010).
- [186] A. Milani, M. Tommasini, D. Fazzi, C. Castiglioni, M. D. Zoppo, and G. Zerbi, *J. Raman Spectrosc.* **39**, 164 (2008).
- [187] N. R. Agarwal, A. Lucotti, D. Fazzi, M. Tommasini, C. Castiglioni, W. Chalifoux, and R. R. Tykwinski, *J. Raman Spectrosc.* **44**, 1398 (2013).
- [188] A. J. Heeger, *Rev. Mod. Phys.* **73**, 681 (2001).
- [189] M. Knupfer, *App. Phys. A* **77**, 623 (2003).
- [190] D. Moses, J. Wang, A. J. Heeger, N. Kirova, and S. Brazovski, *PNAS* **98**, 13496 (2001).
- [191] Y. Shujuan, Z. Chenggang, W. Jinping, L. Jiaye, H. Bo, and C. Hansong, *Int. J. Quantum Chem.* **108**, 1565 (2008).
- [192] O. Cretu, A. R. Botello-Mendez, I. Janowska, C. Pham-Huu, J.-C. Charlier, and F. Banhart, *Nano Lett.* **13**, 3487 (2013).
- [193] A. A. Abrikosov, L. P. Gorkov, I. E. Dzyaloshinski, and I. E. Dzialoshinski, in *Methods of quantum field theory in statistical physics*, Dover publication (New York, 1963) p. Dover publication.
- [194] I. E. Dzyaloshinskii, E. M. Lifshitz, and L. P. Pitaevskii, *Sov. Phys. Usp.* **4**, 153 (1961).
- [195] I. V. Fialkovsky, V. N. Marachevsky, and D. V. Vassilevich, *Phys. Rev. B* **84**, 035446 (2011).
- [196] B. E. Sernelius and P. Björk, *Phys. Rev. B* **57**, 6592 (1998).